

**A Study on Dust Dry Deposition:  
Wind-tunnel Experiment and Improved  
Parameterization**

Inaugural-Dissertation

zur

Erlangung des Doktorgrades

der Mathematisch-Naturwissenschaftlichen Fakultät

der Universität zu Köln

vorgelegt von

**Jie Zhang**

aus Suzhou, China

Köln 2013



Berichtersteller:

Tag der mündlichen Prüfung:

Prof. Dr. Y. Shao  
Prof. Dr. S. Crewell  
28.10.2013



# Kurzfassung

Die Staubdeposition ist eine Schlüsselkomponente des Staubzyklus, allerdings sind die Depositionsmechanismen noch nicht vollständig verstanden. Dies limitiert die Fortentwicklung der Staubforschung. Die Hauptaspekte dieser Studie sind daher die Gewinnung verlässlicher Daten zur trockenen Deposition von Staubpartikeln, die Validierung existierender Staubdepositionsschemata sowie die Verbesserung der Parametrisierung der Staubdepositionsprozesse.

Zu diesem Zweck wurde eine Reihe von Experimenten im Windtunnel durchgeführt. Um Geschwindigkeit und Größe der Staubpartikel festzustellen, die den Messbereich passierten, wurde eine laserbasierte PDPA („Phase Doppler Particle Analyzer“) Technik angewandt. Mit Hilfe eines Aerosolspektrometers wurde die Staubkonzentration gemessen. Wind- und Turbulenzmessungen wurden mit einem Schallanemometer und weiteren im Windtunnel üblichen Messgeräten durchgeführt. Es wird außerdem eine neue Methode zur Datenverarbeitung vorgestellt. Die Staubdepositionsgeschwindigkeit wird für verschiedene Partikelgrößen, Wind- und Bodenoberflächenbedingungen auf Basis der PDPA-Daten bestimmt.

Durch die Windtunnelexperimente konnte auf diese Weise ein zuverlässiger Datensatz erstellt werden, auf dessen Grundlage zwei repräsentative Depositionsschemata validiert werden konnten, nämlich das Schema von Slinn und Slinn (1980) für glatte Oberflächen und das Schema von Slinn (1982) für Vegetationsbedeckung. Es zeigte sich hierbei, dass die Schemata die Depositionsgeschwindigkeit insbesondere für raue Oberflächen leicht unterschätzen. Der Effekt der Interzeption hingegen wird in den Schemata deutlich unterschätzt.

Ein neues Staubdepositionsschema wird in der vorliegenden Studie vorgestellt. Hierin wird der Zusammenhang zwischen Staubdeposition und Impulsvernichtung etabliert. Zur Beschreibung der Deposition wird die „drag partition“ Theorie inklusive der Bodenoberflächenparametrisierung eingeführt. Die verbesserte Parametrisierung kann nun sowohl auf glatte als auch auf raue Bodenoberflächen angewendet werden. Es zeigen sich gute Übereinstimmungen der Ergebnisse des neuen Depositionsmodells mit den Windtunnelmessungen. Durch eine Sensitivitätsanalyse konnte der neu eingeführte Oberflächenparameter, der Element-Frontalflächenindex, als vorwiegender Einflussfaktor auf die Kollisionseffizienz der Bodenoberfläche identifiziert

werden. Somit hat der Index starken Einfluss auf die Deposition von Partikeln aller Größen.

# Abstract

Dust deposition is a key component of the dust cycle in the Earth system. The lack of understanding for the mechanisms of dust deposition has been a major bottle neck to the development of the dust-related research field. The focus of this study is to obtain data for dust dry deposition, to validate the existing dust deposition schemes and to improve the parameterization for dust deposition processes.

A series of dust deposition experiments are carried out in a wind-tunnel laboratory. A laser-based PDPA (Phase Doppler Particle Analyzer) technique is employed to measure the velocity and size of the dust particles which pass through the sampling area. Dust concentration is measured using an Aerosol Spectrometer and wind and turbulence are measured using a sonic anemometer and other conventional wind-tunnel instruments. A new method for processing the data is proposed. The PDPA data are used to derive the dust deposition velocity for different particle sizes and wind and surface conditions.

A reliable dataset is obtained through the wind-tunnel experiments, which are then used to validate two representative dust deposition schemes, the Slinn and Slinn (1980) scheme for smooth surfaces and the Slinn (1982) scheme for vegetation canopies. It is found that the schemes tend to underestimate dust deposition velocity, especially for rough surfaces. The effect of interception is seriously underestimated in the schemes.

A new dust deposition scheme is proposed in this study. The relationship between dust deposition and momentum depletion is established. The drag partition theory including the surface parameterization method is introduced to describe dust deposition. The improved scheme is suitable for both rough and smooth surfaces. The predictions of the new scheme are found to agree well with the experimental data. By sensitivity analysis, it is found that the newly introduced surface parameter, element frontal area index, has a predominant effect on surface collection efficiency and influences the deposition of particles of all sizes.





# Contents

Chapter 1	Introduction .....	1
Chapter 2	Basic Theory and Study Review .....	5
2.1	Basic theory .....	5
2.1.1	Influencing factors.....	5
2.1.2	Assumptions .....	8
2.1.3	Key variables.....	9
2.1.4	Mechanisms for dust deposition.....	12
2.1.5	Deposition steps .....	23
2.2	Review of dust deposition experiments .....	24
2.2.1	Measurement methods.....	24
2.2.2	Experimental data.....	27
2.3	Review of schemes .....	29
2.3.1	Resistance model.....	29
2.3.2	Analytical scheme .....	30
Chapter 3	Wind-tunnel Experiments.....	37
3.1	Introduction of the wind-tunnel experiment .....	38
3.1.1	Facility and instrumentation.....	38
3.1.2	Purposes of the experiments.....	47
3.1.3	Experiment configuration and device setup.....	48
3.1.4	Experimental procedure .....	50
3.2	Test of the experimental conditions .....	51
3.2.1	Stability and reproducibility of the environment .....	51
3.2.2	Structure of wind field and dust concentration profile.....	53
3.3	Summary .....	55
Chapter 4	Experimental Data and Scheme Validation .....	57
4.1	Methodology of data processing.....	57
4.1.1	Processing method for deposition velocity .....	57

---

4.1.2 Quality control.....	58
4.1.3 Method of data process .....	62
4.2 Results and comparison with schemes.....	63
4.2.1 Dust deposition on water surface .....	63
4.2.2 Dust deposition on sticky and smooth surface .....	66
4.2.3 Dust deposition on low-roughness surface.....	68
4.2.4 Dust deposition on canopy surface.....	72
4.3 Conclusions.....	75
Chapter 5 Improved Parameterization .....	77
5.1 Scheme improvement.....	77
5.1.1 Assumptions .....	77
5.1.2 Framework of the new model.....	77
5.1.3 Parameterizations .....	79
5.2 Scheme validation.....	87
5.3 Sensitivity analysis.....	92
5.4 Summary .....	98
Chapter 6 Summary and Outlook .....	99
6.1 Summary and conclusions .....	99
6.2 Outlook .....	101
List of Symbols.....	103
Bibliography .....	107
Acknowledgement .....	113
Erklärung.....	115
Curriculum Vitae.....	117

## Chapter 1

# Introduction

Dust are small mineral particles with diameter less than 20  $\mu\text{m}$ . The motion of dust in the Earth system forms a dust cycle which consists of processes of dust emission, transport and deposition. Dust deposition can be divided into dry and wet deposition, depending on whether precipitation is involved in the removal process. Dust dry deposition, to be studied in this thesis in detail, refers to the removal of dust particles from atmosphere onto surface in the absence of precipitation. In addition to the effect of gravitational settling which is related to the dust particle characteristics, other factors such as atmosphere turbulences and surface properties are also important to this process. Throughout this thesis, dust dry deposition will be simply referred to as dust deposition, unless otherwise stated.

Airborne dust plays an important role in the climatic system. Dust aerosols influence the atmospheric radiation budget via scattering and absorbing shortwave and longwave radiation components (Pérez et al., 2006) and affect the optical properties and lifetime of clouds (Sokolik et al., 2001). According to the reports of the IPCC (Intergovernmental Panel for Climate Change), the uncertainty in aerosol radiative forcing is among the largest of all forcings on the climate system (IPCC Fourth Assessment Report, 2007). In addition, the transport of dust is closely related to the global cycle of minerals and nutrients. It also affects the process of soil formation (Reheis et al., 1995) and the evolution of surface topography on geological time scales (Wells et al., 1987). Moreover, airborne dust in the lower part of the atmosphere causes visibility degradations (Malm et al., 2003) and detrimental health impacts (Pope and Dockery, 1999), which strongly influence the human life.

In recent years, a number of dust models have been developed by coupling modules for atmospheric, land-surface and aeolian processes with land-surface parameter databases, for example, by Shao et al. (2003), Ginoux et al. (2004), Tanaka

and Chiba (2006). One of the main research problems facing the dust modeling community is how surface dust fluxes, including emission and deposition, can be quantified through parameterization. These are both complex dynamic processes involving a number of environmental factors. Our knowledge of these processes is, however, far from complete (Shao, 2008; Petroff et al., 2008a). Dust deposition is particularly poorly understood, although the process has been studied over the last few decades by a number of research groups.

Numerous experimental studies on dust deposition have been carried out, using various measurement methods, such as collection method, gradient method and eddy correlation method. A database of experimental results of dust deposition over various surfaces and under different conditions exists (Chamberlain, 1966 and 1967; Sehmel, 1971 and 1973; Wedding and Montgomery, 1980; Nicholson, 1993; Pryor et al., 2006 and 2007). However, a comparison of the different experimental results remains difficult due to the lack of information on detailed experimental conditions and the poor comparability between the measurement techniques (Wesely et al., 1985; Hicks et al., 1989; Goossens and Rajot, 2008).

On the other hand, several theoretical schemes have been proposed to describe the deposition process under different situations (e.g. Bache, 1979a and 1979b; Slinn, 1982; Wesely et al., 1985; Petroff et al., 2008b). Some mechanisms including turbulence transfer, gravitational settling and surface collection are introduced to predict the quantity of dust deposited on the surface. But the disagreement between the model results and experimental data is significant (Ruijgrok et al., 1995), which indicates that these schemes still have weaknesses in accurately describing the complex deposition processes. One of the obvious deficiencies of the existing schemes is for instance that a rough surface is normally considered to consist of a uniform roughness elements and the total surface collection efficiency is based on consideration of one of the uniform roughness element. These schemes are thus difficult to apply to surfaces with multi-size roughness elements. Also the effect arising from the interactions among the roughness elements on the process of dust collection is neglected.

A thorough literature review reveals, as detailed in Chapters 2 and 3 of this thesis,

that our knowledge of dust deposition is rather incomplete. The large uncertainties in the dust-deposition estimates in dust models, due to the lack of high quality dust-deposition data for comparison, the employment of poorly-tested dust-deposition schemes and the unreliable parameter databases required for the deposition schemes, have been a major bottle neck to the development of the entire research field.

The general aims of this study are to better understand the mechanisms of dust deposition, to collect data for dust deposition scheme validation and to develop better dust deposition schemes. The following targets are achieved through this study.

- A series of wind-tunnel experiments on dust deposition over several surfaces is carried out and a reliable and comprehensive dataset is obtained.
- The dataset is used to validate representative existing dust deposition schemes. The differences between the experimental data and the scheme- predicted results are analyzed and the deficiencies of the schemes are examined.
- An improved dust deposition scheme with a new parameterization is proposed to account for the effect of surface roughness elements interactions.

The thesis is structured as follows: Chapter 2 describes the basic theory of dust deposition velocity, including the most important concepts and the main mechanisms for dust deposition. The traditional experimental methods and prevalent theoretical schemes are also described in Chapter 2. In Chapter 3, the wind-tunnel laboratory and the equipment used for the experiment, as well as the design of the wind-tunnel experiments, are introduced. The methodology of data processing and the experimental data are presented in Chapter 4. Also shown in Chapter 4 is a comparison between the measurements and the dust deposition schemes. In Chapter 5, the new dust deposition scheme is presented and validated against the wind-tunnel measurements. Finally, the summary of the work, along with an outlook for future studies, is given in Chapter 6.



## Chapter 2

# Basic Theory and Study Review

Dust deposition as a scientific problem has attracted the attention from the environmental investigators since as early as the 1900s (Mili and Lempfert, 1904; Winchell and Miller, 1918). In the past century, more systematic research on the topic has been carried out and a wealth of knowledge accumulated, which forms the basis of this study. In this chapter, the basic concepts and hypotheses of dust deposition will be introduced and the dust deposition mechanisms described. Theories, parameterization schemes, and experimental techniques will be reviewed.

## 2.1 Basic theory

### 2.1.1 Influencing factors

Dust deposition is the transport of dust particles from atmosphere onto earth surface. This process is influenced by a number of factors related to the properties of the airborne dust particles, atmospheric flow conditions and the underlying surface characteristics.

#### **Airborne dust**

The physical properties of the airborne dust particles, including shape, size and density, affect their dynamic behavior and hence their motion in air. As shown in Figure 2-1, the shape of dust particles is mostly complex and irregular. Due to this fact, the size of a dust particle is often described using an equivalent diameter ( $D_p$ ) which is the diameter of a spherical object possessing the same physical property as the dust particle (e.g., aerodynamic characteristics in the study of dust deposition). Dust particles are therefore assumed to be spherical in many relevant theoretical works, as

well as in this study. The size of airborne dust distributes over a considerable range, from a few nanometers (nm) to several tens of micrometers ( $\mu\text{m}$ ). The typical number and volume distributions of aerosols (including dust) are as shown in Figure 2-2.

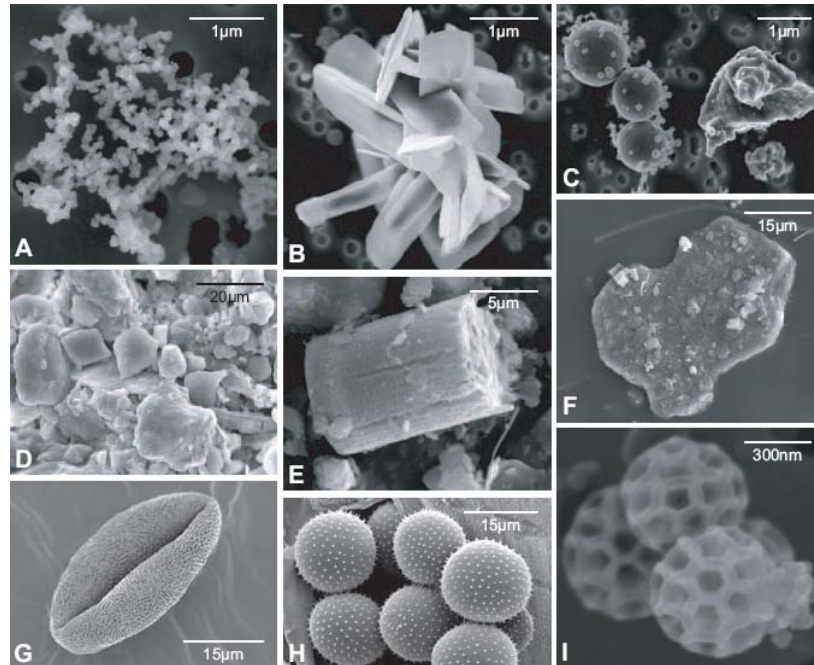


Figure 2-1: Electron microscope images of anthropogenic (A-C) and natural airborne (D-I) particles (Gieré and Querol, 2010). Therein, D, E and F are collected from the Saharan dust.

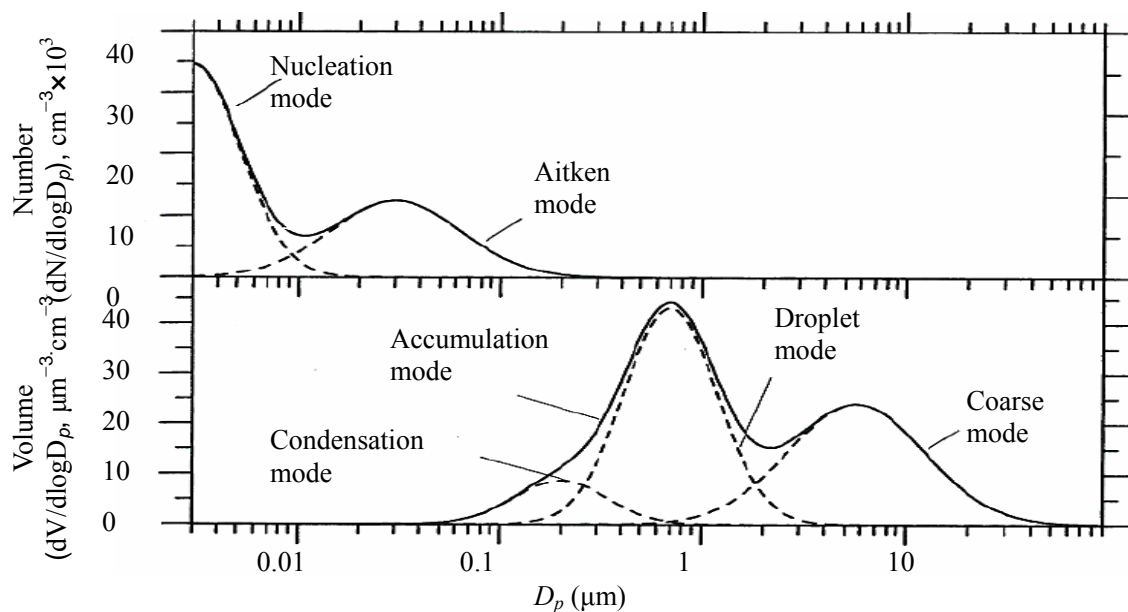


Figure 2-2: Typical number and volume distributions of aerosols (Seinfeld and Pandis, 2012)

Another physical quantity of interest to deposition is particle density,  $\rho_p$ , which



refers to the mass per unit volume of the particle itself. Particle density influences the kinetic properties of the particle and its value is dependent on the particle structure and composition. However, the density of dust particles (of quartz, clays, feldspath, calcite etc.) is typically  $2650 \text{ kg}\cdot\text{m}^{-3}$  (Rajot et al., 2008).

The gravitational force acting on a spherical particle,  $G$ , can be calculated as

$$G = \frac{1}{6} \rho_p \cdot D_p^3 \cdot g \quad (2.1)$$

where  $g$  is the gravitational acceleration.

### Atmosphere (air)

Drag force arising from the relative movement between air and particle is another main reason for dust motion in the atmosphere. Wind therefore plays an important role in the process of dust deposition. In neutral atmospheric boundary layers, the profile of the mean wind speed is approximately logarithmically (Shao, 2008), i.e.,

$$u(z) = \frac{u_*}{k} \cdot \ln\left(\frac{z}{z_0}\right) \quad (2.2)$$

for surfaces with low roughness elements or

$$u(z) = \frac{u_*}{k} \cdot \ln\left(\frac{z - z_d}{z_0}\right) \quad (2.3)$$

for surfaces with high roughness elements, where  $u(z)$  is the mean wind speed (horizontal) at height  $z$  and  $k$  the von Karman constant ( $\sim 0.4$ ). The friction velocity,  $u_*$ , is defined as:

$$u_* = \sqrt{\frac{\tau}{\rho_a}}$$

with  $\tau$  being the surface shear stress and  $\rho_a$  the air density. The roughness length,  $z_0$ , is the height at which  $u(z)$  in Eq. (2.2) or (2.3) becomes zero and describes the capacity of the surface for momentum absorption. The zero-displacement height,  $z_d$ , is introduced to describe the change of the centroid of momentum absorption on high-rough surface.

## Surface

Both the roughness length ( $z_0$ ) and zero-displacement height ( $z_d$ ) are integral parameters related to the roughness of the surface but not the real sizes of the roughness elements (obstacles). For studying surface dust collection, the real sizes of the roughness elements need to be used. For simplicity, a roughness element is usually considered to be cylinders standing perpendicular to the ground (Figure 2-3), with  $h_c$  and  $d_c$  representing respectively its height and diameter.

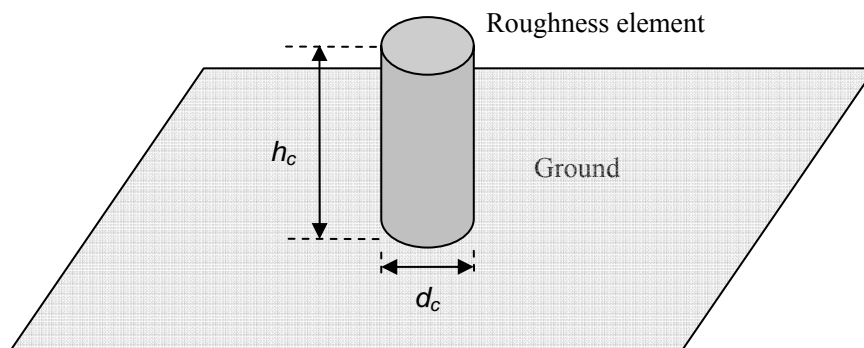


Figure 2-3: Illustration of a roughness element.

### 2.1.2 Assumptions

Some assumptions are required to simplify the complex dust deposition processes and to propose feasible dust deposition schemes. The main ones commonly made in dust deposition studies are summarized in this section.

#### Constant flux in vertical

The most important assumption for dust deposition studies is that dust flux, i.e. mass transfer per unit area per unit time, in the atmospheric surface layer is constant in vertical. This also implies that in the absence of dust emission, the dust flux at any given height, from the top of roughness element to the reference height  $z_r = 100z_0 + z_d$  [about 100 m for typical forest according to Businger (1986)], is equal to the dust deposition flux at the surface.

The constant-flux assumption is not expected to hold for an instant time and location, but is tenable if dust fluxes are averaged over a sufficiently large surface for given time and/or over sufficiently long time period for given location. This assumption provides a way to establish a relationship between dust motion in air and dust deposition to the surface. It also underpins the theory for the deposition flux measurement on surface.

### Surface homogeneity

The assumption of surface homogeneity is made in many dust deposition studies. The size and distribution of roughness elements on the surface are supposed to be uniform. Furthermore, the horizontal flow field is also supposed to be homogeneous.

### 2.1.3 Key variables

#### Deposition velocity

Deposition velocity,  $w_d(z)$ , for a given height,  $z$ , can be defined as the deposition flux,  $F_d$ , normalized by the concentration,  $C(z)$ , (Pryor et al., 2008):

$$w_d(z) = -\frac{F_d}{C(z)} \quad (2.4)$$

According to this definition, deposition velocity changes with dust concentration for the constant flux assumption. If dust is completely absorbed when it reaches the surface (i.e.  $C(0) = 0$ ), then the deposition velocity at the surface would be infinite. For position far away from the surface, the effect of concentration depletion is small. This high position is normally selected as the reference height,  $z_r$ . In previous studies, deposition velocity is generally referred to  $w_d$  given by Eq. (2.4) for level  $z_r$ , namely  $w_{dr}$  in Figure 2-4, unless otherwise stated. The ideal profiles of deposition velocity, dust concentration and flux are as shown in Figure 2-4.

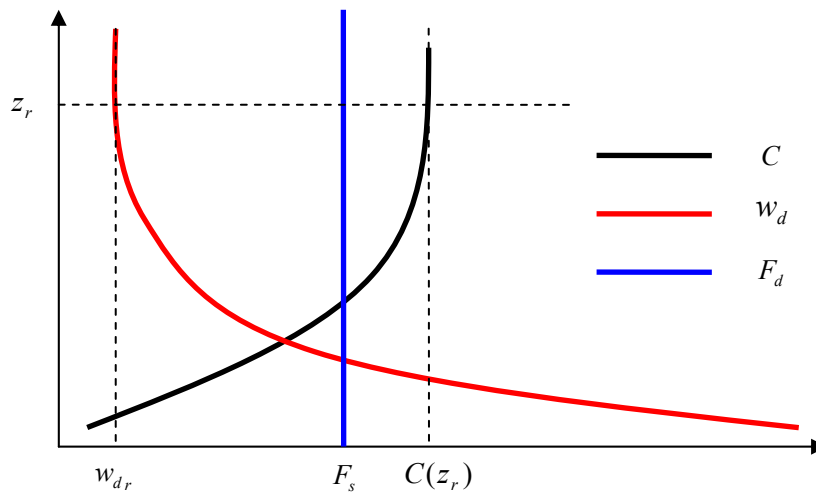


Figure 2-4: Idealized profiles for dust concentration,  $C$ , deposition velocity,  $w_d$ , and deposition flux,  $F_d$ , which is considered to be constant in vertical.  $F_s = F_d$  is the flux of dust deposited to the surface. Dust concentration increases with height. And hence, dust deposition velocity decreases with height.  $w_{dr}$  is the deposition velocity at reference height,  $z_r$ , where the effect of concentration depletion is minimum.

### Surface collection efficiency

Surface collection efficiency,  $\xi$ , is defined as (Bache, 1979a)

$$\xi = \frac{\text{Trap dose}}{\text{Area dose}} \quad (2.5)$$

where the “trap dose” represents the number of particles deposited to a unit surface area and “area dose” refers to the number of particles flowing through an imaginary frame of unit area cross-section, perpendicular to the wind direction. This approach was originally proposed by Gregory and Stedman (1953) and then was widely applied to the studies of dust-surface interactions.

For a roughness element on rough surface, the element collection efficiency,  $E$ , represents the collected fraction of all dust particles initially moving on a collision course with the element (Figure 2-5a). The surface collection efficiency is essentially the synthesized effect of all roughness elements on the surface. The relationship between  $\xi$  and  $E$  depends on the size and location distribution of the roughness elements. If the roughness elements are uniform and distributed as shown in Figure 2-5b, the surface collection efficiency would be equal to the element collection

efficiency, i.e.  $\zeta = E$ . This situation is assumed in many existing dust deposition schemes, e.g., Slinn and Slinn (1980) (SS80 hereafter), Slinn (1982) (S82 hereafter) and Zhang et al. (2001).

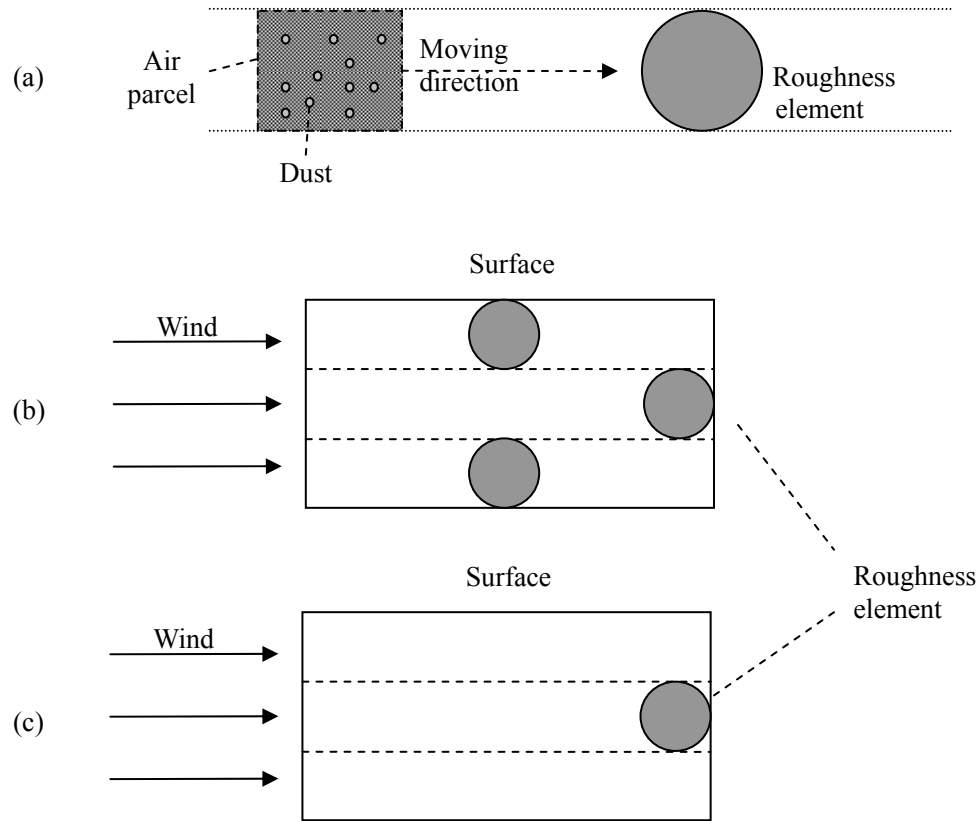


Figure 2-5: Top view of surface with roughness elements. (a) Illustration of element collection efficiency. An air parcel containing dust particles moves towards a roughness element. (b) The case for equal value between surface collection efficiency and element collection efficiency, i.e.  $\zeta = E$ . (c) The case for different surface collection efficiency and element collection efficiency, i.e.  $\zeta < E$ .

In general, surface collection efficiency is contributed to several surface collection mechanisms, including Brownian motion, impaction and interception, as discussed in more detail in Section 2.1.4. We therefore have the following relationship:

$$\zeta = R \cdot (\zeta^B + \zeta^{im} + \zeta^{in}) \quad (2.6)$$

where  $\zeta^B$ ,  $\zeta^{im}$  and  $\zeta^{in}$  are respectively the contribution of the Brownian motion, impaction and interception.  $R$  is a reduction factor of surface collection efficiency due to particle rebound.

## 2.1.4 Mechanisms for dust deposition

### Part 1: Deposition in air

#### Gravitational settling

Airborne particles are forced by gravity ( $G$ , as expressed as Eq. (2.1) and shown in Figure 2-6) and move downwards. Dust deposition due to this process is called gravitational settling. For simplicity, we assume that the air is static. As a particle falls through the static air, a resisting force ( $f_r$ , aerodynamic drag) occurs due to the particle-to-air relative

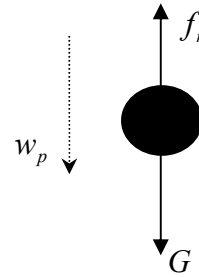


Figure 2-6: Gravitational settling.

motion. The magnitude of the aerodynamic drag increases with the particle-to-air relative velocity, and its effect is to counteract the acceleration of gravity (Figure 2-6). When the aerodynamic drag balances the gravity force, the particle is no longer accelerated and the particle-to-air relative velocity reaches a maximum, which is known as the particle terminal velocity.

For small spherical particles, the relationship between the aerodynamic drag and the particle-to-air relative velocity is (Hinds, 2012):

$$f_r = -\frac{3\pi\mu D_p w_r}{C_c} \quad (2.6)$$

where  $\mu$  is the air dynamic viscosity,  $D_p$  the particle diameter,  $w_r = w_p - w_a$  the relative velocity between the particle with velocity  $w_p$  and the air with velocity  $w$ . The negative sign means that the direction of the aerodynamic drag is opposed to the direction of the particle-to-air relative velocity.  $C_c$  is the Cunningham correction factor which accounts for non-continuum effects when calculating the drag on small particles, which is found to be (Seinfeld and Pandis, 2012)

$$C_c = 1 + \frac{2\lambda_m}{D_p} \left( 1.257 + 0.4e^{-0.55D_p/\lambda_m} \right)$$

where

$$\lambda_m = \frac{K_B T}{\sqrt{2\pi} D_a^2 p}$$

is the particle mean free path,  $K_B$  is the Boltzmann constant,  $T$  temperature,  $p$  pressure and  $D_a$  the effective diameter of air molecule.

Suppose only gravity and aerodynamic forces are exerted on the airborne particle (Figure 2-6). Then, at equilibrium, we have:

$$f_r \Big|_{w_r=w_t} + G = 0 \quad (2.7)$$

where  $w_t$  is terminal velocity, i.e. the maximum particle-to-air relative velocity a particle falling through air under gravity can reach.

A combination of Eq. (2.1), Eq. (2.6) and Eq. (2.7) leads to the expression of particle terminal velocity:

$$w_t = \frac{C_c \rho_p D_p^2}{18\mu} \cdot g \quad (2.8)$$

In other words, if we release a particle in still air and allow it to fall over a sufficiently long time, then the final particle velocity would be

$$w_p \Big|_{final} = w_t + w_a \quad (2.9)$$

The first part on the right side of Eq. (2.8) is the particle relaxation time

$$\tau_p = \frac{C_c \rho_p D_p^2}{18\mu} \quad (2.10)$$

which characterizes the time required for a particle to adjust or "relax" its velocity to a new condition of forces. It follows that Eq. (2.8) can also be rewritten as

$$w_t = \tau_p \cdot g \quad (2.11)$$

## Diffusion

Diffusion is another important mechanism for dust transfer, which results in mixing or mass transport without requiring bulk motion. To describe the effect of diffusion, the quantities under consideration are separated into their mean and fluctuating

components (Stull, 2009), e.g.,

$$a = \bar{a} + a' \quad (2.12)$$

where  $\bar{a}$  is the mean component of  $a$  and  $a'$  the deviation of  $a$  from  $\bar{a}$ . By averaging Eq. (2.12), we have

$$\overline{a'} = 0 \quad (2.13)$$

We can now partition the quantities relevant to dust deposition as follows:

$$u_a = \bar{u}_a + u'_a \quad (2.14a)$$

$$w_a = \bar{w}_a + w'_a \quad (2.14b)$$

$$w_p = \bar{w}_p + w'_p \quad (2.14c)$$

$$C = \bar{C} + C' \quad (2.14d)$$

where  $u_a$  and  $w_a$  are respectively horizontal and vertical velocity of air. The vertical dust flux averaged over a time interval can be calculated as:

$$F_d = \overline{(\bar{w}_p + w'_p) \cdot (\bar{C} + C')} = F_d^{mean} + F_d^{diff} = \bar{w}_p \cdot \bar{C} + \overline{w'_p C'} \quad (2.15)$$

The above expression implies that the total vertical dust flux consists of two components, namely, a component of dust transport by the mean movement,  $F_d^{mean}$ , and a component by fluctuations or the diffusion flux,  $F_d^{diff}$ . Suppose the average vertical wind speed is zero. Then, the mean movement of dust is gravitational settling with flux  $F_d^g$ , i.e.,

$$F_d^{mean} = F_d^g = w_t \cdot \bar{C} \quad (2.16)$$

The diffusion flux is mainly due to dust Brownian motion,  $F_d^B$ , and air turbulence,  $F_d^T$ , i.e.,

$$F_d^{diff} = F_d^B + F_d^T \quad (2.17)$$

(a) Brownian diffusion  $F_d^B$

Airborne dust particles are constantly and randomly bombarded from all sides by air



molecules. If the particles are sufficiently small, then the bombardments cause them to move irregularly in air, i.e. Brownian motion. Brownian motion diffuses particles from regions of higher concentration to lower. This process is termed as Brownian diffusion. The effect of Brownian diffusion can be shown experimentally to obey the Fick's Law of diffusion (Fick, 1855), i.e., the Brownian diffusion flux can be calculated by

$$F_d^B = -k_p \cdot \frac{\partial \bar{C}}{\partial z} \quad (2.18)$$

where

$$k_p = \frac{K_B \cdot T \cdot C_c}{3\pi\mu D_p}$$

is the diffusion coefficient. The negative sign means the direction of flux is opposed to the concentration gradient.

(b) Turbulent diffusion flux  $F_d^e$

Turbulence is an important characteristic of air movement. Atmospheric turbulence can be generated by a number of different conditions, but in the atmospheric boundary layer primarily by wind shear and buoyancy. Turbulence can be visualized as consisting of irregular swirls of motion, called eddies, with different sizes and superimposed on each other (Stull, 2009).

The mechanism through which turbulence generates a dust flux is illustrated in Figure 2-7. Suppose an eddy exists near the surface as shown in Figure 2-7a. Air parcels will be exchanged between Position 1 (high level) and Position 2 (low level). Dust particles move following the air parcels and mix with the environment. If the average concentration at Position 1 is higher than that at Position 2, the amount of downward moving dust particles is more than that of upward moving, i.e., dust is transported downward by the eddy. When air parcels from Position 1 with higher concentration ( $C' > 0$ ) move downwards ( $w'_p < 0$ ), they result in a negative flux (downward). Likewise, the upward moving parcels ( $w'_p > 0$ ), being associated with a lower concentration ( $C' < 0$ ), also result in a negative flux. Both the upward and

downward moving air parcels contribute to a negative  $w'_p C'$ . Thus, for the case shown, the average turbulent dust flux is negative.

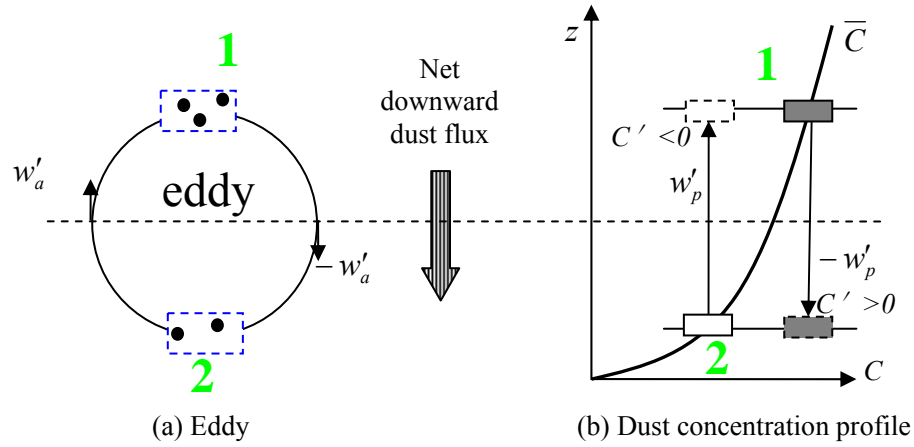


Figure 2-7: Illustration of turbulent dust flux. Air parcels exchange places between Position 1 and 2, with more dust moving downward and less upward. As a result, dust is transferred downwards.

The above discussions suggest that eddy diffusion is determined by two factors: particle fluctuating motion caused by turbulence and concentration gradient. This allows us to use an expression similar to Eq. (2.18) to calculate the eddy dust flux

$$F_d^T = -K_p \cdot \frac{\partial \bar{C}}{\partial z} \quad (2.19)$$

where  $K_p$  is particle eddy diffusivity and  $\bar{C}$  mean dust concentration.

For the fluctuating motion of dust particles caused by turbulence, the relationship between particle eddy diffusivity and eddy viscosity  $K_T$  can be expressed as

$$K_p = Sc_T \cdot K_T \quad (2.20)$$

where  $Sc_T$  is the turbulent Schmidt number which depends on the property of turbulence and the particle relaxation time. Csanady (1963) derived a specific expression of Eq. (2.20) by taking the trajectory-crossing effect into consideration. The relevant result of Csanady's theory is

$$Sc_T = \left( 1 + \frac{\beta^2 w_t^2}{\sigma^2} \right)^{-1/2} \quad (2.21)$$

where  $\beta$  is a dimensionless coefficient and  $\sigma$  is the standard deviation of the turbulent velocity.

For a neutral atmospheric surface layer,  $K_T$  is normally expressed as

$$K_T = ku_*z \quad (2.22)$$

In summary, if the vertical mean velocity of air is zero, the dust deposition flux in air consists of the following parts

$$F_d = F_d^B + F_d^e + F_d^g = \left( -k_p \cdot \frac{\partial \bar{C}}{\partial z} \right) + \left( -K_p \cdot \frac{\partial \bar{C}}{\partial z} \right) - w_t \cdot \bar{C} \quad (2.23)$$

The gravitational settling flux is dependent on particulate size, density and shape, and is important in general for particles larger than 10  $\mu\text{m}$ . Diffusion is effective for small particles. At relatively high levels in the atmospheric surface layer, flow is predominantly turbulent and the diffusion flux occurs mainly through eddy transfer. Close to the surface where turbulence is weak, Brownian diffusion dominates. For particles smaller than 0.1  $\mu\text{m}$ , Brownian diffusion is the dominant mechanism for dust transfer in the absence of turbulence.

## **Part 2: Deposition on surface (surface collection process)**

### **Laminar layer and Quasi-laminar layer**

The laminar layer as shown in Figure 2-8a is a thin layer adjacent to the surface, where turbulence is suppressed and flow is laminar. The thickness of the laminar layer,  $\delta$ , over a smooth surface (small roughness-element Reynolds number) is in direct proportion to air kinematic viscosity,  $\nu$  ( $\text{m}^2\text{s}^{-1}$ ) and inversely proportional to friction velocity,  $u_*$ , (Shao, 2008), i.e.:

$$\delta \sim \nu / u_* \quad (2.24)$$

In the case of a rough surface, a quasi-laminar layer with thickness,  $\delta'$ , can be defined as a sublayer adjacent to the surface and envelops all obstacles (Figure 2-8b).

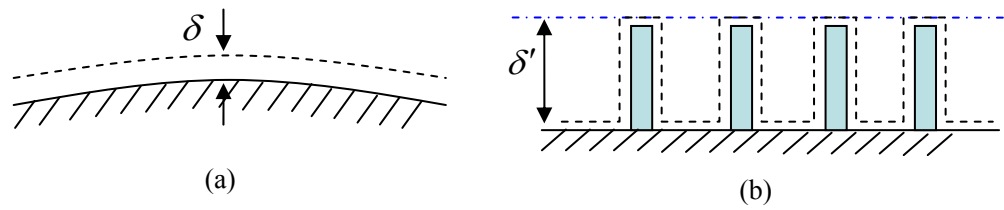


Figure 2-8: Illustration of (a) a lamina layer and (b) a quasi-laminar layer.

The particles which enter and cross the laminar layer (or quasi-laminar layer) may contact the surface and be collected. This is the so called surface collection process. The mechanisms for surface collection include sedimentation, Brownian motion, impaction and interception. Hence, the flux of dust collected by the surface,  $F_s$ , can be expressed as

$$F_s = F_s^g + F_s^B + F_s^{im} + F_s^{in} \quad (2.25)$$

where  $F_s^g$ ,  $F_s^B$ ,  $F_s^{im}$ ,  $F_s^{in}$  respectively relate to the contribution of sedimentation, Brownian motion, impaction and interception.

### Sedimentation

Due to gravity, particles, especially large particles ( $> 10 \mu\text{m}$ ), fall through the laminar layer (or quasi-laminar layer), leading to gravitational sedimentation (Droppo, 2006). Gravitational settling flux is independent on the type of the surface (rough or smooth) but on the surface horizontal projection area.  $F_s^g$  can be expressed as

$$F_s^g = w_{t,\delta} \cdot C_\delta \quad (2.26)$$

where  $C_\delta$  is the typical dust concentration of the laminar (or quasi-laminar) layer. Considering the possible aggregation of hygroscopic particle in humid laminar (or quasi-laminar) layer over wet surfaces, the size of dust particle may grow to  $D_{p,\delta}$  and  $w_{t,\delta}$  is relevant terminal velocity. Methods for predicting size growth of hygroscopic particles exist (e.g. Fitzgerald, 1975; Gerber, 1985) and have been applied to dust deposition schemes (e.g. SS80; Zhang et al., 2001).

### Brownian motion

Brownian motion is the dominant mechanism for very fine particles ( $D_p < 0.1 \mu\text{m}$ ) to cross the laminar layer (Droppo, 2006). According to the definition of surface collection efficiency [i.e., Eq. (2.5)], the Brownian diffusion deposition flux can be expressed as

$$F_s^B = u_{a,\delta} \cdot C_\delta \cdot \xi^B \quad (2.27)$$

where  $u_{a,\delta}$  is the typical horizontal wind speed of the laminar (or quasi-laminar) layer.

It has been suggested that the surface collection efficiency due to Brownian motion,  $\xi^B$ , can be expressed as

$$\xi^B = Sc^{-a} \quad (2.28)$$

where the Schmidt number  $Sc = \nu/k_p$  is the ratio of the kinematics viscosity of air,  $\nu$ , to the particle molecular diffusivity,  $k_p$ . The parameter  $a$  usually lies between 1/2 and 2/3 with larger values for rougher surfaces (S82). Zhang et al. (2001) suggested  $a$  varies between 0.50 and 0.58 depending on different land-use categories.

Petroff et al. (2008b) suggested the collection efficiency for a roughness element (a cylinder perpendicular to the flow),  $E^B$ , as

$$E^B = C_B Sc^{-2/3} Re^{n_B-1} \quad (2.29)$$

where  $Re$  is the Reynolds number for the roughness element.  $C_B$  and  $n_B$  are parameters depending on flow regimes as shown in Table 2-1.

Table 2-1: Typical values of  $C_B$  and  $n_B$  in Eq. (2.29) for different Reynolds numbers (Petroff et al., 2008b).

$Re$	$C_B$	$n_B$
$1-4 \times 10^3$	0.467	1/2
$4 \times 10^3-4 \times 10^4$	0.203	3/5
$4 \times 10^4-4 \times 10^5$	0.025	4/5

## Impaction

Suppose a dust particle moves along with the airflow near the surface. If the particle is too large to follow the directional change of the airflow, then it may collide with the surface. This process is called impaction. Particles with a diameter of 2  $\mu\text{m}$  or larger can be effectively collected by impaction (Droppo, 2006). Impaction is further divided into turbulent impaction and element impaction depending on the mechanisms for the directional change of the flow, as shown in Figure 2-9.

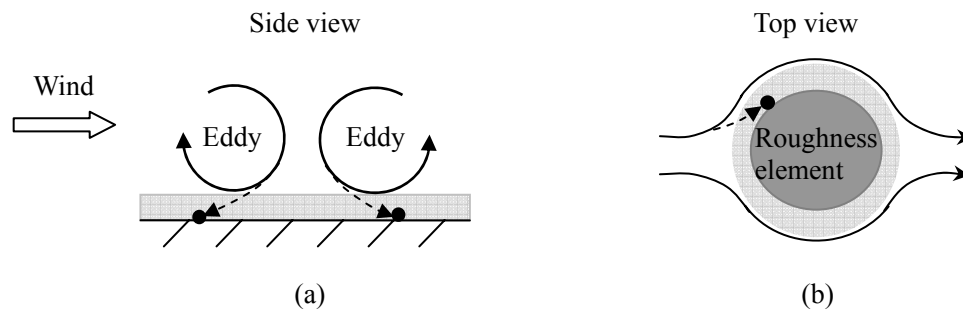


Figure 2-9: Schematic illustration for impaction for the particles which cannot follow the flow stream line and hit the surface. Airflow is represented by the solid lines and the particle paths the dashed lines. The grayish region represents the laminar layer around the surface. (a) Turbulent impaction on smooth surface (without roughness elements). Flow direction changes due to eddy. (b) Elemental impaction on a roughness element. Flow direction changes due to the presence of roughness element.

Turbulence is ubiquitous for atmospheric motion. A dust particle may disengage from the eddy due to inertia and hit the surface (as shown in Figure 2-9a). This is called turbulent impaction. The turbulent impaction may occur over any kind (smooth or rough) of surfaces. Similar to Eq. (2.27), the impaction deposition flux can be expressed as

$$F_{sT}^{im} = u_{a,\delta} \cdot C_\delta \cdot \xi_T^{im} \quad (2.30)$$

where  $\xi_T^{im}$  is the surface collection efficiency of turbulent impaction, which is related to dimensionless particle relaxation time (Liu and Agarwal, 1974)

$$\tau_p^+ = \frac{\tau_p \cdot u_*^2}{\nu} \quad (2.31)$$

SS80 suggested a semi-empirical formulation for surface collection efficiency as follow

$$\xi_T^{im} = 10^{-3/\tau_p^+} \quad (2.32)$$

As shown in Figure 2-9b, the direction of air flow changes near the roughness element (i.e. obstacle). The particle with big inertia may disengage from the stream line and hit the roughness element. This is called elemental impaction. The elemental impaction only occurs around the roughness element. The collection efficiency for a roughness element due to elemental impaction,  $E_e^{im}$ , is normally considered as a function of the Stokes number ( $St$ ). For example, S82 suggested

$$\xi_e^{im} = \frac{St^2}{1+St^2} \quad (2.33)$$

where  $St = \tau_p u_* / d_c$  and  $d_c$  is the dimension of the roughness element. Petroff et al. (2008b) used the following form for isolated cylinders,

$$E_e^{im} = \left( \frac{St}{0.6 + St} \right)^2 \quad (2.34)$$

In summary, the surface collection efficiency caused by impaction can be expressed as

$$\xi^{im} = \xi_T^{im} + \xi_e^{im} = \xi_T^{im} + f(E_e^{im}) \quad (2.35)$$

The function  $f$  depends on the distribution of the roughness elements. For the case as shown in Figure 2-5b,  $f(E_e^{im}) = E_e^{im}$ .

### Interception

Interception occurs when particles of small inertia, which perfectly follow the streamlines of the airflow, but are held back because the distance between the particle centre and the surface is smaller than the radius (Fuchs, 1964). The predominant collection mechanism for particles in the size range of 0.2 to 2  $\mu\text{m}$  is often assumed to be interception (Droppo, 2006).

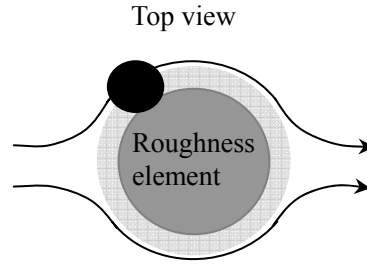


Figure 2-10: As Figure 2-9b but is for interception. The particle follows the streamline well but contacts with the roughness element due to proximity.

Similar to impaction, interception also may be caused by air turbulence. But the particles which can follow the air well should be very small, even compared with the thickness of the laminar layer. When these small particles move into the laminar layer, they will be barely affected by the turbulence. Hence, almost no interception occurs because of turbulence, i.e.  $\xi_T^{in} \approx 0$ .

As shown in Figure 2-10. Interception mainly occurs around roughness element. Specification of interception's contribution to the elemental collection efficiency,  $E_e^{in}$ , is unclear. The estimate is mainly based on the theoretical results for potential flows, such as (Fuchs, 1964)

$$E_e^{in} = \frac{1}{2} \cdot \frac{D_p}{d_c} \quad (2.36)$$

Similar to Eq. (2.35), the surface collection efficiency caused by interception can be expressed as

$$\xi^{in} = \xi_e^{in} = f(E_e^{in}) \quad (2.37)$$

S82 suggested the surface (vegetation) collection efficiency caused by interception as

$$\xi^{in} = \frac{c_v}{c_d} \cdot \left[ c \cdot \frac{D_p}{D_p + d_c^s} + (1-c) \cdot \frac{D_p}{D_p + d_c^l} \right] \quad (2.38)$$

where  $c_d$  is average drag coefficient for vegetation,  $c_v$  the portion of  $c_d$  arising from viscous drag (as opposed to form drag),  $d_c^s$  characteristic dimension (e.g. diameter) of small collectors in a canopy,  $d_c^l$  characteristic dimension of large collectors in a canopy, and  $c$  fraction of the total collected momentum collected by small collectors.



## Rebound

Particle rebound is possible after particle-surface collision. This phenomenon is related to the kinetic energy of the incident particle and the nature of the impact. It also depends on the adhesive conditions of the surface. It is thought to have a strong influence on the deposition of coarse particles larger than 5  $\mu\text{m}$  (Chamberlain, 1967). According to S82, the reduction in collection caused by rebound,  $R$ , can be expressed as

$$R = \exp(-b\sqrt{St}) \quad (2.39)$$

where  $b$  is an empirical constant, assumed to be 2 based on grass deposition measurements (Chamberlain, 1967). In the studies of Giorgi (1988) and Zhang et al., (2001),  $b$  is set to 1.

The other mechanisms, such as electrophoresis, diffusiophoresis and thermophoresis, may also contribute to dust deposition, but the magnitude is considered small compared with the ones introduced above (Davidson and Wu, 1990).

### 2.1.5 Deposition steps

The process of dust deposition consists of three steps, as shown in Figure 2-11.

- Firstly, dust particles move downwards due to the combined effect of turbulent diffusion and gravitational settling from the atmosphere to a very thin layer of stagnate air adjacent to the surface.
- Then, the particles pass through the thin laminar layer to reach the surface. In the laminar layer, turbulence is suppressed. Brownian diffusion (for small particles) and gravitational settling (for large particles) are the main factors driving the deposition process.
- Finally, the particles are collected by the surface due to impaction, interception and Brownian motion. They are either retained to or rebounded from the surface, depending on a combination of surface and particle properties.

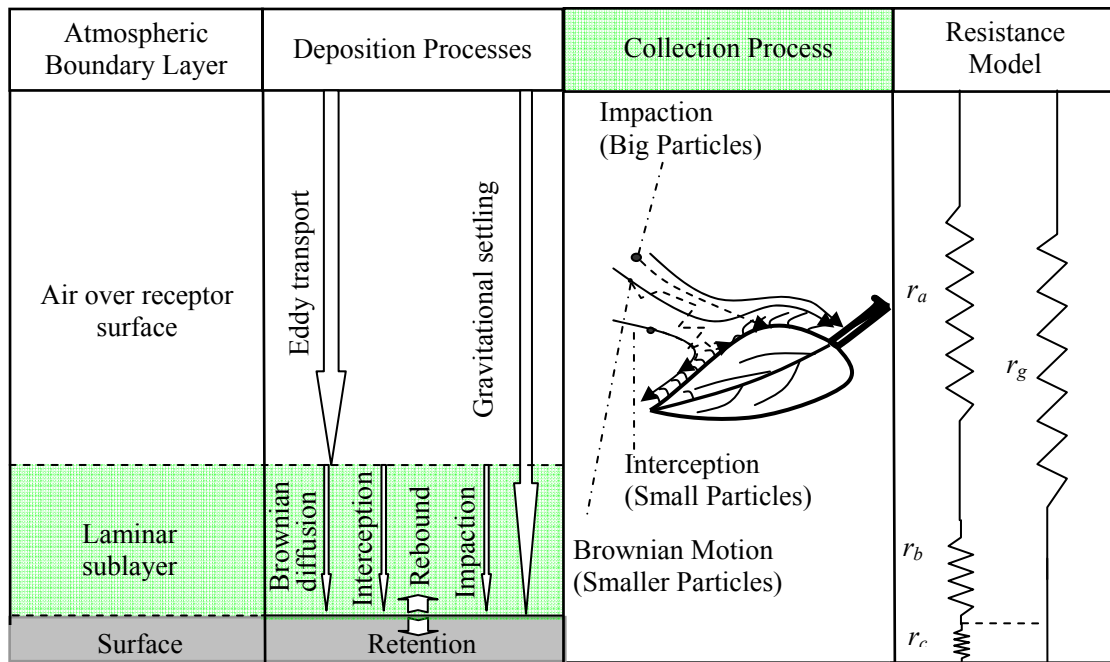


Figure 2-11: Dust deposition steps and mechanisms. Dust is firstly transferred downwards by eddy diffusion and gravitational settling from free air to the layer adjacent to surface. Brownian motion, interception and impaction lead to particle crossing the laminar layer to contact the surface. There, the particles are either retained or rebound.

## 2.2 Review of dust deposition experiments

Over the past few decades, numerous experimental studies on dust deposition have been performed. The experimental results have been summarized in the studies of McMahon and Denison (1979), Sehmel (1980), Nicholson (1988), Wesely and Hicks (2000), Pryor et al. (2008) and Petroff et al. (2008a). The measurement results are obtained under different surfaces, particles and wind conditions by using a variety of techniques. Here, the measurement methods and techniques involved are reviewed briefly.

### 2.2.1 Measurement methods

As stated in Eq. (2-4), dust deposition velocity,  $w_d$ , is dust deposition flux divided by dust concentration. Measuring dust flux is the main challenge, for which a wide range of methods has been developed. These methods can be roughly divided into the

general categories of direct and indirect methods (Seinfeld and Pandis, 2012). Direct methods explicitly determine the dust deposition flux by collecting dust deposited on the surface or by measuring the vertical dust flux in air near the surface. Indirect methods derive dust deposition fluxes by measurements of quantities such as dust concentration.

## **Direct methods**

### **(a) Surface collection method**

Dust deposition flux is obtained by measuring the amount of dust collected by a natural or surrogate surface. The measurements are local and do not represent dust deposition over a large area unless in homogeneous conditions, but are easy to perform. A wide variety of surrogate surfaces, such as filters, plastic and glass surfaces, has been used (Goossens and Offer, 1994). Foliar extraction (e.g. leaf washing or analysis of snow) enable the natural surface to be employed in dust deposition measurements. The associated throughfall technique is widely used to measure the dust deposition on canopies (Garland, 2001).

The accumulation method and the trace method are usually used in conjunction with the surface collection method. For accumulation method, the total amount of dust deposited on the surface is collected for certain time duration. It can be readily carried out but contains no details of the measurement process, and it is not suitable for studying the influences of the meteorological conditions on dust deposition.

The tracer method is based on chemically or radioactively labeled particles, which are introduced into the field or the wind tunnel for measurement purposes. The uncertainties in aerosol granulometry and measurement reliability are usually low as the introduced aerosols are pre-characterised. This method has been widely used in wind-tunnel studies with different surface types, such as grass (Chamberlain, 1967), water (Sehmel and Sutter, 1974), moss (Clough, 1975), spruce (Ould-Dada, 2002) etc.

### **(b) Eddy-correlation method**

Turbulent dust flux can be expressed as the covariance of particle velocity and dust

concentration

$$F_d^T = \overline{w'_p C'} \quad (2.40)$$

For sufficiently small dust particles,  $w_p \approx w_a$ , such that the above equation becomes

$$F_d^T \approx \overline{w'_a C'} \quad (2.41)$$

Thus, if the instantaneous wind velocity and particle concentration can be simultaneously sampled, then turbulent dust flux can be calculated by use of Eq. (2.41). This method is called eddy-correlation method which requires fast particle sampling (Businger, 1986). To quantify the particles, various methods have been employed in the previous studies, based on analyzing the different properties of the particles, such as electric charge (Wesely et al., 1977; Lamaud et al., 1994), photometry (Hicks et al., 1982; Wesely et al., 1985; Hicks et al., 1989), optical refraction (Gallagher et al., 1997; Bleyl, 2001) or liquid condensation into nuclei or Aitken particles (Buzorius et al., 1998; Nemitz et al., 2002). Another method, termed eddy-accumulation method, operates in a similar fashion, but a distinction is made between the upward and downward moving particles (Wesely and Hicks, 2000).

Both the eddy-correlation and eddy-accumulation methods are micro-meteorological methods for measuring turbulent fluxes (Businger, 1986). But for dust flux measurements, the dust particles must be small enough, such that they behave similarly as traces in turbulent flows. As averaging over certain time duration is required to estimate the covariance, the measurement conditions must be assumed to be stationary, horizontally homogeneous and there is no particle source in the near field, such that the dust fluxes measured at a certain height can be considered to be identical to that at the surface. However, the results obtained by using this method do not include the contribution of gravitational settling.

## **Indirect methods**

### **(c) Gradient method**

Dust deposition flux is determined by measuring the vertical gradient of dust concentration and using the flux-gradient relationship [such as Eq. (2.19)] to infer to

the associated deposition flux. This method, often be used for smooth surface or low canopies, is not entirely applicable to rough canopies such as forests because the concentration gradient on the accessible measurement height is often weak, and samplers with great precision are necessary. Another limitation of this method is that the required dust diffusivity is often associated with large uncertainties (Cellier and Brunet, 1992).

### 2.2.2 Experimental data

Here, we don't repeat the work of reviewing the details of the dust-deposition experiments carried out over the past decades (McMahon and Denison, 1979; Sehmel, 1980; Wesely and Hicks, 2000; Pryor et al., 2008; Petroff et al., 2008a), but summarize the representative results to assess the state of the existing datasets. Figure 2-12 shows the dust deposition velocity as a function of particle size for different surface types, obtained from both wind-tunnel and field experiments. The line shows the predicted results using the S82 scheme for a representative forest.

As shown, the deposition velocity for large particles exhibits a much smaller scatter and fits well to the S82 scheme. That is because gravitational settling is the main mechanism for the deposition of large particles, which depends primarily on particle size and is relatively easy to estimate. A much larger scatter in the  $w_d$  measurements exists for small particles, ranging from less than 0.01 to 10  $\text{cm}\cdot\text{s}^{-1}$ . This wide range of variations may be related to the different experimental conditions, such as differences in meteorological conditions and surface types. It is also found that the results of field measurements are always higher than those from the wind-tunnel experiments, but detailed descriptions of the conditions for many experiments are lacking.

Different measurement methods and equipment used may be another cause for the large scatter. The use of surrogate surfaces may lead to under-collection of depositing particles. Further, it is questionable to extend these devices to represent the natural surfaces. For micrometeorological techniques to work well, spatial homogeneity and temporal stationary are assumed for the successful use of these techniques. However, it is often difficult to fulfill all requirements in experiments under field conditions.

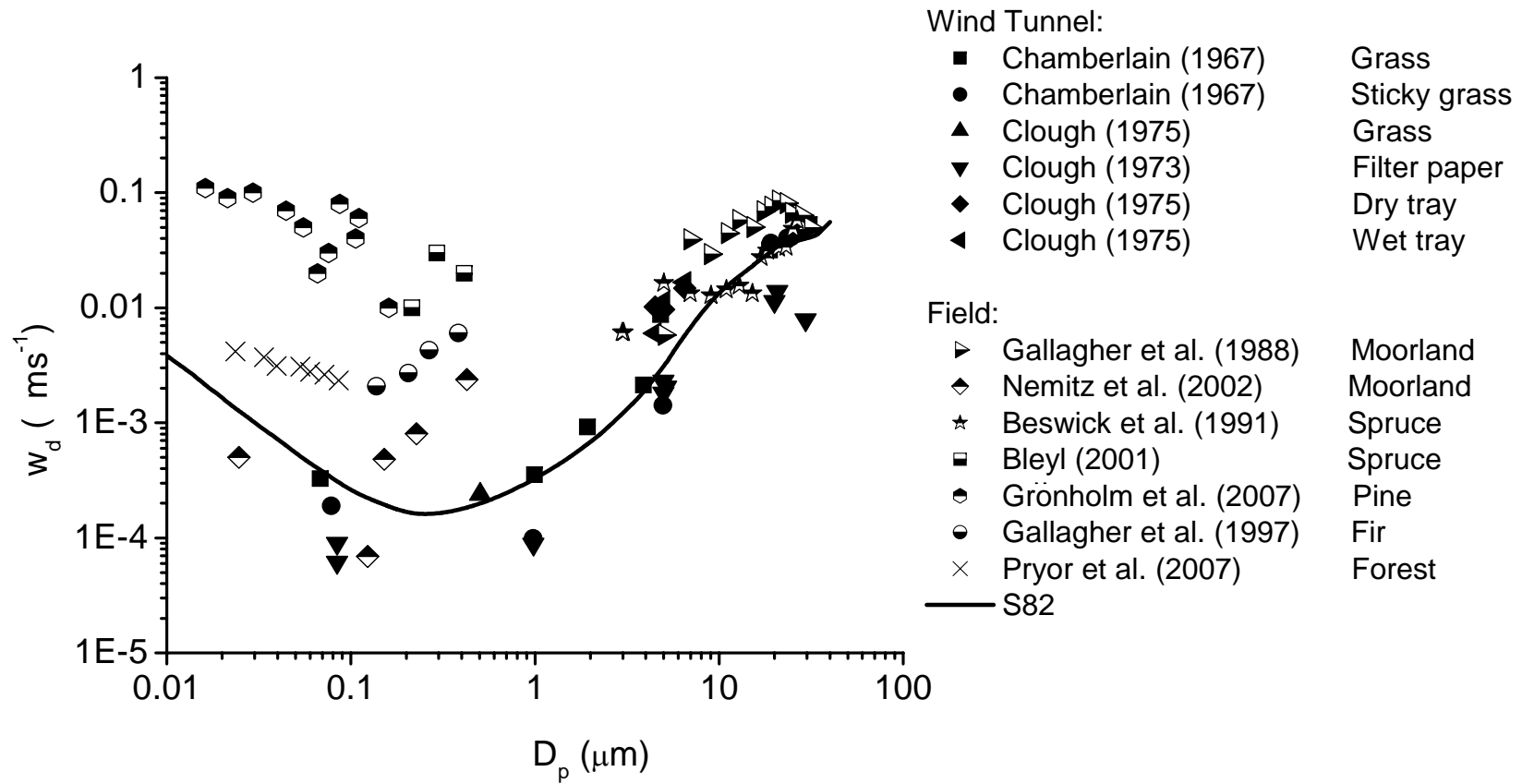


Figure 2-12: Measurements of deposition velocities against particle size for different surfaces and a theoretic prediction.

Besides the errors in the techniques themselves, accurate measurements of the size distribution of airborne dust was not involved in most deposition measurements. Therefore, it cannot be ruled out that the higher deposition velocities were caused by sedimentation effects of large particles. The gap between the  $w_d$  values derived from field and wind-tunnel experiments is considerable and requires further clarification.

## 2.3 Review of schemes

Over the past few decades, several schemes have been developed to parameterize dust deposition. A concept of deposition resistance (or its inverse, the conductance) is widely applied and it has proved to be useful to interpret the deposition process in terms of an electrical resistance analogy (Hicks et al., 1987; Wesely and Hicks, 2000; Seinfeld and Pandis, 2012).

### 2.3.1 Resistance model

The resistance approach uses an analogy to electrical circuits to establish a scheme that incorporates the various processes of dust deposition. The dust concentration gradient over the surface corresponds to the potential (in analogy to voltage drop) for deposition and the deposition flux is considered as current. The total deposition process is considered to function as a circuit and the deposition velocity is the inverse of the total resistance of this circuit. Following the description of the deposition mechanisms and steps, the deposition flux (like a current) flows through two parallel pathways. As shown in the right hand of Figure 2-11, the different resistances correspond to the different deposition steps. And the deposition velocity is expressed as:

$$w_d = (r_a + r_b + r_c)^{-1} + w_t \quad (2.42)$$

where  $r_a$  is the aerodynamic resistance related to dust diffusivity and air stability. For a neutral atmospheric boundary layer, it can be approximated as (Seinfeld and Pandis, 2012):

$$r_a = \frac{1}{ku_*} \cdot \ln\left(\frac{z}{z_0}\right) \quad (2.43)$$

$r_b$  represents the resistance to transfer across the laminar (or quasi-laminar) layer and is named laminar (or quasi-laminar) layer resistance.  $r_b$  depends on the surface collection process and according to Zhang et al. (2001) we have

$$r_b = \frac{1}{\varepsilon_0 u_* R \xi} \quad (2.44)$$

where  $\varepsilon_0$  is an empirical constant ( $\sim 3$ ).  $r_c$  is the surface resistance defined as

$$r_c = \frac{C(0)}{F_d} \quad (2.45)$$

where  $C(0)$  is the dust concentration at the surface.  $w_t$  represents the contribution of gravitational settling treated as a parallel conductance (Figure 2-11).

It is usually assumed that all particles adhere to the surface (i.e.,  $C(0)=0$ ), so that  $r_c$  is normally neglected. And considering the gravitational settling is not a gradient-driven flux and does not fit into the resistance concept, a modified version of the resistance scheme is proposed by Hicks et al. (1987):

$$w_d = \frac{1}{r_a + r_b + r_a \cdot r_b \cdot w_t} + w_t \quad (2.46)$$

### 2.3.2 Analytical scheme

The analytical scheme is generally derived from the governing equation of dust deposition [i.e. Eq. (2.23)]. The atmosphere is usually divided into several layers to describe the deposition process. The constant flux assumption and continuity of dust concentration is required to connect the adjacent layers. According to the number of the layers, the existing schemes can be categorized as a single-layer model and a multi-layer (mostly two-layer) model.

#### (a) Single-layer model

In a single-layer model, the surface layer is treated as a bulk entity (Owen and Thomson, 1963; Chamberlain, 1967; Sehmel, 1980; Raupach et al., 2001). For instance, in the Raupach et al. scheme, the deposition velocity is the bulk single-layer



conductance made up of three components acting in parallel

$$w_d = w_t + G_{im} + G_B \quad (2.47)$$

where  $G_{im}$  the impaction conductance and  $G_B$  the Brownian diffusion conductance are assumed to be proportional to the bulk aerodynamic conductance for momentum ( $G_{aM} = u_*^2 / u_r$ ,  $u_r$  is the mean wind speed at reference height  $z_r$ ) which is contributed by the form or pressure drag ( $G_{aM,form}$ ) and viscous or skin-friction drag ( $G_{aM,visc}$ ), i.e.

$$G_{aM} = G_{aM,form} + G_{aM,visc}$$

Furthermore, the following assumptions are made by Raupach et al. (2001) scheme,

$$G_{im} = a_f \cdot \left( \frac{St}{0.8 + St} \right)^2 \cdot G_{aM,form} \quad (2.48a)$$

$$G_B = a_v \cdot Sc^{-2/3} \cdot G_{aM,visc} \quad (2.48b)$$

where  $a_f$  and  $a_v$  are factors in the order of 1 accounting for the roughness sheltering effects. Finally, the deposition velocity is expressed as

$$w_d = w_t + G_{aM} \cdot [f_{form} \cdot a_f \cdot \left( \frac{St}{0.8 + St} \right)^2 + (1 - f_{form}) \cdot a_v \cdot Sc^{-2/3}] \quad (2.49)$$

where  $f_{form}$  is the fraction of the total drag exerted as form drag.

The single-layer model of Raupach et al. (2001) is a great simplification of the real deposition steps, but includes the main physics to capture the dependence of the three major processes (gravitational settling, impaction and Brownian diffusion) on particle diameter and wind speed. The effect of the interaction between the roughness elements (sheltering effect) to the deposition process is considered.

### (b) Two-layer model for smooth surface

SS80 used a two-layer model to explain dust deposition over water surface considered as a smooth (without roughness elements) and wet (leading to hygroscopic growth of particles). The atmosphere below a certain height is divided into two layers, an upper constant flux layer of depth  $h$ , where turbulent diffusion is dominant, and a lower

deposition layer of depth  $\delta$ , where molecular diffusion is dominant and dust is transferred by impaction, Brownian diffusion and gravitational settling to the surface (Figure 2-13).

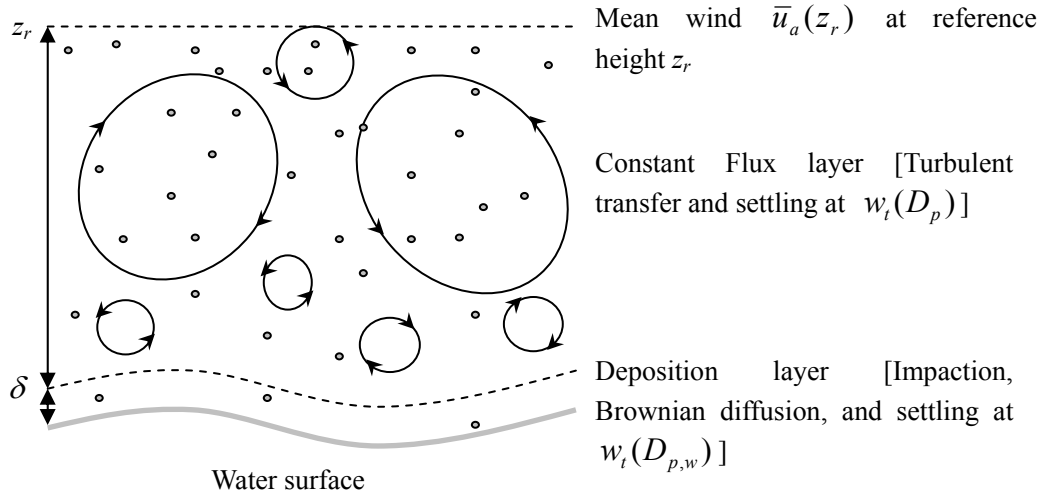


Figure 2-13: A schematic illustration of the two-layer model for dust deposition to a smooth surface (SS80)

The dust deposition velocity over the water surface is expressed as

$$\frac{1}{w_d} = \frac{1}{w_C} + \frac{1}{w_D} - \frac{w_t(D_p)}{w_C w_D} \quad (2.50)$$

where

$$w_C = \frac{1}{1-k} \cdot \frac{u_*^2}{\bar{u}_a(z_r)} + w_t(D_p) \quad (2.51)$$

is the transfer velocity for the upper layer, and  $w_t(D_p)$  is the particle terminal velocity and

$$w_D = -\alpha m'' + \frac{1}{k} \cdot \frac{u_*^2}{\bar{u}_a(z_r)} \cdot \left( Sc^{-1/2} + 10^{-3/\tau_p^+} \right) + w_t(D_{p,w}) \quad (2.52)$$

is the transfer velocity for the low deposition layer, where  $m''$  represents the contribution from diffusiophoresis and  $\alpha = 10^3 \text{ cm} \cdot \text{s}^{-1} / (1 \text{ g} \cdot \text{cm}^{-2} \cdot \text{s}^{-1})$ . Hygroscopic growth of particles is taken into account via the particle growth theory proposed by

Fitzgerald (1975).  $D_p$  and  $D_{p,w}$  represent the diameter of dry and wet particle, respectively.  $w_t(D_{p,w})$  is the terminal velocity for the wet particles. Here, both the Schmidt number ( $Sc$ ) and the dimensionless relaxation time ( $\tau_p^+$ ) relate to the wet particle diameter.

### (c) Two-layer model for canopy surface

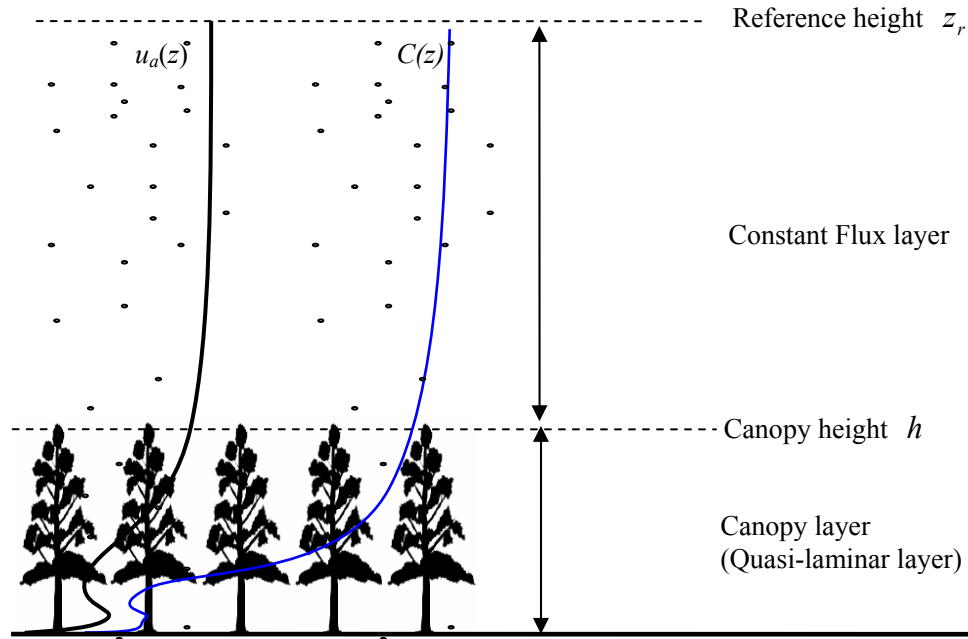


Figure 2-14: Schematic illustration of a two-layer model for dust deposition on canopy.

In most cases, a multilayer model is applied to study the dust deposition over canopy surfaces (Bache, 1979a, b; S82; Zhang et al., 2001 and Petroff et al., 2008b). The atmosphere is generally split into two layer, a canopy layer (or the so-called quasi-laminar layer) with the depth of canopy height  $h$  and the upper layer from the top of the canopy to the reference height ( $z_r$ ), where the concentration depletion caused by the canopy collection is minimal. The representative work is proposed by S82. The terminal velocity is added to the deposition velocity calculated from the following equation which only includes the effect of turbulent and Brownian diffusion

$$\frac{\partial}{\partial z} \left[ (k_p + K_p) \cdot \frac{\partial C}{\partial z} \right] = (c_d \alpha u_a) \cdot \xi \cdot C \quad (2.53)$$

where  $\alpha$  is the surface area of vegetation per unit volume.

Based on a series of approximations and assumptions, the solution for above equation can be found and the dust deposition velocity shown to be

$$w_d = (r_a + r_s)^{-1} + w_t \quad (2.54)$$

where

$$r_a = \frac{u_a(z_r) - u_a(h)}{u_*^2} \quad (2.55)$$

and  $r_s$  is the resultant effect of both  $r_b$  and  $r_c$ . It is found that

$$r_s = \frac{u_a(h)}{u_*^2} \cdot \frac{1}{\sqrt{\xi}} \cdot \left( \frac{1 + \sqrt{\xi} \tanh \gamma \sqrt{\xi}}{\sqrt{\xi} + \tanh \gamma \sqrt{\xi}} \right) \quad (2.56)$$

where  $u_a(z_r)$  and  $u_a(h)$  are horizontal wind speeds at the reference height and the canopy top, respectively,  $u_*$  is friction velocity and  $\xi$  is the surface collection efficiency determined by the combination of Eq. (2.6), (2.28), (2.32), (2.33), (2.38), and (2.39).  $\gamma$  is a parameter characterizing the wind profile in a canopy, expected to be in the range from 2 to 5.

Venkatram and Pleim (1999) pointed out that “the electrical analogy does not apply to modeling dry deposition of particles”, because the formulation is not consistent with mass conservation as expressed in Eq. (2.23). The same critique applies to the Raupach et al. (2001), SS80 and S82 schemes. Venkatram and Pleim (1999) suggested an analytical expression of deposition velocity by solving Eq. (2.23)

$$w_d(z) = \left[ \frac{w_t}{1 - \exp(-r \cdot w_t)} \right]^{-1} \quad (2.57)$$

with boundary condition  $C(0) = 0$ , and

$$r = \int_0^z \frac{1}{K_p(z) + k_p} dz \quad (2.58)$$

However, problems remain with the approach of Venkatram and Pleim (1999), because Eq. (2.23) does not describe surface collection process and it is problematic to set the lower limit of the integral, Eq. (2.58), to zero. A more serious problem is that the boundary condition  $C(0) = 0$  is often incorrect. Besides, the confusion

between surface collection efficiency and element collection efficiency has limited the veracity of these schemes. In many schemes, the canopy surface is considered to be of uniform roughness elements and no parameter is proposed to describe the effect of the canopy architecture.

None of the existing schemes has been well validated, due to the lack of high-quality experimental data as motioned in Section 2.2. So the tasks of this study are to produce a cohesive experimental dataset and to propose a more reasonable scheme which satisfies the governing equation of dust transport [Eq. (2.23)] and includes new parameters to describe the effect of the canopy architecture to the dust deposition process.



## Chapter 3

# Wind-tunnel Experiments

Wind tunnel is an experimental facility which basically consists of a fan and a tubular passage (or working section, Figure 3-1). Airflow is generated by the fan and manually controlled, so that a desired flow in the working section is achieved. The parameters of interest are measured using relevant equipments.

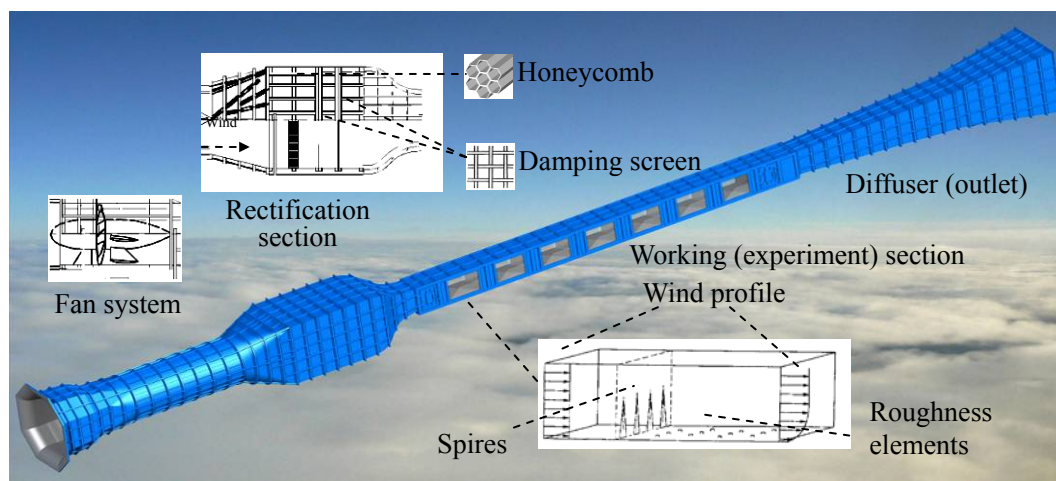


Figure 3-1: Sketch map of the wind tunnel of LZU.

Since the 1960s, a number of wind-tunnel experiments on dust deposition have been carried out (e.g. Chamberlain, 1966, 1967; Sehmel, 1973; Little, 1977; Ould-Dada, 2002) and a considerable amount of dust-deposition data has been accumulated. However, large uncertainties exist in the data set, due to the limitations of the dust observing equipments and the poor comparability between the measuring techniques. There is also a lack of descriptions on the details of the experiments. As a consequence, the quality of the existing datasets does not meet the requirement of the in-depth dust deposition studies. To remedy this problem, we carried out a series of wind-tunnel experiments on dust deposition. But firstly, the wind-tunnel setup and

instrumentation are described in this chapter.

### 3.1 Introduction of the wind-tunnel experiment

Our experiments are carried out in the “Environmental Mechanics” Key Laboratory of the Lanzhou University (LZU) of China. The research facilities are maintained by the Key Laboratory for both wind-tunnel and relevant measurement devices, such as Phase Doppler Particle Analyzer (PDPA) used to measure particle size and velocity, Aerosol spectrometer (AS) used to measure dust concentration and Ultrasonic anemometer used to measure wind speed.

#### 3.1.1 Facility and instrumentation

##### (a) Wind tunnel

The LZU wind tunnel is a blow-down wind tunnel, which is in total 55 m long, including a powerful fan system, a rectification section, a working section and a diffuser (Figure 3-1). High-speed and turbulent wind can be generated by a fan of 75 kW in the first part. Then, the turbulent air flows into the rectification section. Here, the flow speed is slowed down because of a bigger cross-section. Turbulent eddies in the original flow generated by the fan are destructed by a combination of honeycomb and damping screens (rectangular grids) deployed in this part. After passing the rectification section, the air flow becomes uniform. The rectified air flow is accelerated in the working section which has a smaller but uniform cross-section of 1.3 m (width)×1.45 m (height).

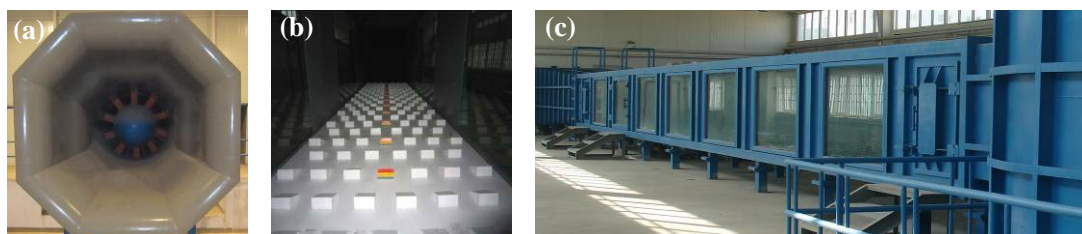


Figure 3-2: Illustration of the LZU wind tunnel. (a) Fan; (b) Roughness elements; (c) Working section.

The length of the working section is about 22 m. Some spires or roughness



elements (or both) are set up in the front of this section to generate a turbulent boundary layer. Finally, the air flows out from the diffuser with an increasing cross-section. The wind tunnel is controlled by a computer and the wind speed can be adjusted between 3 and 40  $\text{m}\cdot\text{s}^{-1}$ . Figure 3-2 shows some pictures of the wind tunnel of LZU.

### (b) Dust feeder

For creating a dust-deposition condition, a device is required to supply dust particles steadily and continuously into the tunnel. For this purpose, we designed a dust feeder as shown in Figure 3-3. The main parts of the dust feeder are illustrated in Figure 3-4.



Figure 3-3: Dust feeder.

A rotary feeder is used for supplying the dust stored in the upper hopper into a circulatory connected underneath. The feeding speed is controlled by the rotating speed of the rotary feeder. Air is driven by a blower in the circulatory and moves circularly with high speed. The supplied dust particles are well mixed in air and another blower then pumps the dusty air from the circulatory part slowly and continuously into the wind tunnel.

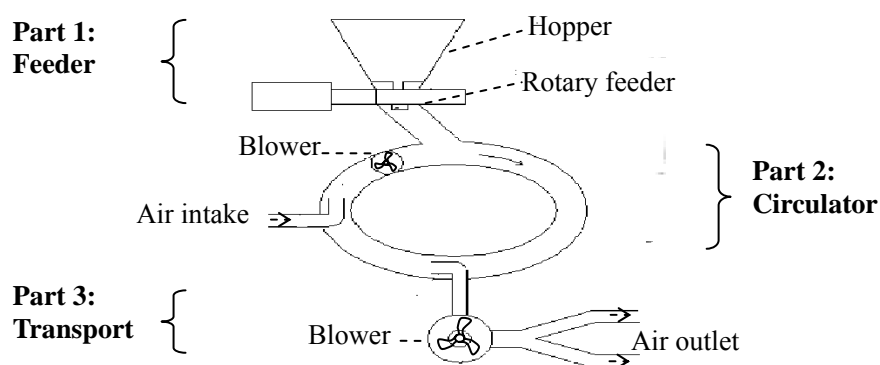


Figure 3-4: Illustration of the dust feeder specially designed for the project.

### (c) Phase Doppler Particle Analyzer (PDPA)

PDPA is a non-contact optical instrument which combines laser-based optical transmitter, optical receiver, electronic signal processor and software for capturing and analyzing data (Figure 3-5).



Figure 3-5: Appearance of the PDPA (by Dantec). (a) Laser generator; (b) Probes (laser transmitter and receiver); (c) Signal processor.

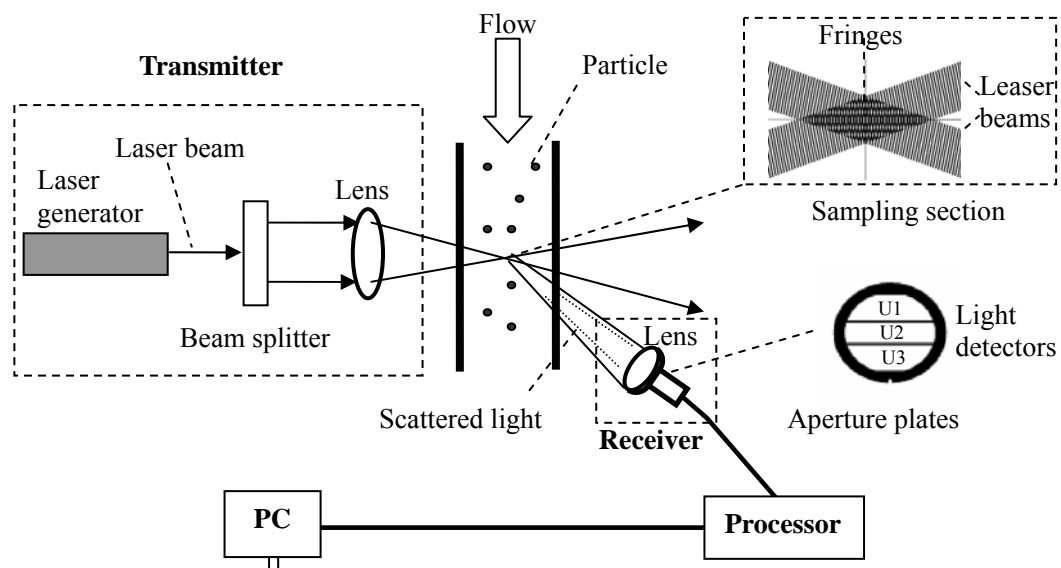


Figure 3-6: Basic structure of the PDPA. Velocity and size of particles which passes the sampling area are obtained by analyzing the light scattered by the particles.

As shown in Figure 3-6, by using a beam splitter, the laser beam is split into two

beams which are then transmitted and managed to intersect in their respective beam waists. Interference occurs in the intersection region of these two coherent and intersecting laser beams. Then the fringes of brightness and darkness with distance of  $\delta_f$  will be produced. The value of  $\delta_f$  depends on wavelength of the laser,  $\lambda_l$ , and the angle between the incident beams,  $\theta$  (Dantec Dynamics A/S, 2006)

$$\delta_f = \frac{\lambda_l}{2\sin(\theta/2)} \quad (3.1)$$

This intersection region is the sampling area. When a particle passes through this area, it alternates between the bright and dark fringes, and scatters light with different intensities. The varying scattered light is detected by a photo-detector fixed in the receiver probe to produce current pulse depending on the intensity of the received

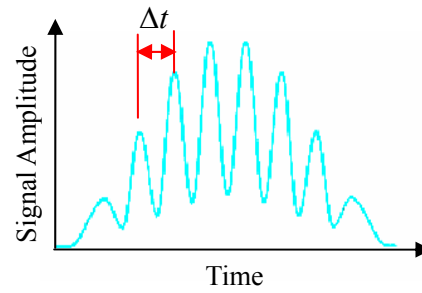


Figure 3-7: Doppler burst.

light. Then, a Doppler burst signal is gained (as shown in Figure 3-7). The time interval  $\Delta t$  between the adjacent peaks of the Doppler burst signal represents the transit time between the known spacing of the adjacent fringes ( $\delta_f$ ). Then the particle velocity component orthogonal to the fringes can be determined as

$$V_p = \delta_f / \Delta t \quad (3.2)$$

The size of the particle which passes through the sampling area is gained by analyzing the phase differences of the scattered light between the different detectors. The different detectors are actualized by aperture plates (as shown in Figure 3-6). The whole light sensor is divided into several parts as different light detectors with different azimuth angles (such as U1, U2, and U3 in Figure 3-6). As an example, we discuss the phase differences between detector 1 and detector 2 (Figure 3-8). The Doppler bursts of the passing particle are received by different detectors (1 and 2) with same frequency but different phases. The corresponding phase difference is

$$\phi_{12} = 2\pi f \cdot \Delta t_{12} \quad (3.3)$$

where  $f$  is the frequency of the scattered light, and  $\Delta t_{12}$  can be obtained by analyzing the burst signal of detector 1 and detector 2 (Figure 3-8b).

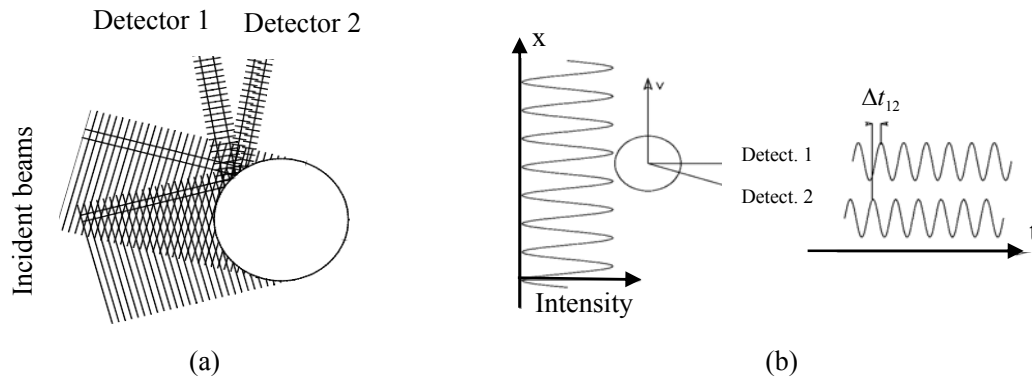


Figure 3-8: (a) The light scattered from a reflecting spherical particle is received by two photo-detectors; (b) The phase difference between two detectors at different azimuth angles.

For spherical particle, the phase difference of the scattering light between two various detectors can be calculated as (Durst, and Zaré, 1976)

$$\phi_{ij} = \phi_j - \phi_i = \frac{\pi}{\lambda_l} D_p \times (\varphi_j - \varphi_i) \quad (3.4)$$

Here, the subscripts  $i$  and  $j$  represent different detectors;  $\phi_i$  is the phase of the Doppler signal received by detector  $i$ ;  $\varphi$  is a geometrical factor fixed by the scattering model and the setup of the optic parameters; and  $D_p$  is the particle diameter. Finally, the particle size is obtained by the combination of Eq. (3.3) and Eq. (3.4).

The Phase-Doppler method requires no calibration (Dantec Dynamics A/S, 2006) because the measured results (particle size and velocity) only depend on the laser wavelength and relevant optical configuration. The beam attenuation or deflection, which occurs in air of dense particle and influence on light intensity, will not degrade the precision of PDPA.

It should be noted that this method of diameter measurement only works well for spherical particles, because the mathematical relationship between the phase difference and the particle size, i.e. Eq. (3.4), is based on ideal spherical particles.

PDPA detects discrete burst signals from the passing particles to produce the

information of arrival time, transit time, velocity and size for the particles. But if more than one particle is present in the sampling area simultaneously, the detected burst signal will fluctuate and is the sum of the effect from all particles in the sampling area.

The PDPA employed in our experiments is manufactured by Dantec. The specified accuracy is 1% for velocity measurement and  $\pm 0.5 \mu\text{m}$  for particle-size measurement. This device is suitable for measuring particle velocity in the range between  $-100 \text{ m}\cdot\text{s}^{-1}$  and  $200 \text{ m}\cdot\text{s}^{-1}$  and particle size in the range between  $0.5 \mu\text{m}$  and  $2000 \mu\text{m}$ . For data collecting, the Burst mode is selected and the scattering angle is  $150^\circ$ . The sampling area is an ellipsoid (about  $4.55 \times 10^{-11} \text{ m}^3$ ) with semi-principal axes of length  $0.149 \text{ mm}$ ,  $0.1489 \text{ mm}$  and  $3.921 \text{ mm}$ .

#### (d) Aerosol Spectrometer (AS)

Aerosol Spectrometer (Model 1.109, Figure 3-9) is a portable device used for continuous measurement of aerosol concentration and size distribution. This equipment detects aerosols in the size range between  $0.25 \mu\text{m}$



Figure 3-9: Aerosol Spectrometer.

and  $32 \mu\text{m}$  in 31 size channels ( $0.25\text{-}0.28\text{-}0.3\text{-}0.35\text{-}0.4\text{-}0.45\text{-}0.5\text{-}0.58\text{-}0.65\text{-}0.7\text{-}0.8\text{-}1\text{-}1.3\text{-}1.6\text{-}2\text{-}2.5\text{-}3\text{-}3.5\text{-}4\text{-}5\text{-}6.5\text{-}7.5\text{-}8.5\text{-}10\text{-}12.5\text{-}15\text{-}17.5\text{-}20\text{-}25\text{-}30\text{-}32 \mu\text{m}$ ). The results of each size range are determined in one of the two basic modes: particle counts or mass concentration. The fastest sampling rate of the device is  $1 \text{ Hz}$  and the highest suitable concentration is  $2 \times 10^9$  particles per  $\text{m}^3$ .

As shown in Figure 3-10a, the air with dust is drawn into the device through an internal volume-controlled pump at a rate of  $1.2$  liters per minute. The dust particles move following the sample air directly into the measuring chamber and are detected through light scattering inside the chamber. After the measuring chamber, almost all particles are collected by a filter and the clean air then flows back to the ambient.

Figure 3-10b is a sketch map of the measuring chamber assembly, containing a laser optical system which allows particle counting by collecting the scattered light from individual particles with a detector. A laser diode is used to generate the laser

beam. By means of illumination optics, the laser beam is focused to a flat elliptical strip. The sample air is led as a particle flow at a certain speed to through the focus of the beam. The scattering light pulse of every single particle is detected by a second optic device under a scattering angle of  $90^\circ$ . The size of the particle is estimated by the intensity of corresponding scattering light. Then the concentrations of particles with different diameter are obtained (Grimm Aerosol Technik GmbH & Co. KG., 2010).

The entire sampling dust will be collected by the filter. Then the gravimetric analysis can be performed to estimate the density of dust particles and to validate the reported aerosol mass. In addition, chemical analysis is made possible.

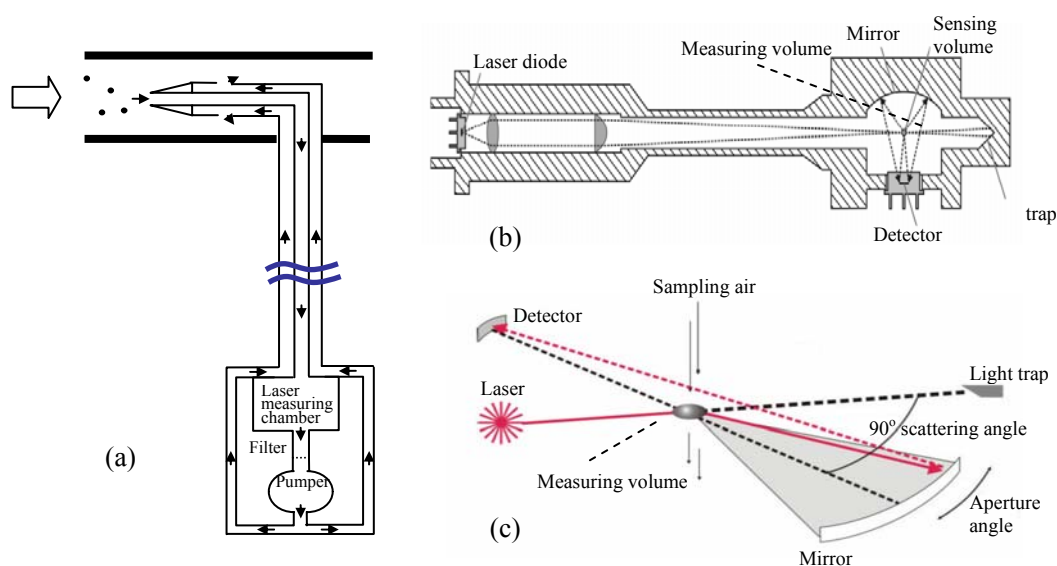


Figure 3-10: Illustration of aerosol spectrometer (Grimm Aerosol Technik GmbH & Co. KG., 2010). (a) Interior flow of ambient-air; (b) Laser measuring chamber; (c) Measuring principle. (Grimm Aerosol Technik GmbH & Co. KG., 2010)

### (e) Ultrasonic Anemometer (CSAT3)

CSAT3 is a 3-D ultrasonic anemometer used to measure wind speed in three dimensions. Three pairs of non-orthogonally oriented transducers are employed to sense the wind. As shown in Figure 3-11, each pair of transducers transmits and receives the ultrasonic signal. The speed of ultrasonic is directly related to the wind speed along the sonic

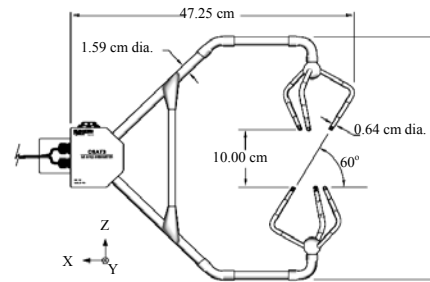


Figure 3-11: Anemometer head (Campbell Scientific, Inc., 2007)

transducer axis. Accordingly, the value of wind speed can be estimate by analysis the flight time of the ultrasonic. The specified accuracy of CSAT3 is  $\pm 0.01 \text{ m}\cdot\text{s}^{-1}$  and the sampling frequency can be set between 1Hz and 60 Hz (Campbell Scientific, Inc., 2007). Although the size of the anemometer head is somewhat large (47.25 cm  $\times$  42.44 cm, Figure 3-11) for wind-tunnel measurements, CSAT3 can still be employed to monitor information of flow field.

#### (f) Artificial surfaces and dust

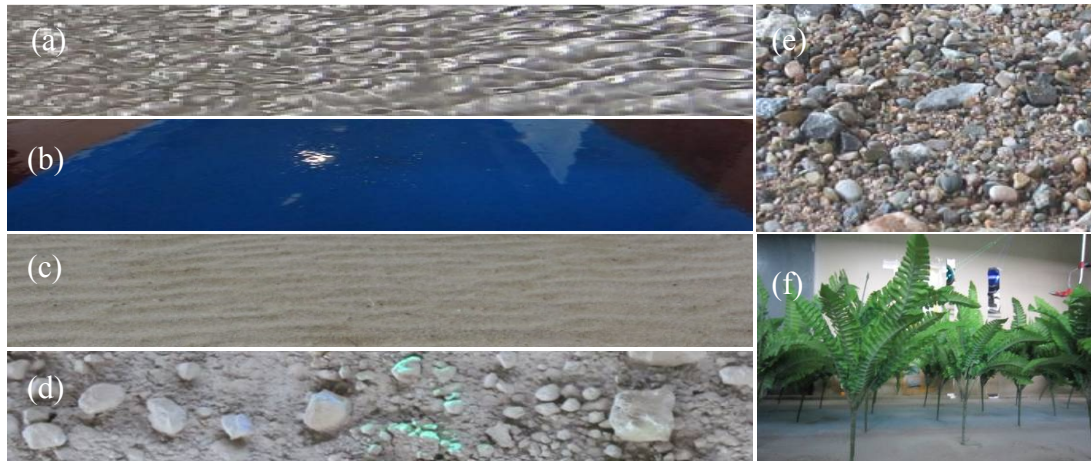


Figure 3-12: A series of surfaces: (a) Water; (b) Sticky (Oiled) wood plane; (c) Sand; (d) Sandy loam; (e) Gobi surface; (f) Trees.

A series of surfaces as shown in Figure 3-12 are prepared for the wind-tunnel experiments, including (a) water; (b) oiled wood plane; (c) sand (mean diameter: 200  $\mu\text{m}$ ); (d) sandy loam; (e) Gobi surface; (f) artificial trees (height 23 cm, spacing

20 cm).

For sandy surfaces, some particles may be lifted under high wind conditions, which may cause the emission of small particles and influence the measurements of dust deposition. To handle this problem, the surface is wetted by a water sprayer and then air-dried to produce a crust to prevent the motion of surface particle. Apart from that, we planned to study dust dry deposition over a sticky surface. As high humidity may cause particle growth, lubricating oil was used to oil the wood plane. In addition, artificial landscape trees made of plastics are employed to simulate canopy surface.

To facilitate the preparation of the surfaces, trays are used (Figure 3-13a). Figure 3-13b and Figure 3-13c show the dimensions of the trays. In addition, four wheels are mounted on each tray and it is thus easy to move the trays along the orbits fixed on the floor of tunnel. The trays are then filled with water, sand or sandy loam and are arrayed along the midline of the work section of the tunnel to produce the relevant surfaces.

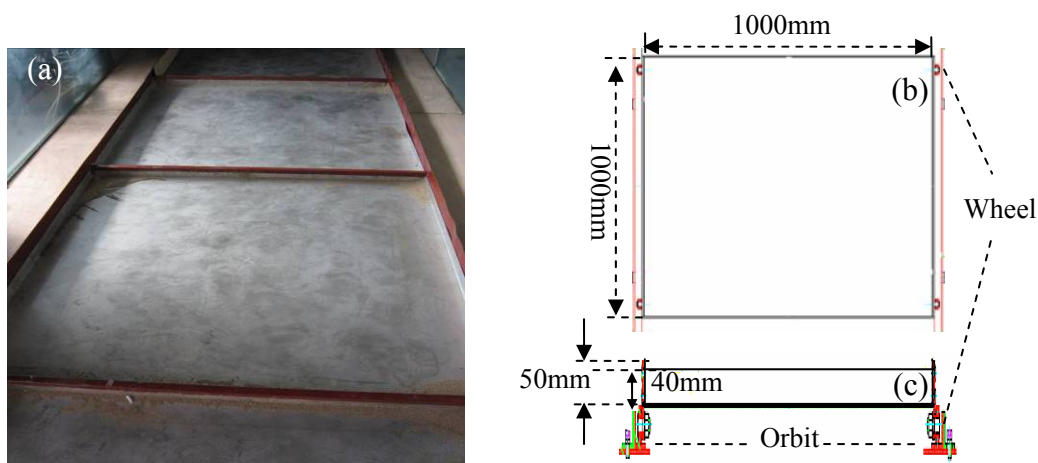


Figure 3-13: (a) Picture of the trays; (b) Top view; (c) Side view.

As mentioned before, PDPA works best for spherical particles. Therefore, the optical characteristics and spherical degree of the particles are important factors which affect the reliability of the PDPA measurements. The white powder (Figure 3-14a) is selected as the dust source for our experiments. The chemical composition of this powder is Silicon Dioxide ( $\text{SiO}_2$ ) and the density is  $2200 \text{ kg}\cdot\text{m}^{-3}$ . The particles have a good spherical degree (Figure 3-14b) and the mean diameter is  $10 \mu\text{m}$ . The particle



size distribution is shown in Figure 3-14c. The powder ( $\text{SiO}_2$ ) used in our experiments is different from natural dust in shape (irregular, as shown in Figure 2-1), color and density (because of different chemical components). But the white and spherical particles have good performance in light reflection and well meet the requirements of the PDPA.

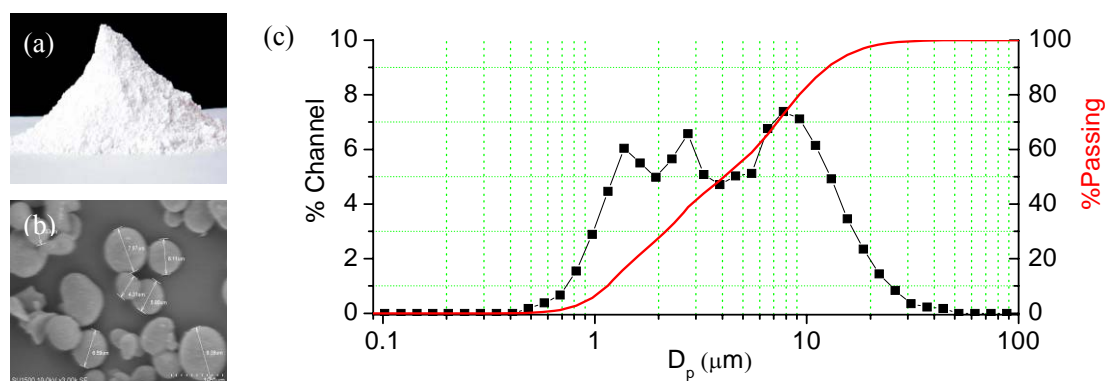


Figure 3-14: Dust powder. (a) Appearance; (b) Microscopic figure; (c) size distribution (measured by Particle Size Analyzer (Model: S3500)).

### 3.1.2 Purposes of the experiments

We intend to measure the deposition velocities for different surfaces, different particle sizes and different wind speeds. The data will then be used to validate the existing and newly developed dust deposition schemes, such as those of SS80 and S82. We are therefore interested in the following variables:

#### (a) Dust concentration profile

Dust concentration is measured by the Aerosol Spectrometer (AS). The measurements can be repeated at different heights in sequence to obtain dust profiles.

#### (b) Wind structure

Wind profile is obtained by measurements of wind speed at different heights. While CSAT3 is generally useful for measuring wind speed and turbulence intensity, it is not available for the regime close to the surface because of the relatively large anemometer head. Fortunately, some wind information, such as horizontal wind speed can be derived from the PDPA particle velocity measurements of small particles (more than 95% of the particles are smaller than  $20 \mu\text{m}$ , as Figure 3-14c shows), which can be

placed near the surface.

### **(c) Dust deposition velocity**

While dust deposition velocity cannot be measured directly, it can be derived from the particle velocity and size measured by the PDPA, as described in Chapter 4.

### **3.1.3 Experiment configuration and device setup**

The configuration of our wind-tunnel experiments is as shown in Figure 3-15. A 6 m long roughness-element section is located in the front of the wind-tunnel working section to generate a deep turbulent boundary layer. Downstream of this section is the test surface. The dust feeder is placed at the beginning of the working section to inject dust into the tunnel through a tubular manifold which consists of two rows of six outlets with even spacing of 20 cm (Figure 3-15a). The manifold is adjusted such that the bottom and the top rows are at approximately 20 cm and 40 cm above the top of the surface. After release, the dust particles are fully dispersed in the turbulent boundary layer over the test surface.

Several devices, including the PDPA, AS and CSAT3, are located near the end of the working section (Figure 3-15c). The sampling area of the PDPA coincides with the midpoint of the transducer pairs of the CSAT3. The sampling point of the AS is 15 cm behind the measuring point of the PDPA to avoid the influence of the air-pump on the flow at this point. All probes are fixed on adjustable frames to allow measurements at different heights, and the distance between the measurement area and the dust outlet is about 10 m to ensure sufficient development of the turbulent boundary layer and dust dispersion.

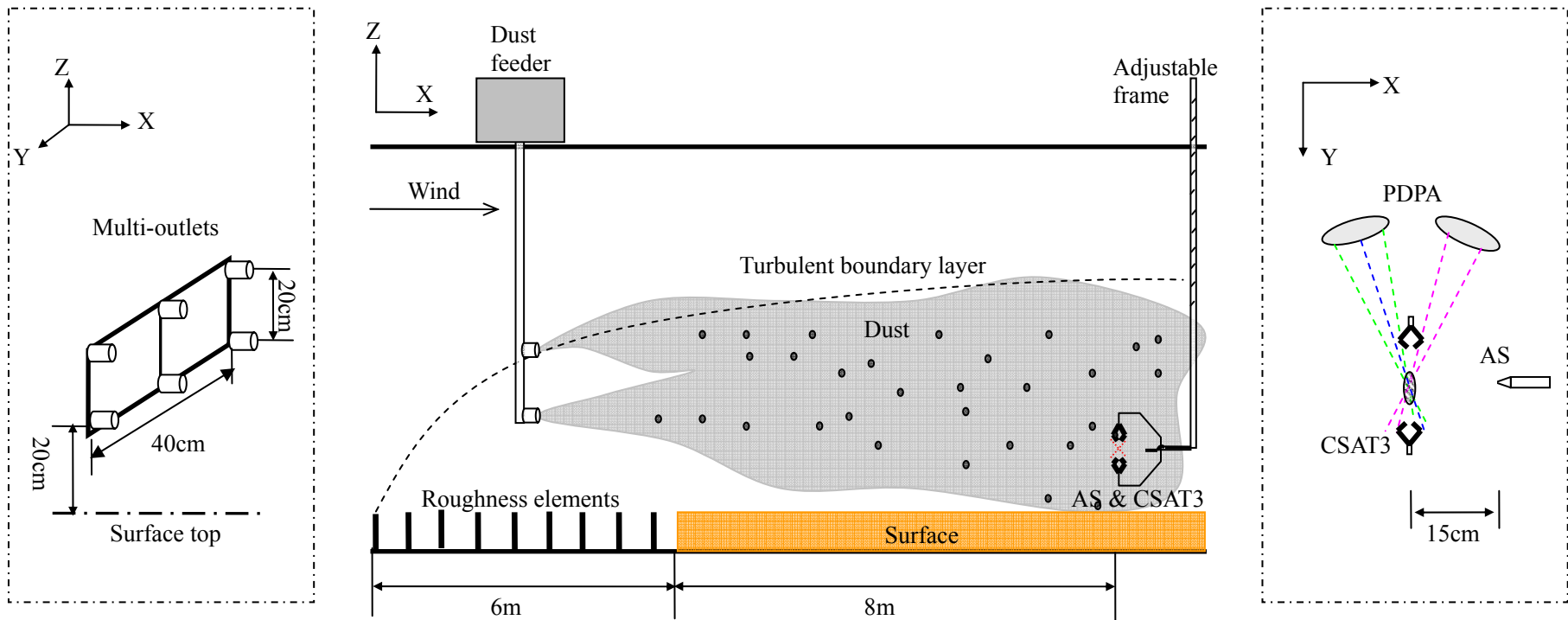


Figure 3-15: Configuration of the wind-tunnel experiments. (a) The manifold of the dust feeder; (b) Wind-tunnel working section, with a roughness-element surface and a test surface; (c) Arrangement of the PDPA, AS and CSAT3 sensors.

The laser light emitted from an Argon-Ion laser of the PDPA is split through a beam splitter into three pairs in green lines with wavelength of 514.5 nm, blue lines of 488 nm and violet lines of 476.5 nm. These six laser lines intercross at the sampling area and the 3D-velocity and the size of the particles passing through this area are measured. According to the size of the wind-tunnel cross section, the focal length of the front lens of the transmitting and receiving optics of the PDPA, the back scatter setup is arranged with a scattering angle of 150 degrees. The sampling frequency of the CSAT3 is set to 20 Hz.

### **3.1.4 Experimental procedure**

We conducted a series of experiments for different surface types (Figure 3-12). For a given surface, measurements are repeated for 3 different flow speeds. For each case, at least 3 successful runs are made. The procedure of the experiment is as follows:

#### **Step 1: Preparation**

The surfaces as shown in Figure 3-12 are structured in the working section, according to the configuration shown in Figure 3-15. In addition, the height of the roughness elements is adjusted to match the leeward surface to generate a logarithmic wind profile.

#### **Step 2: Profile Measurement**

Wind speed, dust concentration and dust mean velocity are measured at different heights by the CSAT3, AS and PDPA, respectively. About 10 points with different heights are selected from the lowest possible point depending on the probe size to about 0.2 m. Measurements are successively made at the different height points. For each point, the measuring period is 3 minutes.

#### **Step 3: Point Measurement**

A point, about 5 cm above the surface, is selected for point measurement. Dust-particle velocity and size at this point is measured by the PDPA. Simultaneously, dust concentration is monitored by the AS at same height and 15 cm downstream. If possible, the CSAT3 is used to measure the air flow speed for the sampling area of the PDPA. The measurement for this step takes 10 minutes.

**Step 4: Repeat**

The surface is re-prepared and the Steps 2 and 3 are repeated.

The experiments are carried out under different situations as shown in Table 3-1.

Table 3-1: List of wind-tunnel experiments.

Surfaces	Fan speed & Repeat times			
	3000 rpm	6000 rpm	9000 rpm	12000 rpm
Water	3	3	3	/
Sticky wood plane	3	/	3	3
Sand	3	3	4	/
Sandy loam	3	3	3	/
Gobi surface	3	3	3	/
Tree	3	3	/	3

**3.2 Test of the experimental conditions**

Before the formal experiment, the experimental conditions are tested to make sure that they are adequate for our purposes.

**3.2.1 Stability and reproducibility of the environment**

Some simple tests are carried out over the flat wood surface to examine the stability and reproducibility of the wind field and dust concentration. The wind speed is monitored using the CSAT3 at 6 cm height (the anemometer head of the CSAT3 is positioned flat to keep the x-z plane horizontal). The tests of 10 minutes are repeated under three different fan-rotation speeds of 3000, 6000 and 9000 rpm.

Figure 3-16 shows the monitoring results of the horizontal wind speed. As shown, wind speed fluctuates with time but is always close to the mean velocity. The blue lines represent the 3-minute running means, which corresponds to the minimum length (3 minutes) of the measuring period in the formal experiments. The running means confirm the stability of the wind field over time spans longer than 3 minutes.

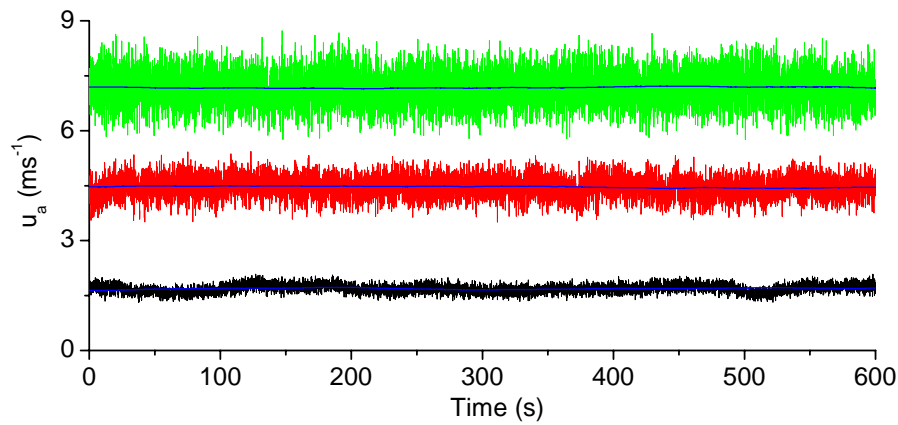


Figure 3-16: Test results for wind-tunnel flow stability at 60 mm height. The lines with color of black, red and green are experimental data for fan speed 3000, 6000 and 9000 rpm, respectively. The blue lines represent the 3-minute running means.

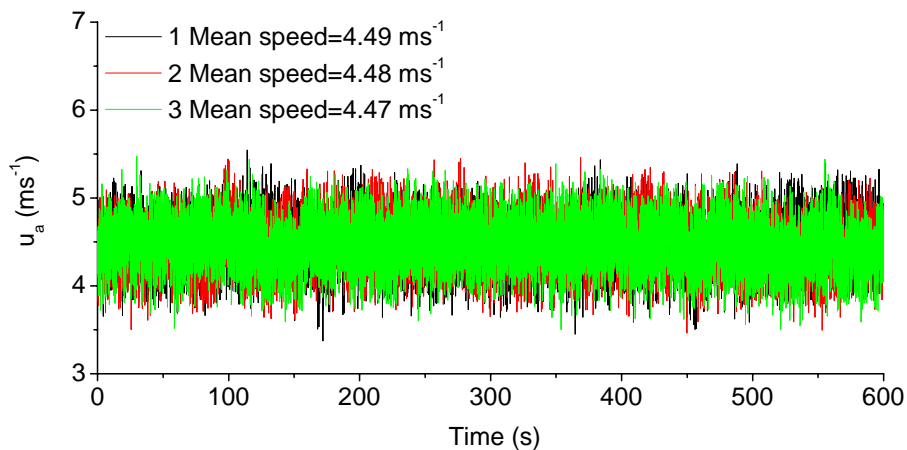


Figure 3-17: Test results for wind-tunnel flow reproducibility at 60 mm height with fan speed 6000 rpm. The measurements are repeated for three times and the results are shown in different color.

To validate the reproducibility of the wind field, the measurements are repeated 3 times at 60 mm and with fan speed 9000 rpm. The results (Figure 3-17) show the mean speeds are very close to each other for the repeated runs.

Figure 3-18 shows the results of dust concentration (number per cubic meter) measured by AS with a sampling rate of 1/6 Hz. The fan rotating speed is set to

9000 rpm, and the height of the sampling point 50 mm above the surface. The measurements are repeated three times. The data, shown as symbols in Figure 3-18, varies with time as a consequence of wind turbulence and the changing feeding speed of the dust feeder, but the mean dust concentrations for the repeated runs are close to each other.

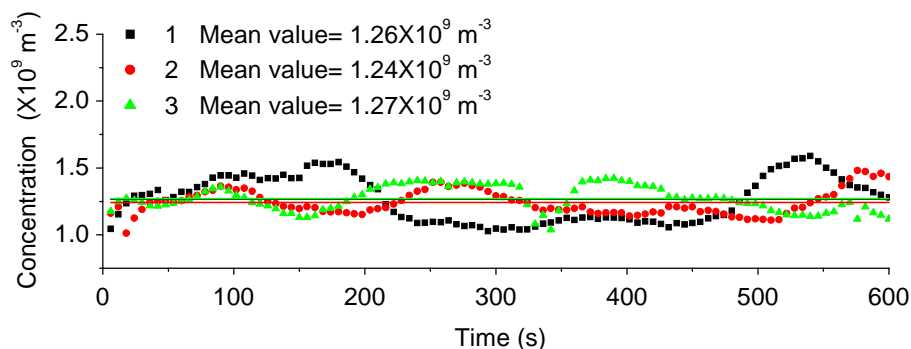


Figure 3-18: Test results for dust concentration at 50 mm height and 9000 rpm fan speed. The symbols are the raw data of dust concentration and the lines corresponding mean concentration.

### 3.2.2 Structure of wind field and dust concentration profile

One of the main goals of the wind tunnel experiment is to physically model the turbulent boundary layer. Based on the atmosphere boundary-layer theory, the profile of the mean horizontal wind under neutral conditions obeys the logarithmic law as Eq. (2.2) or Eq. (2.3).

To measure the wind profiles over different surfaces is an important part of the test. For the CSAT3 probe is too big to work near the surface, the particle-velocity measurements of the PDPA at different heights are used to infer to wind speed. The horizontal component of the particle velocity is considered to be identical to the local air speed. The results are shown in Figure 3-19, where the symbols are the PDPA data and the lines follow Eq. (2.2) or Eq. (2.3).

For low-roughness surfaces, such as water, wood, sand, and sandy loam, the PDPA wind profiles can be well fitted to Eq. (2.2), while for high-roughness surfaces, such as trees, the displacement height needs to be considered [Eq. (2.3)].

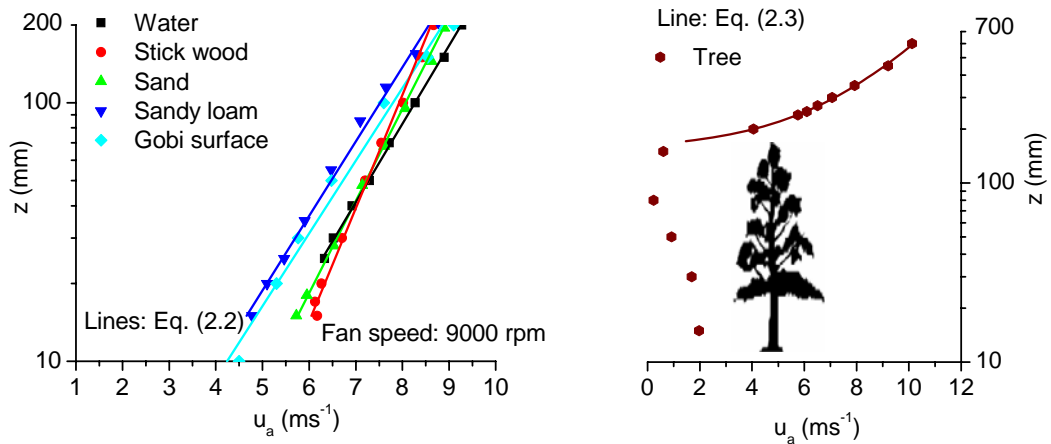


Figure 3-19: Wind profiles over different surfaces. The symbols are particle velocities extracted from the PDPA measurements and are used to represent the local winds. The lines are wind profiles fitted by Eq. (2.2) or Eq. (2.3) to the measurements.

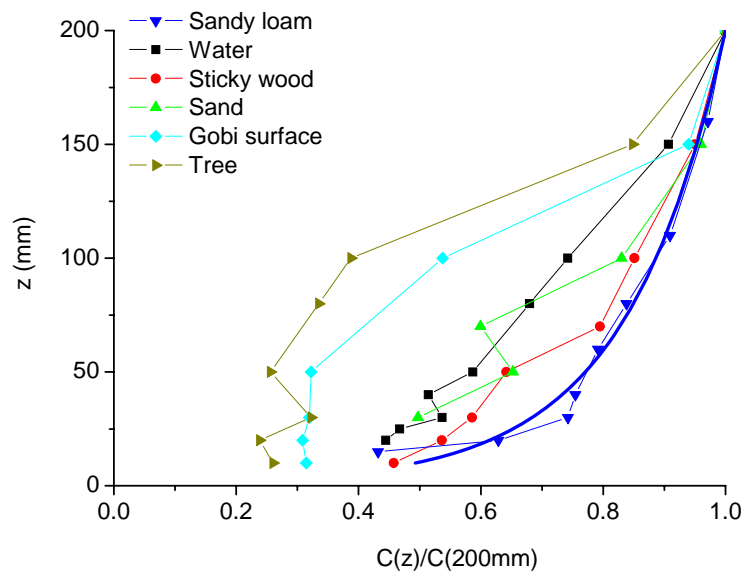


Figure 3-20: Normalized dust concentration profiles over different surfaces for a fan speed of 9000 rpm. The symbols are AS measurements and the blue line is an ideal profile, satisfied Eq. (2.23), over the sandy loam surface.

Dust concentration profile is measured by AS, over different surfaces for fan



speed of 9000 rpm. The dust profiles, normalized with dust concentration at 200 mm, are shown in Figure 3-20. The dust-concentration profiles with a positive gradient are successfully reproduced in the wind tunnel. The blue line in Figure 3-20 is an ideal concentration profile of dust driven by turbulent diffusion and gravitational settling with constant flux [i.e. satisfies the solution of Eq. (2.23)].

### **3.3 Summary**

In this chapter, the facilities and equipments for our wind-tunnel experiments are described. The components, principles and specifications of the instruments are presented. The design, purposes, configurations and procedures of the experiments are discussed. Also, the results of a series of test experiments are shown. It can be concluded that the wind-tunnel experimental conditions are similar to those of a neutral atmosphere boundary layer.



# Experimental Data and Scheme Validation

Deposition velocity is the quantity to be determined in this study, but it is not directly measured. A method is required to extract this quantity through a combination of the PDPA and AS measurements. In this chapter, we describe the methodology of data processing and compare the experimental results with the scheme estimates.

## 4.1 Methodology of data processing

### 4.1.1 Processing method for deposition velocity

A method is developed to derive deposition velocity from particle velocity and size which are directly measurable.

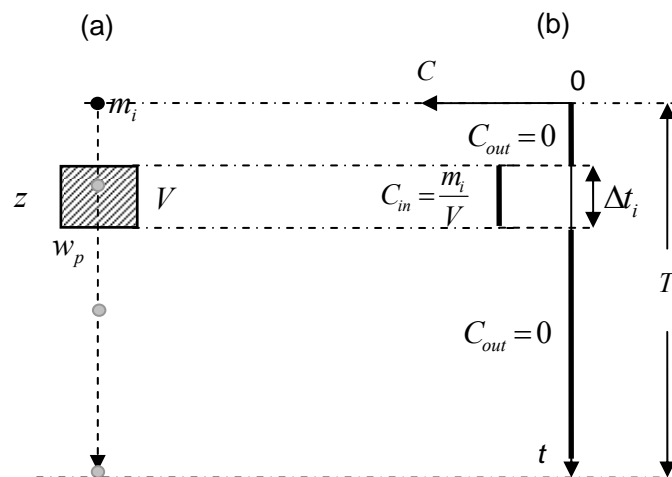


Figure 4-1: Illustration of one particle's contribution to concentration and flux. (a) Sampling area (shadow) and particle image; (b) Monitoring results of concentration.

We confine our discussion to the vertical direction. As shown in Figure 4-1, the sampling (shadow) area with volume  $V$  is monitored. If no particle appears in the area, then the concentration and velocity for this area are zero and, of course, no dust transfer occurs. If a particle (with index  $i$ ) of mass  $m_i$  passing through the sampling area with (vertical) velocity  $w_{pi}$ , then the corresponding concentration is  $m_i/V$  during the transit time  $\Delta t_i$  and deposition flux is

$$F_i = \frac{m_i}{V} \cdot w_{pi} \quad (4.1)$$

Suppose the sampling time interval is  $T$ , and  $N$  particles pass through the sampling area during this time interval. Then, the average flux  $F_d$  and concentration  $\bar{C}$  are respectively

$$F_d = \sum_{i=1}^N \left( F_i \cdot \frac{\Delta t_i}{T} \right) = \sum_{i=1}^N \left( \frac{m_i}{V} \cdot w_{pi} \cdot \frac{\Delta t_i}{T} \right) \quad (4.2)$$

$$\bar{C} = \sum_{i=1}^N \left( \frac{m_i}{V} \cdot \frac{\Delta t_i}{T} \right) \quad (4.3)$$

According to Eq. (2.4), the deposition velocity can be expressed by combining Eq. (4.2) and (4.3) as

$$w_d = \frac{\sum_{i=1}^N (D_{pi}^3 \cdot w_{pi} \cdot \Delta t_i)}{\sum_{i=1}^N (D_{pi}^3 \cdot \Delta t_i)} \quad \text{with } m_i \propto D_{pi}^3 \quad (4.4)$$

where  $D_{pi}$  (particle diameter),  $w_{pi}$  and  $\Delta t_i$  are measured simultaneously by the PDPA.

## 4.1.2 Quality control

### Error detection

The deposition velocity calculated with Eq. (4.4) includes the contributions of Brownian diffusion, eddy diffusion, gravitational settling and possibly mean vertical wind. The mean vertical wind is generally considered to be zero, but in our wind-tunnel experiment, it may be locally of the magnitude comparable with the

particle terminal velocity. Even if the average vertical wind is zero, error in flow measurements may still occur because a small alignment error in the PDPA vertical with respect to the surface normal may result in interpreting a component of the horizontal wind as the vertical wind and causing a serious bias in deposition velocity estimates. Therefore, we have to remove the effect of vertical mean wind,  $\bar{w}_a$ , from the PDPA measurements.

The particle velocity considered in this study,  $w_p$ , is defined from Euler's point of view. As shown in Figure 4-2a, a thin layer with thickness  $dz$  at height  $z$  is to be monitored. At time  $t_i$ , a particle  $i$  enters the layer and leaves it after  $\Delta t_i$ , and the particle velocity is  $w_p = w_{pi}$ . If no particle passes by, then  $w_p$  is zero. If there are more than one particle passing through this layer at same time, then  $w_p$  is the average velocity of all these particles. Suppose several particles pass through this layer at different times during the sampling time  $T$ . Then, the particle velocity  $w_p(z, t)$  and air velocity  $w_a(z, t)$  may behave as illustrated in Figure 4-2b. During each time interval, the particle velocity may relax to the local air velocity. But as particles are discrete, the particle velocities for different time intervals are initially independent.

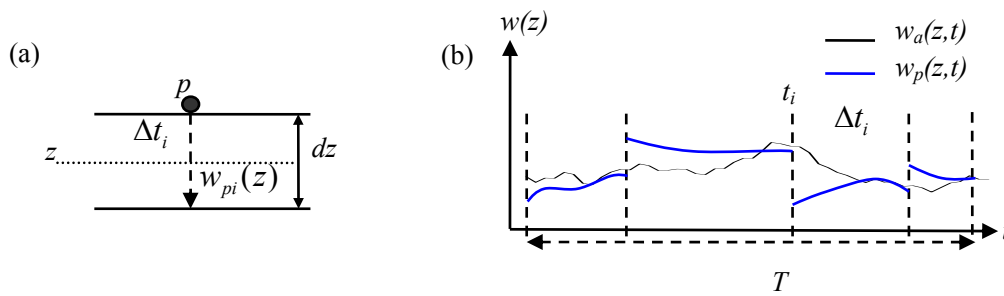


Figure 4-2: (a) Particle velocity for the sampling area; (b) Sketch of time series of air velocity (black line) and particle velocity (blue line) for the sampling area.

For the vertical particle velocity component, the equation of particle motion can be written as

$$\frac{dw_p(z, t)}{dt} = -g + \frac{w_p(z, t) - w_a(z, t)}{\tau_p} \quad (4.5)$$

Now we separate the motion of air into mean and fluctuating components by

$$w_a = \overline{w}_a \Big|_{\Delta t_i} + w'_a \quad (4.6)$$

where

$$\overline{w}_a \Big|_{\Delta t_i} = \frac{\int_{t_i}^{t_i+\Delta t_i} w_a(z, t) dt}{\Delta t_i}$$

is the mean of  $w_a$  over the time interval  $\Delta t_i$  and  $w'_a$  is the fluctuation. Likewise, the particle velocity  $w_p$  can be split into two parts:

$$w_p = \overline{w}_p \Big|_{\Delta t_i} + w'_p \quad (4.7)$$

Substituting Eq. (4.6) and Eq. (4.7) to Eq. (4.5), and averaging the latter over  $\Delta t_i$  yields

$$\overline{w}_p \Big|_{\Delta t_i} = \overline{w}_a \Big|_{\Delta t_i} + w_t \quad (4.8)$$

where terminal velocity  $w_t$  can be calculated with Eq. (2.8).

Eq. (4.8) is valid for  $\tau_p \ll \Delta t_i$ . If  $\Delta t_i$  is also sufficiently small and particles with the same properties (diameter, density and shape) pass the sampling area one by one, then

$$\sum_{i=1}^N \Delta t_i = T \quad (4.9)$$

Further, the sum of Eq. (4.8) over  $N$  particles gives

$$\sum_{i=1}^N (\overline{w}_p \Big|_{\Delta t_i} \cdot \frac{\Delta t_i}{T}) = \sum_{i=1}^N \overline{w}_p \Big|_{\Delta t_i} + w_t$$

i.e.

$$\overline{w}_p = \overline{w}_a + w_t \quad (4.10)$$

where  $\overline{w}_p$  and  $\overline{w}_a$  are mean particle and air velocities for the sampling area during monitoring time  $T$ , respectively.

The purpose of Eq. (4.10) is to estimate  $\overline{w}_a$  from the measurement of  $\overline{w}_p$  and  $w_t$  (function of particle size). So that  $\overline{w}_p$  is reliably determined, it requires the number of particles to be sufficiently large and the sampling is not biased. Unfortunately, the sampling is biased due to the vertical variation of dust particle

concentration. As shown in Figure 4-3, the dots represent the particle velocity measured by the PDPA, the solid line  $w_a+w_t$  and the red dashed line  $\bar{w}_p$ .

An iterative method is applied to determine the value of  $\bar{w}_p$ . For initialization,  $\bar{w}_p$  is set to  $(\bar{w}_p^+ + \bar{w}_p^-)/2$ , where  $\bar{w}_p^+$  and  $\bar{w}_p^-$  are respectively the mean values of all positive and negative particle velocities. Then, the full dataset for each run is divided into four sub-sets:

- (1)  $w_p \in (0, \bar{w}_p)$ ;
- (2)  $w_p \in (\bar{w}_p, 2\bar{w}_p)$ ;
- (3)  $w_p > 2\bar{w}_p$ , if  $\bar{w}_p > 0$  (or  $w_p < 2\bar{w}_p$ , if  $\bar{w}_p < 0$ ); and
- (4)  $w_p < 0$ , if  $\bar{w}_p > 0$  (or  $w_p > 0$ , if  $\bar{w}_p < 0$ ).

The number of measurements of sub-set  $j$  is counted and denoted with  $N_j$  ( $j=1, 2, 3, 4$ ). For sub-set  $j$  the average of particle velocity deviation  $\overline{w_p - \bar{w}_p}^{N_j}$  is calculated. Finally,  $\bar{w}_p$  is determined iteratively to satisfy

$$\overline{w_p - \bar{w}_p}^{N_2} \cdot \frac{N_2}{N_2 + N_3} + \overline{w_p - \bar{w}_p}^{N_3} \cdot \frac{N_3}{N_2 + N_3} = \overline{w_p - \bar{w}_p}^{N_1} \cdot \frac{N_2}{N_2 + N_3} + \overline{w_p - \bar{w}_p}^{N_4} \cdot \frac{N_3}{N_2 + N_3} \quad (4.11)$$

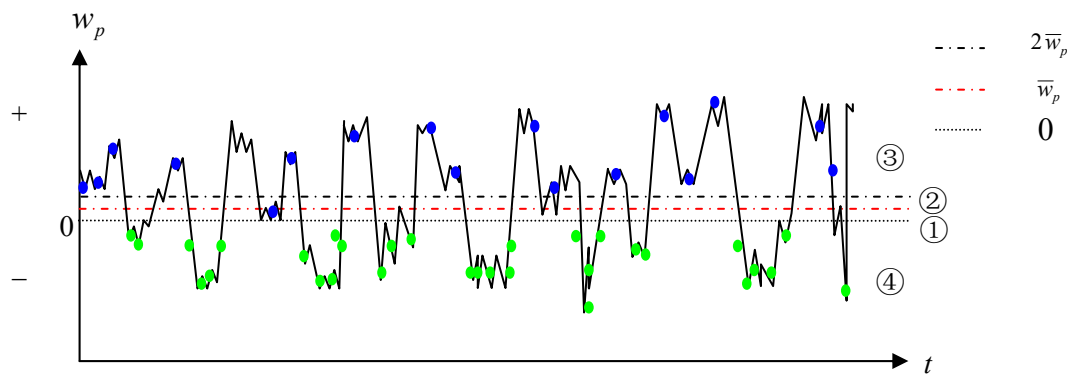


Figure 4-3: Illustration of the PDPA data of particle velocity. Dots are the PDPA measurements. Blue and green dots represent positive and negative particle velocities, respectively. The solid line is  $w_a+w_t$ . As an example for  $\bar{w}_p > 0$ , the whole dataset is divided into four parts: (1)  $0 < w_p < \bar{w}_p$ ; (2)  $\bar{w}_p < w_p < 2\bar{w}_p$ ; (3)  $w_p > 2\bar{w}_p$ ; and (4)  $\bar{w}_p < 0$ .

### Error correction

The method used to correct the estimated deposition velocity is to remove the mean particle velocity and then add back the gravitational settling velocity. Particles are divided into size groups, and for a given size group the deposition velocity can be modified from Eq. (4.4) to

$$w_d = \frac{\sum_{i=1}^N (D_{pi}^3 \cdot w_{pi} \cdot \Delta t_i)}{\sum_{i=1}^N (D_{pi}^3 \cdot \Delta t_i)} - \bar{w}_p + w_t \quad (4.12)$$

where  $\bar{w}_p$  is iteratively determined with Eq. (4.11) and  $w_t$  is computed with Eq. (2.8).

### Discussion of uncertainty

The PDPA cannot distinguish the particles appearing in the sampling area simultaneously and misinterprets these particles as one single large particle, causing uncertainties in its measurements. However, the volume of the sampling area is  $4.55 \times 10^{-11} \text{ m}^3$  and the number concentration of dust in our experiments is about  $10^9$ , the possibility for more than one particle appearing in the sampling area simultaneously is very low.

Although the low dust concentration has little effect to degrade the precision of the PDPA, it affects the number of particles sampled by the PDPA. Indeed, the number of big particles (e.g. bigger than  $50 \mu\text{m}$ ) sampled by the PDPA is very low with respect to the size distribution of the dust used for our experiments. This may lead to a serious uncertainty for the estimation of the mean motion for these big particles [Eq. (4.11)], because of the low sample space. However, since the terminal velocity is calculated theoretically and is dominant for big particles [Eq. (4.12)], this uncertainty remains relatively small value.

#### 4.1.3 Method of data process

The raw data of the PDPA includes the diameter, velocity and transit time of the particles which pass the sampling area. The whole data is divided into a number of



particle size groups. The following size channels are considered: 0.5- 1.5- 3- 5- 10- 15- 20- 25- 30- 50- 80- 100- 150- 200  $\mu\text{m}$ . For each channel, the particles are considered to be mono-dispersed with the median size of each channel, i.e., 1, 2.25, 4, 7.5, 12.5, 17.5, 22.5, 27.5, 40, 65, 90, 125 and 175  $\mu\text{m}$ . Then, the deposition velocity for each particle size group is obtained by using Eq. (4.12).

## 4.2 Results and comparison with schemes

### 4.2.1 Dust deposition on water surface

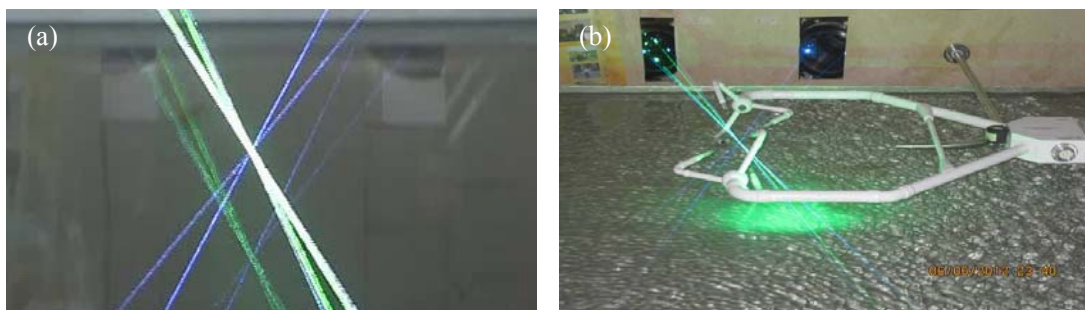


Figure 4-4: Dust deposition measurement over water surface. (a) Flat water surface under zero wind speed. (b) Wavy water surface under high wind speed.

Water is a special surface with perfectly wet and sticky characteristics. The shape of the water surface changes with the speed of the airflow. If there is no airflow, then the water surface is flat and smooth (Figure 4-4a), but in case of airflow, waves develop (Figure 4-4b) and change the capacity of the water surface to absorb momentum. A wavy water surface also has higher capacity of collecting dust particles. Besides, if the particles are hygroscopic, their sizes will increase under the high humid condition and thereby enhancing the effect of gravitational settling.

The wind profiles over the water surface are shown in Figure 4-5 for three different fan speeds. As shown, the profiles obey the logarithmic law (Eq. (2.2)) very well. Both the friction velocity and roughness length (determined by fitting Eq. (2.2) to the measurements) increase with the fan speed. These results indicate that the wavy water surface indeed enhances air turbulence and the momentum transfer downwards.

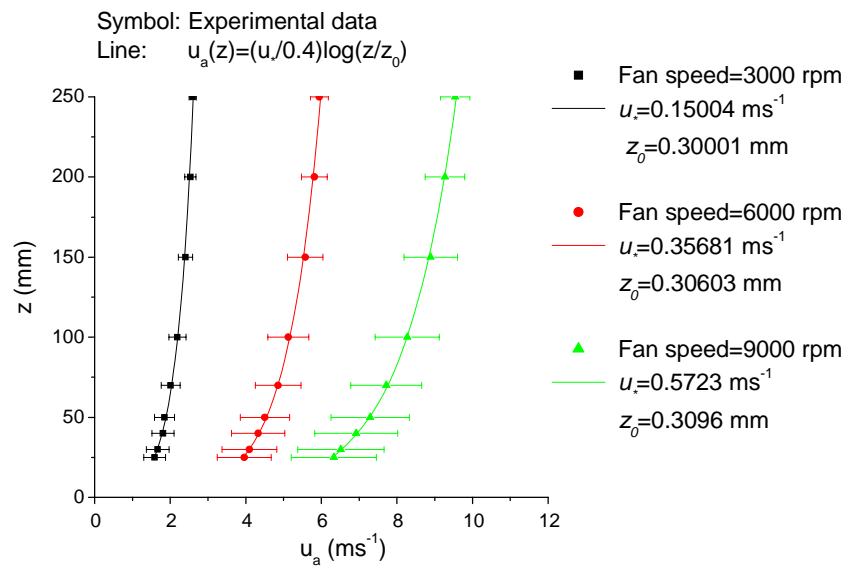


Figure 4-5: Wind profiles measured over the water surface. The symbols are the mean horizontal speed of the particles which pass the measurement point and are used to represent the local horizontal air speed. The error bars show the standard deviation of the speed. The curves are wind profiles fitted to the logarithmic law. The fan speeds are set to 3000, 6000 and 9000 rpm for the three experiments.

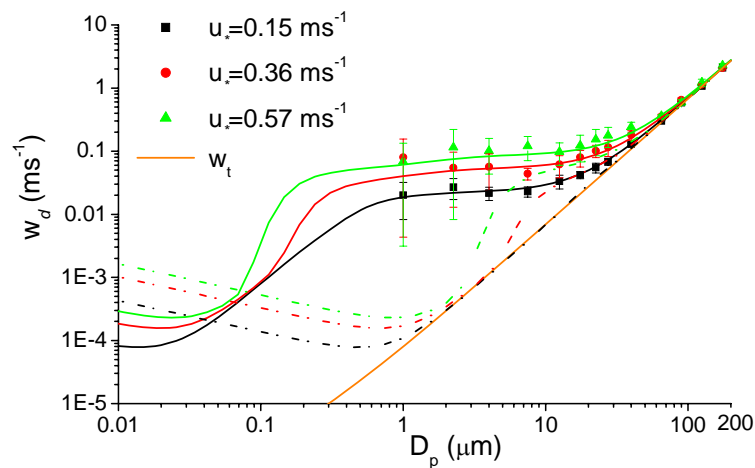


Figure 4-6: Deposition velocity against particle size under different wind conditions over water surface. The symbols are averaged results of  $w_d$  and the error bars represent the variability of the results. The curves are the results predicted with the SS80 scheme. The solid lines are obtained with  $\text{RH} = 100\%$ , and the dashed lines with  $\text{RH} = 0\%$ . The height of the measuring point is 25 mm above the water surface.

The deposition velocities at 25 mm over the water surface are shown in Figure 4-6 as function of particle diameter. For particles in the size range between 1 and 12.5  $\mu\text{m}$ , the values of deposition velocity are close to each other. For  $u_* = 0.15 \text{ m}\cdot\text{s}^{-1}$ , deposition velocity is about  $0.02 \text{ m}\cdot\text{s}^{-1}$ . Similarly, for  $u_* = 0.36 \text{ m}\cdot\text{s}^{-1}$ , we have  $w_d = 0.05 \text{ m}\cdot\text{s}^{-1}$  and for  $u_* = 0.57 \text{ m}\cdot\text{s}^{-1}$ ,  $w_d = 0.10 \text{ m}\cdot\text{s}^{-1}$ . The values of the deposition velocity obtained in this study are obviously higher than those reported in the literature, e.g., the deposition velocity measured by Sievering (1981) at 2m over a lake surface is  $(0.7 \pm 0.3) \times 0.006 \text{ m}\cdot\text{s}^{-1}$  for the aerosol particles in the size range of 0.6 and 1.5  $\mu\text{m}$ . This may be attributed to that the measuring point in our experiment is closer (25mm) to the surface.

Error bars are also shown in the figures to indicate the variabilities of the measurements. The wind speed shown in Figure 4-5 is represented by the particle velocity measured by the PDPA. Generally, the number of the measurements for each height is more than 5000, which is enough to estimate the variability. But for deposition velocity (i.e. Figure 4-6), there are only three repeated measurements for each particle size. So the error bars in Figure 4-6 (also for the other similar figures in this thesis) are only indicative of the variability among the repeated measurements rather than a statistically meaningful evaluation.

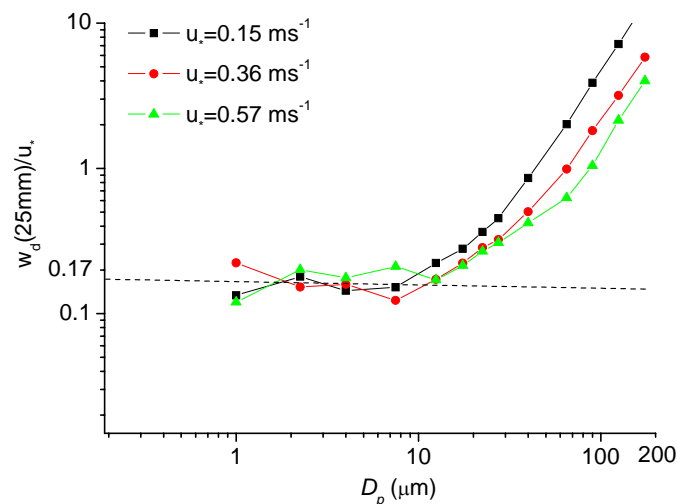


Figure 4-7: Dust deposition velocity normalized with friction velocity as a function of particle size.

As shown, dust deposition velocity increases with friction velocity. For particles in the size range of 1 to 12.5  $\mu\text{m}$ , the deposition velocities, normalized with  $u_*$ , are almost a constant of 0.17 (Figure 4-7).

SS80 proposed a scheme for particle deposition for water surfaces. They treated water as a flat, sticky and wet surface. The mechanisms of turbulence transfer, gravitational settling, Brownian diffusion, impaction and particle size growth are considered (refer to Section 2.3.2b). Using the wind-tunnel flow field parameters, the deposition velocities estimated by using the SS80 scheme are also shown in Figure 4-6. If the relative humidity (RH) of the air near the surface is set to 0%, then the scheme obviously underestimates the deposition velocities (dashed line in Figure 4-6). If RH is set to 100%, the effect of particle growth is considered and the predicted results (solid line in Figure 4-6) agree better with the measurements. A problem is, however, that the mechanism of particle growth embedded in the scheme is introduced for predicting the behavior of hygroscopic particles, not for the Silicon Dioxide ( $\text{SiO}_2$ ) particles used in our experiments. Hence, the effect of particle growth is overestimated by the scheme. On the other hand, the effect of waves and bubbles or spray droplets emitted from the water surface, which should be important for dust deposition, is neglected in the scheme. This implies that the good agreement between the scheme and the measurements is achieved by setting  $\text{RH} = 100\%$  for the wrong reason.

#### 4.2.2 Dust deposition on sticky and smooth surface

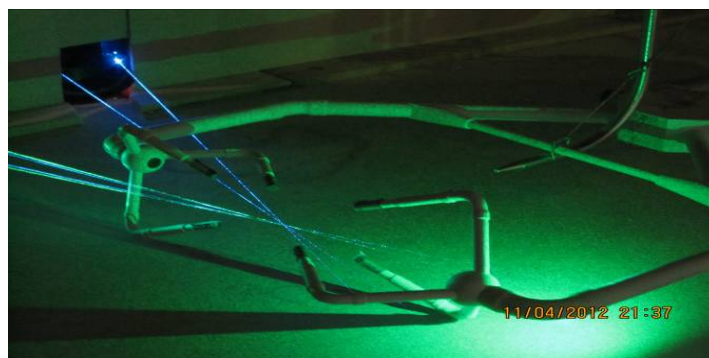


Figure 4-8: Measurement above smooth wood plane. The plane is oiled and sticky.

For a sticky and smooth surface, particle rebound and element collection do not occur. Hence, dust deposition to such a sticky and smooth surface is determined by gravitational settling, Brownian diffusion and impaction.

The wind profiles over the sticky and smooth wood surface, shown in Figure 4-9, also obey the logarithmic law. Similar to the water surface case, the friction velocity also increases with fan speed. But the roughness length is smaller than the wavy water surface and decreases with friction velocity. This increase in friction velocity and decrease in roughness length indicate that intensified turbulence intrudes into the layer adjacent to the surface and reduces the thickness of the laminar layer, and enhances dust deposition.

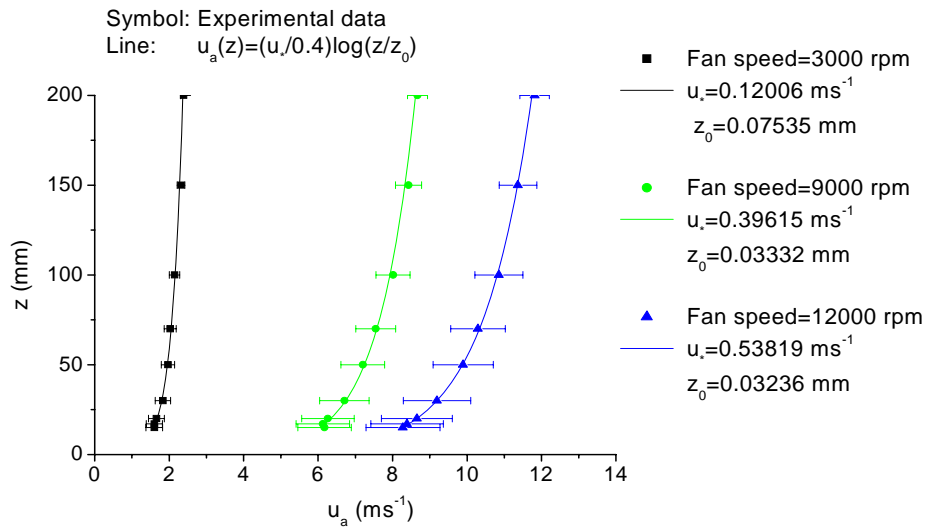


Figure 4-9: As Figure 4-5, but is for sticky and smooth wood surface and fan speed of 3000, 9000 and 12000 rpm.

Figure 4-10 shows the observed deposition velocity for the wood surface. As can be seen, deposition velocity is small for low friction velocity and increases with friction velocity. This is most obviously for particles in the size range of 4 to 22.5  $\mu\text{m}$ , because turbulent impaction is effective for this particle size range and is sensitive to friction velocity. The SS80 scheme originally proposed for water surfaces can also be applied to other smooth surfaces but without particle growth. The predictions of the SS80 scheme are also shown in Figure 4-10. The scheme estimates are comparable to

the measurements and are somewhat smaller. It is perceivable that the underestimation of the deposition velocity by the scheme is caused by the underestimation of the effect of turbulent transfer in high layer or turbulent impaction in low layer.

Besides, the measured deposition velocities for small particles (about  $1\ \mu\text{m}$ , as shown in the lower right corner of Figure 4-10) under higher friction velocity are negative. This may be caused by the re-suspension of the deposited particles.

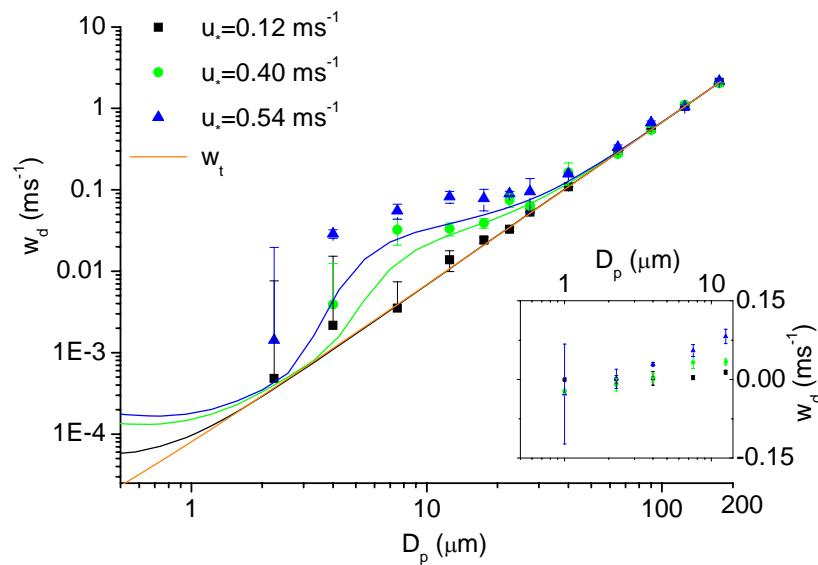


Figure 4-10: As Figure 4-6, but is for sticky and smooth wood surface and measurement height 15 mm.

### 4.2.3 Dust deposition on low-roughness surface



Figure 4-11: Deposition measurement over the sand surface.

The common characteristics of the low-roughness surfaces, including the sand, sandy loam and Gobi surfaces tested in our experiments, is that they can be considered as a flat surface superposed with some roughness elements. These roughness elements, although small in height, enhance turbulence in the surface layer and the collection efficiency of the surface.

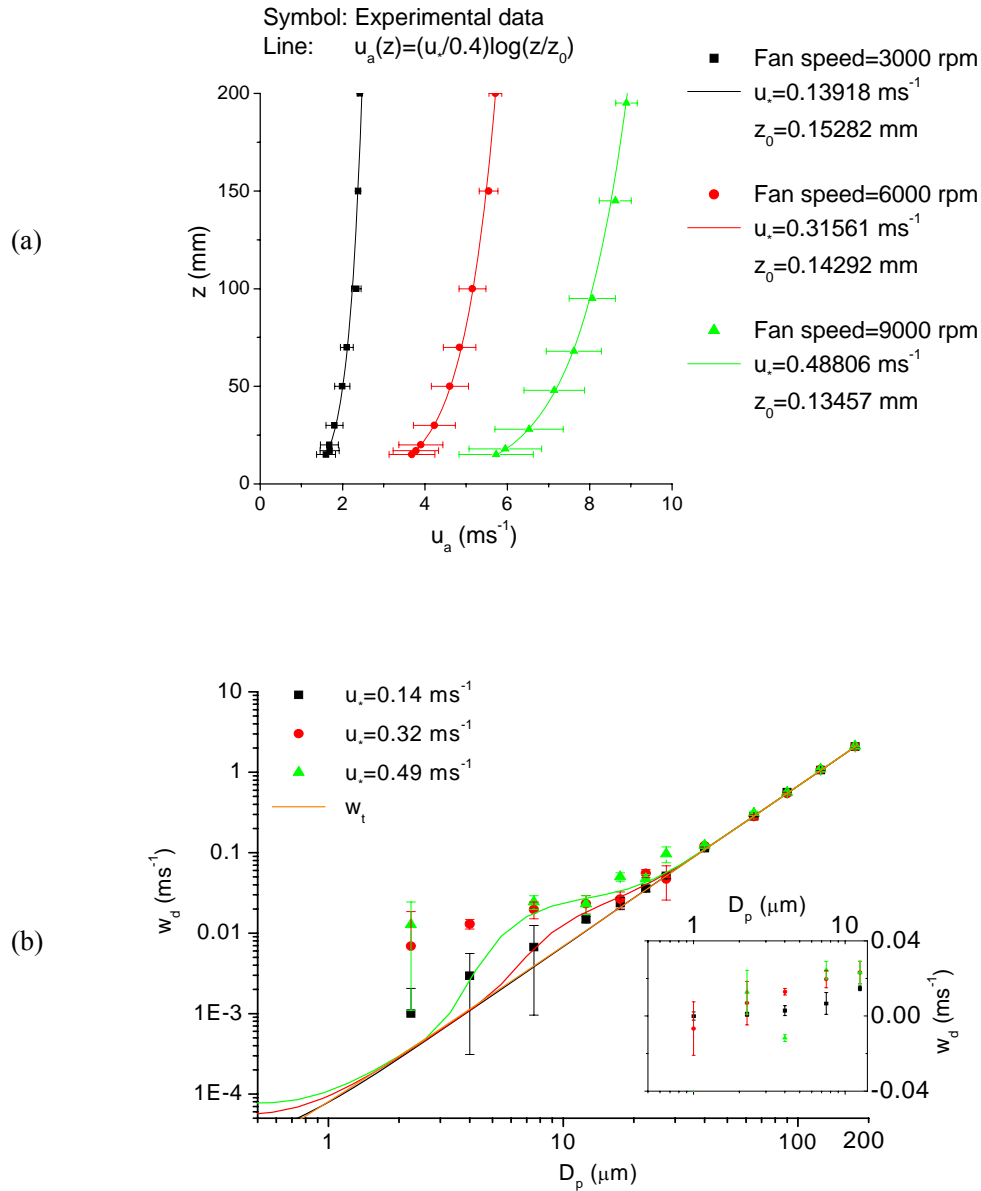


Figure 4-12: Measurements of dust deposition to the sand surface. (a) As Figure 4-5, but is for sand surface. (b) As Figure 4-6, but is for sand surface and the height of measuring point is 15 mm.

In comparison to the wood surface, the roughness length of the sand surface is larger (Figure 4-12a). The corresponding enhancement of air turbulence is reflected in the increased friction velocity. Before the experiment, the sand surface is wetted and then air-dried, so that a crust forms to suppress the motion of sand particles during the measurement. The observed and the SS80 scheme predicted deposition velocities are shown in Figure 4-12b. The measurements show that the deposition velocity for the sand surface increases with particle size and friction velocity. The main difference between the sand and wood surface is that the deposition velocities do not markedly decrease for particles smaller than  $4\ \mu\text{m}$ . This can be attributed to the contribution of elements (sand particles) collection. It appears that the SS80 scheme cannot well predict the deposition velocity for the particles less than  $4\ \mu\text{m}$ , because the effect for element collection is neglected.

Deposition over the sandy loam and Gobi surfaces are similar to that over the sand surface, but the process seems to be enhanced for the rougher surface (Figure 4-13).

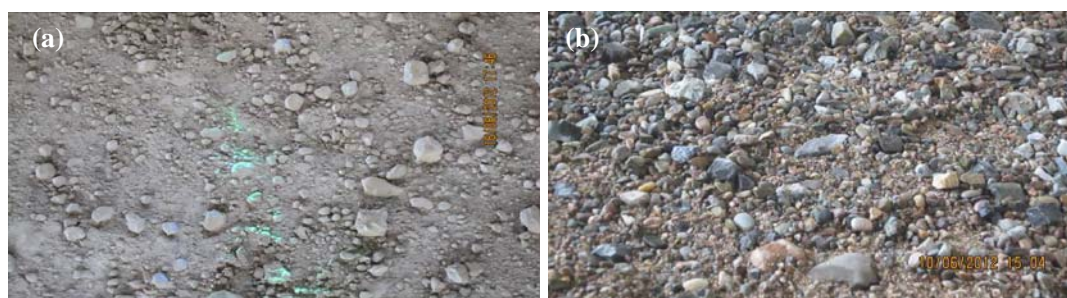


Figure 4-13: (a) Sandy loam and (b) Gobi surface used in the wind-tunnel experiments.

Before the experiment, the sandy loam and Gobi surfaces are exposed under high wind speed for about 5 minutes to remove the loose particles, so that few particles are released from the surface during the experiments to disturb the observations. The experimental data for the sandy loam and Gobi surfaces are shown in Figure 4-14.

As shown in Figure 4-14a and 4-15a, the wind profiles over the sandy loam and Gobi surfaces follow Eq. (2.2). Over the sandy loam surface, the deposition velocity increases with particle size and friction velocity. Compared to the sand surface (Figure 4-12), dust deposition is enhanced because of the rougher surface and stronger turbulence. Over the Gobi surface, air turbulence is further enhanced and hence,



deposition velocity further increased except for the case of  $u_* > 0.67 \text{ m}\cdot\text{s}^{-1}$ , due to dust re-suspension.

The measurements also show that the rougher the surface, the higher friction velocity (for given fan speed), and hence the higher the deposition velocity is.

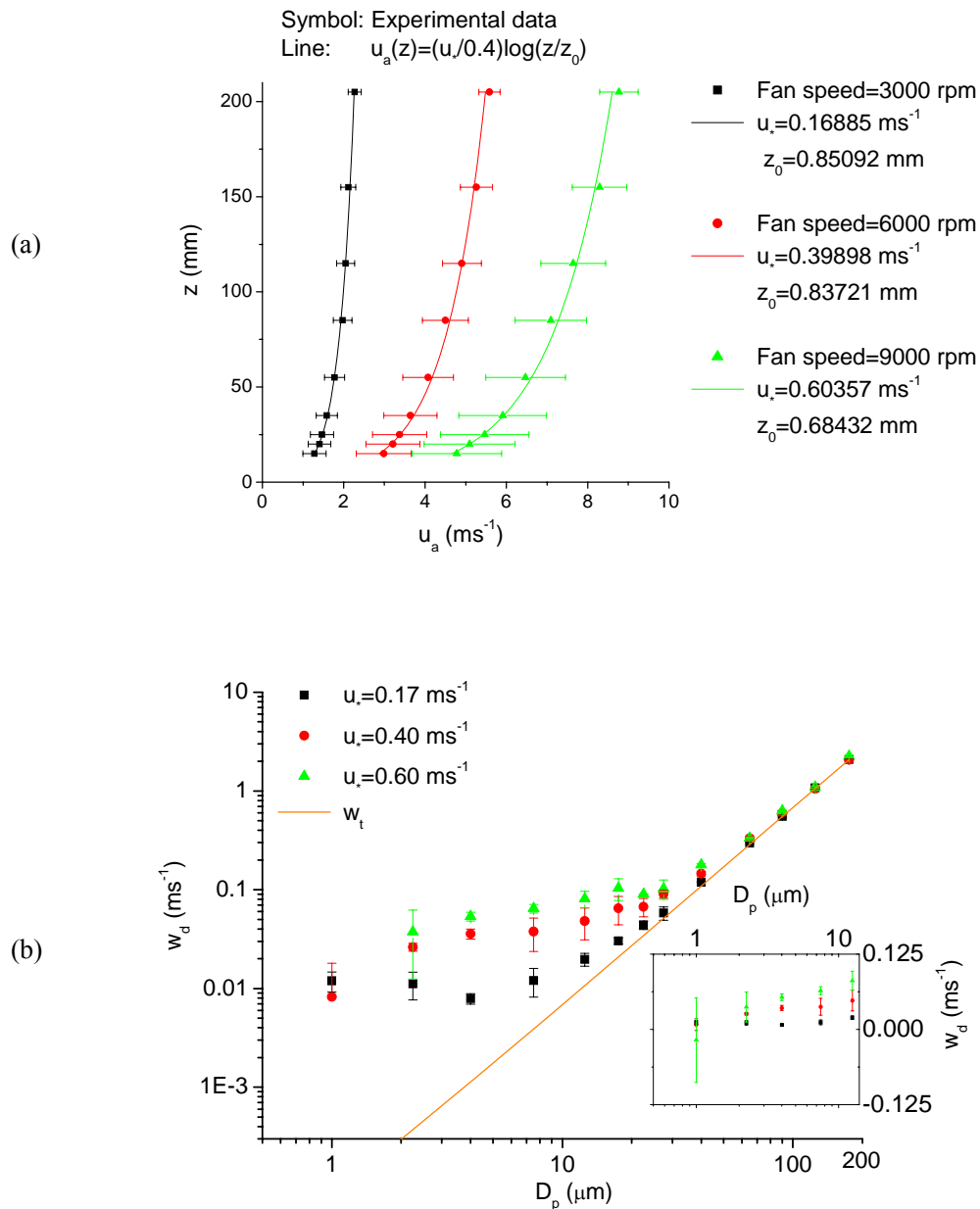


Figure 4-14: Deposition to sandy loam surface. (a) Wind profile; (b) Deposition velocity.

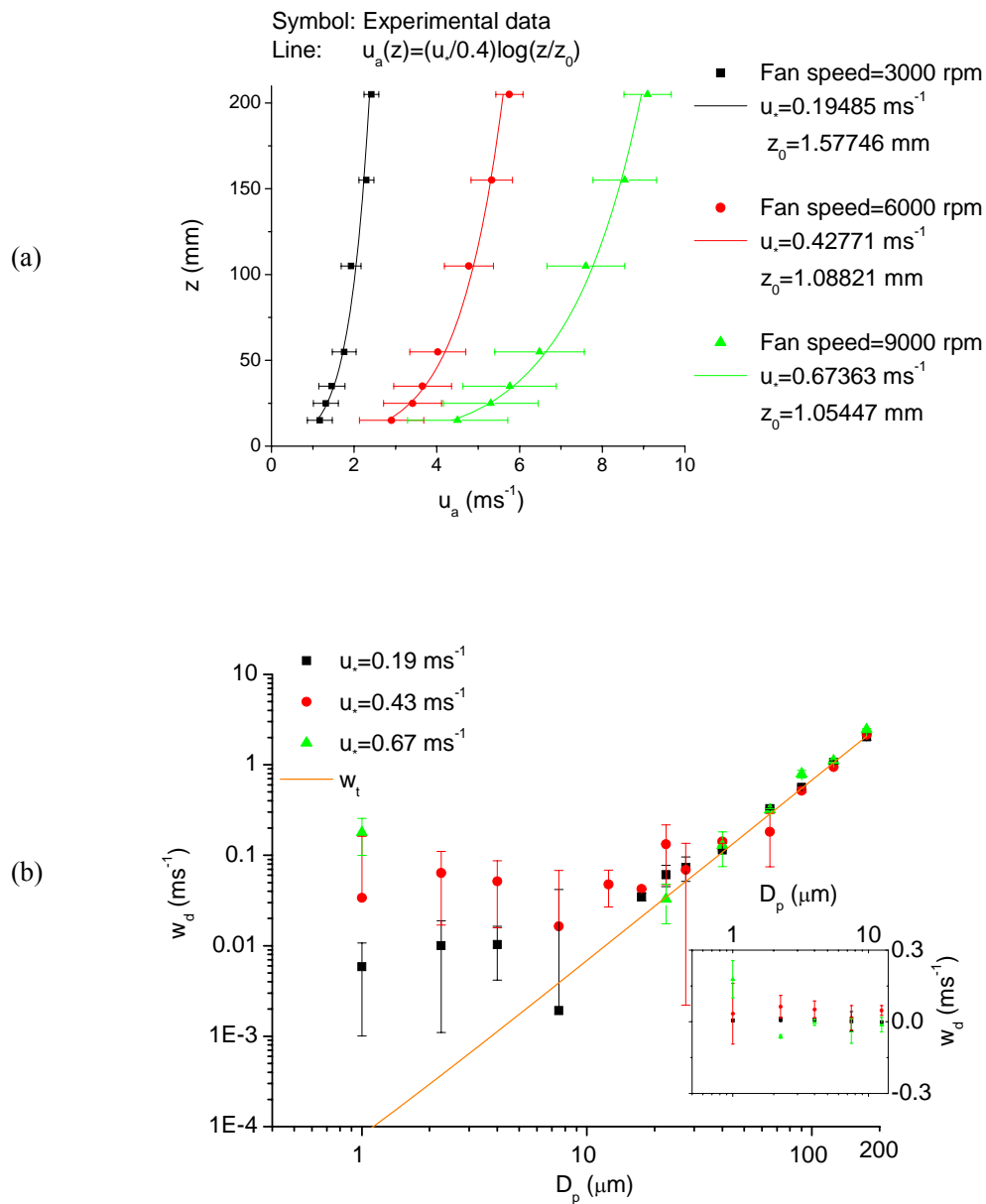


Figure 4-15: Deposition to Gobi surface. (a) Wind profile; (b) Deposition velocity.

#### 4.2.4 Dust deposition on canopy surface

Artificial plastic trees of 230 mm high are fixed on the floor of the working section in the wind tunnel, with a spacing of 200 mm, to imitate forest canopies (Figure 4-16).

The trees are oiled before the experiment to avoid particle rebound.



Figure 4-16: Surface with artificial trees tested in the wind-tunnel experiments.

The wind profiles over the tree surface are shown in Figure 4-16. For the region above the canopy, the profiles follow the logarithmic law. By fitting the experimental data to Eq. (2.3) and setting the zero-plane displacement height to 200 mm, the parameters of the wind field, such as friction velocity and roughness length, are obtained as shown in Figure 4-17. Below the canopy, the wind profiles fit to  $u(z)/u(h_c) = \exp[-\gamma(1-z/h_c)]$  (S82) and the  $\gamma$  parameter estimated from the fitting. As shown, the friction velocity increases with the fan speed, but the roughness length becomes smaller for higher fan speed. The  $\gamma$  values fall in the range of 3.5 to 4.5.

The deposition velocity measurements for the tree surface are shown in Figure 4-18. Deposition velocity increases with particle size and friction velocity. Not only the particles bigger than  $4 \mu\text{m}$ , but also the smaller ones in the range of 1 to  $4 \mu\text{m}$  have a considerable deposition velocity.

The predicted results with the S82 scheme are also shown in Figure 4-18. The wind parameters required by the scheme are obtained from the wind profiles shown in Figure 4-17. The surface parameters, such as the characteristic dimension of the large collectors ( $d_c^l = 5 \text{ mm}$ ), and that of the small collectors ( $d_c^s = 100 \mu\text{m}$ ), are evaluated according to the size of the artificial trees employed in the experiments.  $c$ , the fraction of the total interception by the small collectors, is hard to estimate and is set to 1% following S82.

As shown, the results of the S82 scheme agree with the experimental data well for the cases of low friction velocity. For the cases of high friction velocity, the scheme underestimates the deposition velocity and the scheme-measurement discrepancy increases with the friction velocity. However, if the effect of interception is made

larger in the scheme by decreasing 2 orders of magnitude of  $d_c^s$ , then the predicted results agree better with the measurements. This implies that the effect of interception is related to friction velocity and is underestimated in the S82 scheme.

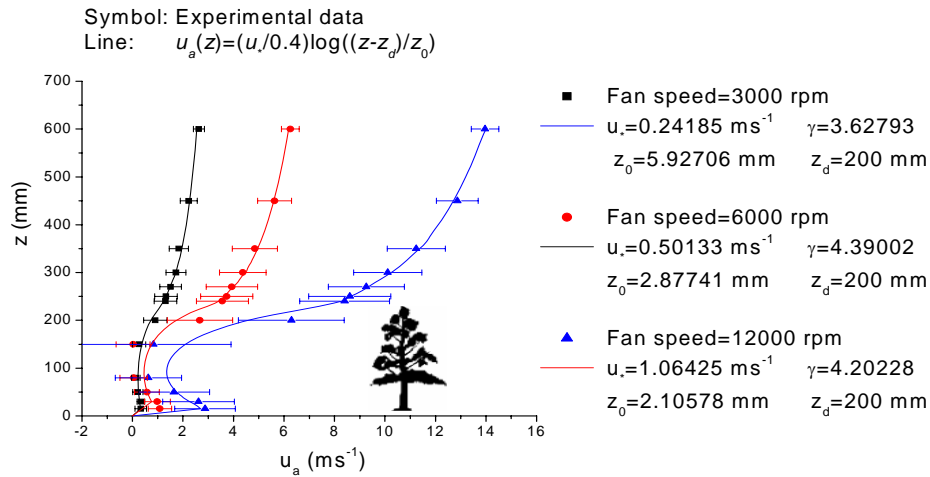


Figure 4-17: As Figure 4-9, but is for the tree surface and the wind profiles over the canopy are fitted to Eq. (2.3). The zero-plane displacement height is set to 200 mm. The wind profiles under the trees are fitted to  $u(z)/u(h_c) = \exp[-\gamma(1-z/h_c)]$  (S82) where  $h_c$  is the height of the trees.

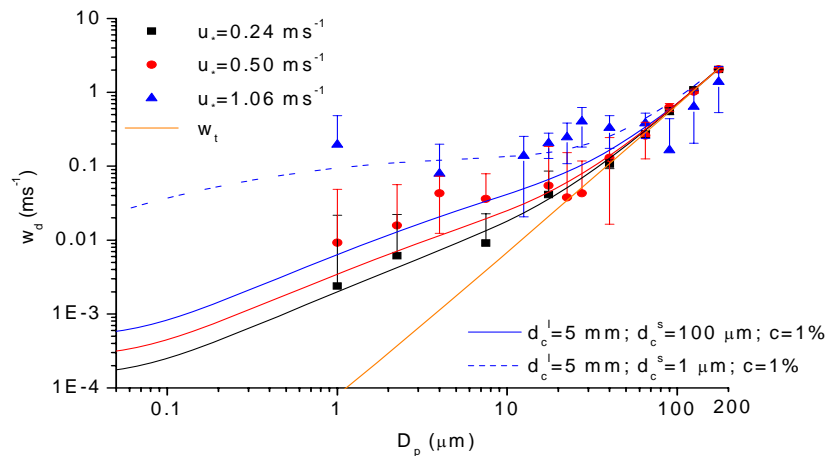


Figure 4-18: As Figure 4-9, but is for tree surface.  $d_c^l$  and  $d_c^s$  are respectively the sizes of the large and small collectors.  $c$  is the fraction of the total interception by the small collectors. By decreasing  $d_c^s$  so that the effect of interception is increased, the S82 scheme can be made to agree with the experimental data (dashed line).

### 4.3 Conclusions

The experimental results show:

- Over water surface, the deposition velocities for the particles in the size range of 1 to 12.5  $\mu\text{m}$  do not significantly differ from each other and their values increase almost linearly with friction velocity;
- Deposition velocity for particles in the size region of 1 to 40  $\mu\text{m}$  over dry surface increases with particle size and friction velocity;
- Impaction is sensitive to friction velocity and is important for the deposition of particles in the size range of 4 to 22.5  $\mu\text{m}$ . Both turbulent impaction and element impaction must be considered for deposition to rough surfaces;
- Interception is effective for particles in the size range of 1 to 4  $\mu\text{m}$  and is sensitive to friction velocity, especially for the canopy surface.

The schemes of SS80 (for smooth surface) and S82 (for canopy) are tested against the experimental data:

- The deposition velocity on water surface can be well predicted by the SS80 scheme, but the effect of particle growth is overestimated for hydrophobic particles. The contribution of waves and bubbles or spray droplets emitted from water surface is neglected in the scheme, but is important to deposition on the water surface. The SS80 scheme somewhat underpredicts the deposition velocity for the sticky and smooth wood surface;
- The SS80 scheme underestimates deposition velocity over low-roughness surfaces, especially for particles smaller than 7.5  $\mu\text{m}$ ;
- The S82 scheme can well predict the deposition velocity over the canopy surface for low friction velocity, but underestimates for high friction velocity. The scheme-measurement disagreement increases with friction velocity. The S82 scheme can well predict the deposition velocity over the canopy surface for low friction velocity, but underestimates for high friction velocity. The scheme-measurements disagreement increases with friction velocity.



## Chapter 5

# Improved Parameterization

An improved dust deposition scheme is introduced in this chapter. It is a two-layer scheme for rough surfaces but reduces to a parameterization for smooth surfaces. Dust deposition velocity is determined by solving the equation for particle motion and is expressed as a function of resistance series. A new parameterization for surface resistance is proposed based on the surface collection mechanisms and the aerodynamic effect of surface roughness elements. Based on this surface parameterization method, a new dust dry deposition scheme is then proposed and is tested against the experimental data presented in the previous chapters. Finally, the driving parameters of the new scheme are identified through a sensitivity analysis.

## 5.1 Scheme improvement

### 5.1.1 Assumptions

The surface is supposed to be a flat ground surface superposed with roughness elements (e.g. trees) which will be simply referred to as roughness elements to facilitate description. It is assumed that the wind field is in steady state and horizontally homogeneous. The size and distribution of the roughness elements on the surface are assumed to be uniform (homogeneity). It is further assumed that the dust flux is vertically constant.

### 5.1.2 Framework of the new model

The atmospheric boundary layer is divided into two parts (Figure 5-1). The lower part is the collection layer with thickness of

$$h = h_c + \delta \quad (5.1)$$

where  $h_c$  is the element height and  $\delta$  the thickness of the laminar layer over the elements. The laminar layer may be broken at the top of the elements and  $h_c$  is usually much larger than  $\delta$ . Therefore, in general, the thickness of the collection layer is  $h_c$  for a rough surface and  $\delta$  for a smooth surface. The dust collection process takes place in this layer.

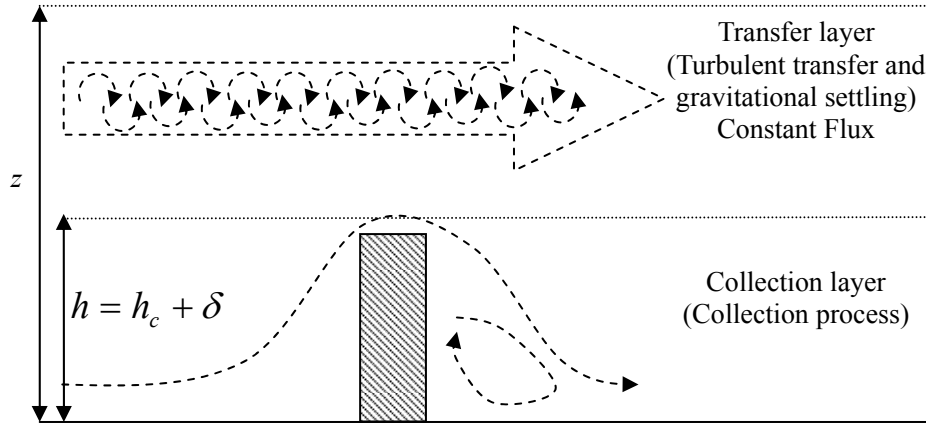


Figure 5-1: Illustration of the two-layer model. The lower layer, from the ground to the top of the quasi-laminar layer, is the collection layer where the dust collection process takes place. Over the collection layer is the transfer layer, where turbulent transfer and gravitational settling are dominant and the dust flux is vertically constant. Air flow is represented by the dash lines.

The upper part above the collection layer is the transfer layer. In this layer, dust is transported mainly by eddy diffusion and gravitation settling and the dust flux is vertically constant.

Based on the assumptions of steady state and horizontal homogeneity, the dust flux,  $F_d$ , in the transfer layer obeys Eq. (2.23). Since the formulation of the earlier resistance-based schemes (i.e. Eq. (2.45)) does not satisfy the mass conservation requirement of Eq. (2.23), we estimate dust deposition velocity by directly solving Eq. (2.23) and have found that

$$w_d(z) = \left( r_g + \frac{r_s - r_g}{\exp(r_a / r_g)} \right)^{-1} \quad (5.2)$$

with boundary condition  $C(h) = F_d / w_d(h)$ .  $r_a$  is the aerodynamic resistance,



accounting for the turbulent dust diffusion

$$r_a(z) = \int_h^z \frac{1}{K_p(z) + k_p} dz \quad (5.3)$$

$r_g$  is the gravitational resistance defined as the inverse of the terminal velocity

$$r_g = \frac{1}{w_t} \quad (5.4)$$

and  $r_s$  is the surface collection resistance which can be calculated by

$$r_s = \frac{1}{w_d(h)} = \frac{C(h)}{F_d} \quad (5.5)$$

### 5.1.3 Parameterizations

#### Aerodynamic resistance $r_a$

In the transfer layer,  $k_p$  is much smaller than  $K_p$ . It follows from Eq. (5.3) that

$$r_a(z) \approx \int_h^z \frac{1}{K_p(z)} dz \quad (5.6)$$

According to Eq. (2.20) and Eq. (2.21),  $K_p$  can be calculated as

$$K_p = \left(1 + \frac{\beta^2 w_t^2}{\sigma^2}\right)^{-1/2} \cdot K_T \quad (5.7)$$

where  $K_T$  is the eddy viscosity,  $\beta$  a dimensionless coefficient and  $\sigma$  the standard deviation of the turbulent velocity. In this study,  $\beta$  is taken as 1 and  $\sigma$  as friction velocity  $u_*$ .

For a neutral atmospheric boundary layer, we take

$$K_T = ku_*(z - z_d)$$

where  $k$  is the von Karman constant, and  $d$  the zero-plane displacement height.

Then integrating Eq. (5.6) yields

$$r_a(z) = \frac{1}{Sc_T \cdot ku_*} \ln\left(\frac{z - z_d}{h - z_d}\right) \quad (5.8)$$

As  $h$  is about  $h_c$ , we have

$$r_a(z) = \frac{1}{Sc_T \cdot ku_*} \ln\left(\frac{z - z_d}{h_c - z_d}\right) \quad (5.9)$$

For a smooth surfaces  $h$  is approximately  $\delta$  and  $z_d$  is zero, and thus

$$r_a(z) = \frac{1}{Sc_T \cdot ku_*} \ln\left(\frac{z}{\delta}\right) \quad (5.10)$$

As it is difficult to obtain the exact value of  $\delta$ , Eq. (5.10) can be approximately written as

$$r_a(z) = \frac{B_1}{Sc_T \cdot ku_*} \ln\left(\frac{z}{z_0}\right) \quad (5.11)$$

with  $B_1$  being an empirical constant determined by the airflow characteristic over the surface. The term  $B_1/Sc_T$  is set to 0.6 for SS80 and 1 for Zhang et al. (2001). In this study, the value of  $B_1$  is estimated to be 0.45, based on the measurements over the water surface.

### Gravitational resistance $r_g$

In the Stokes regime,  $r_g$  can be calculated as

$$r_g = \frac{18\mu}{C_c \rho_p D_p^2 g} \quad (5.12)$$

where  $\mu$  is air viscosity,  $C_c$  the Cunningham correction factor which accounts for non-continuum effects when calculating the drag on small particles,  $D_p$  particle diameter,  $\rho_p$  particle density and  $g$  gravitational acceleration.

### Surface collection resistance $r_s$

#### Parameter of surface

As illustrated in Figure 2-3, a rough surface can be considered to be a smooth surface superposed with elements. Apart from roughness element size (height  $h_c$  and diameter  $d_c$ ), roughness frontal area index,  $\lambda$ , is introduced to characterize the rough surface.

For cylindrical elements,  $\lambda$  can be expressed as

$$\lambda = nh_c d_c \quad (5.13)$$

where  $n$  is element number density (number of elements per unit area, Figure 5-2).

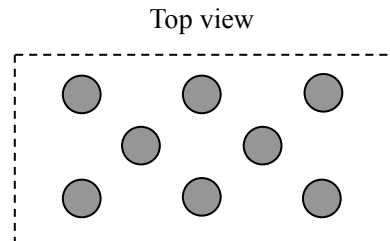


Figure 5-2: A unit area homogenous surface with  $n$  uniform roughness elements.

### Drag partition

We first consider the process of momentum transfer over a rough surface. Momentum flux is generated by eddy diffusion and Brownian diffusion, equivalent to a shear stress consisting of the Reynolds shear stress (caused by eddy diffusion) and viscous shear stress (caused by Brownian diffusion). The momentum transferred downwards is finally absorbed by the surface.

On the rough surface, the total momentum flux is absorbed by different parts of the surface and the total shear stress (or drag) can be split into three parts to represent the relevant contributions to the depletion:

$$\tau = \tau_c + \tau_s + \tau_r \quad (5.14)$$

where  $\tau_c$  is the form or pressure drag exerted on the roughness element,  $\tau_s$  is the ground surface drag due to the momentum transfer to the ground surface and  $\tau_r$  is the roof surface drag due to the momentum transfer to the roof of the roughness elements, as illustrated Figure 5-3.

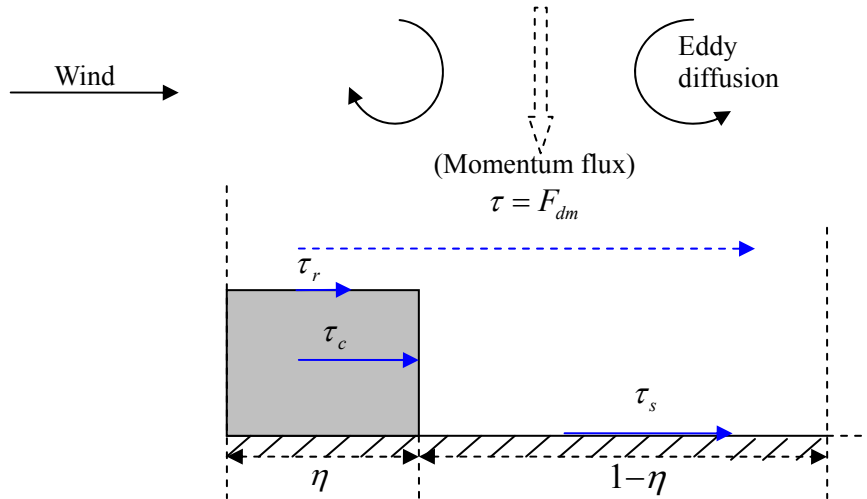


Figure 5-3: Conceptual map for drag partitioning over a rough surface. Shaded area represents the fraction of roughness elements on surface.  $\eta$  is the basal area index representing the fractional surface occupied by the elements. Blue arrows represent the drags exerted on the different parts of the surface. Momentum is transferred mainly by eddy diffusion. The total momentum flux,  $\tau$ , is split into  $\tau_r$  exerted on the roof of the elements,  $\tau_s$  exerted on the ground surface and  $\tau_c$  as a pressure drag on the elements.

The drag partition theory has been developed by many researcher, e.g. Arya (1975), Raupach (1992) and Shao and Yang (2005). In this study, we use the following results of Shao and Yang (2005),

$$\frac{\tau_c}{\tau} = \frac{\beta\lambda_e}{1 + \beta\lambda_e} \quad (5.15)$$

and

$$\lambda_e = \frac{\lambda}{(1-\eta)^{c_2}} \cdot \exp\left(-\frac{c_1\lambda}{(1-\eta)^{c_2}}\right) \quad (5.16)$$

with  $c_1=6$  and  $c_2=0.1$ .  $\lambda$  is the frontal area index and  $\eta$  is the basal area index of the elements.  $\beta$  is the ratio of the drag coefficient for isolated roughness element to that for bare surface.

### Dust flux partition

Dust transfer is closely related to momentum transfer. Similar to Eq. (5.14), the total

deposition flux can be split into three parts:

$$F_d = F_{d,c} + F_{d,s} + F_{d,r} \quad (5.17)$$

where  $F_{d,c}$  is the quantity of dust collected by the elements,  $F_{d,s}$  is that deposited on the ground surface and  $F_{d,r}$  on the roof of the elements.

Based on the definition of the elemental collection efficiency (refer to Section 2.1.4), the amount of dust collected by an isolated roughness element,  $q_{ci}$ , can be calculated as

$$q_{ci} = C \cdot u_a \cdot E \cdot d_c h_c \quad (5.18)$$

where  $C$  is dust concentration,  $u_a$  horizontal wind speed,  $E$  dust collection efficiency of an isolated element.

Per definition, the drag force exerted on an isolated element is:

$$f_{ci} = C_d \cdot \rho_a \cdot d_c h_c \cdot u_a^2 \quad (5.19)$$

where  $C_d$ , the drag coefficient for isolated roughness element, is approximately 0.3 (Shao, 2008), and  $\rho_a$  is air density. A combination of Eq. (5.18) and Eq. (5.19) yields

$$A_{qf} = \frac{q_{ci}}{f_{ci}} = \frac{E}{C_d} \cdot \frac{C}{\rho_a u_a} \quad (5.20)$$

Eq. (5.20) describes the relationship between the amount of dust collected by an element and the amount of momentum depleted by the element (drag on the element). The parameter  $A_{qf}$  is the ratio of ability of the element to collect dust and to absorb momentum.

For a rough surface with  $\tau_c$  exerted on the roughness elements, the quantity of dust collected by the roughness elements can be reasonably expected to be

$$F_{d,c} = \tau_c \cdot A_{qf} = \frac{\tau_c}{\tau} \cdot \frac{\tau}{\rho_a u_a} \cdot \frac{E}{C_d} \cdot C \quad (5.21)$$

The term  $\tau_c/\tau$  in Eq. (5.21) can be evaluated by Eq. (5.15). The element dust collection efficiency,  $E$ , consists of the contributions of Brownian motion, impaction and interception,  $E^B$ ,  $E^{im}$  and  $E^{in}$ , i.e.,

$$E = E^B + E^{im} + E^{in} \quad (5.22)$$

where  $E^B$  could be evaluated by Eq. (2.29) and  $E^{im}$  evaluated by Eq. (2.34). However, the knowledge of interception is still lacking. In this study, the following expression, modified from Eq. (2.36), is used

$$E^{in} = A_{in} \cdot u_* \cdot 10^{-St} \cdot \frac{2D_{p,\delta}}{d_c} \quad (5.23)$$

According to the definition, interception describes the behaviors of particles which can follow the flow well. The term  $10^{-St}$  is introduced to satisfy this requirement, as it approaches 1 for very small particles. As shown by the experimental data, the interception collection efficiency is enhanced by friction velocity. To consider the effect of micro-roughness characteristics (e.g. hair on roughness element), the term  $A_{in}u_*$  is introduced, with  $A_{in}$  being an empirical parameter related to the micro-roughness characteristics of the element surface, e.g., the ratio of hair size to element size and hair distribution.

Both the element roof and the ground surface can be considered to be smooth, on which dust deposition is caused by the mechanisms of gravitational settling, Brownian diffusion and impaction:

$$F_{d,r} = F_{d,r}^g + F_{d,r}^B + F_{d,r}^{im} \quad (5.24a)$$

$$F_{d,s} = F_{d,s}^g + F_{d,s}^B + F_{d,s}^{im} \quad (5.24a)$$

where  $F_{d,r}^g$  and  $F_{d,s}^g$  are caused by gravitational settling,  $F_{d,r}^B$  and  $F_{d,s}^B$  by Brownian diffusion and  $F_{d,r}^{im}$  and  $F_{d,s}^{im}$  by impaction.

The amount of dust deposited by gravitational settling can be calculated as

$$F_{d,r}^g = w_{t,\delta} \cdot C \cdot \eta \quad (5.25a)$$

$$F_{d,s}^g = w_{t,\delta} \cdot C \cdot (1 - \eta) \quad (5.25b)$$

Taking account of the possible particle growth, the terminal velocity near the surface,

$$w_{t,\delta} = w_t(D_{p,w}) \quad (5.26)$$

can be calculated using Eq. (2.8) but particle size  $D_{p,w}$  which can be estimated following Fitzgerald (1975) or Gerber (1985).

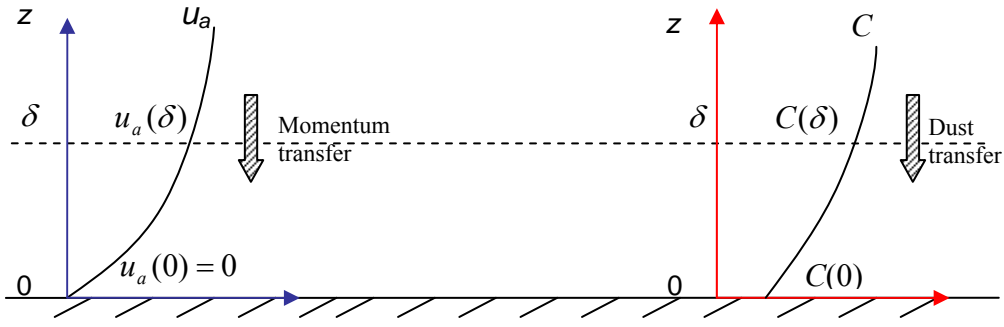


Figure 5-4: An illustration of Brownian diffusion on smooth surface.

Brownian diffusion is mainly responsible for dust to move across the laminar layer. The process of dust transfer is similar to that of momentum transfer (Figure 5-4). Dust particles, for which Brownian diffusion is effective, usually do not rebound from the surface (Chamberlain, 1966). For these particles, the surface dust concentration,  $C(0)$ , can be assumed to be zero. We therefore have

$$F_{d,r}^B = k_p \cdot \frac{C}{\delta} \cdot \eta \quad (5.27a)$$

$$\tau_c = \nu \cdot \frac{\rho u_a}{\delta} \cdot \eta \quad (5.27b)$$

A combination of (5.27a) and (5.27b) leads to

$$F_{d,r}^B = \frac{\tau_r}{\rho_a u_a} \cdot Sc^{-1} \cdot C \quad (5.28)$$

As shown in Figure 5-3, the shear stress exerted on the ground surface is

$$\tau_s = \tau - \tau_c - \tau_r \quad (5.29)$$

The pressure drag term,  $-\tau_c$ , leads to a momentum reduction of the mean flow by production of turbulence, and the enhanced turbulence has a positive contribution to the Brownian diffusion over the ground surface. Further, we neglect the difference in concentration between the element height and the top of laminar layer. In analogy to Eq. (5.27a), the deposition flux caused by Brownian diffusion to the ground surface is

$$F_{d,s}^B = \frac{\tau - \tau_r + \tau_c}{\rho_a \cdot u_a} \cdot Sc^{-1} \cdot C \quad (5.30)$$

Dust is also collected by the surfaces due to turbulent impaction. Studies show that turbulent impaction is depended on turbulence near the surface and the dimensionless particle relaxation time. Following SS80, dust deposition due to impaction on a upward facing surface can be expressed as

$$F_{d,r}^{im} + F_{d,s}^{im} = \frac{\tau}{\rho_a \cdot u_a(h)} \cdot 10^{\frac{3}{\tau_p^+}} \cdot C(h) \quad (5.31)$$

It follows from Eq. (5.17)- Eq. (5.31) that

$$F_d = \left\{ \frac{\tau}{\rho_a \cdot u_a(h)} \left[ \frac{E}{C_d} \cdot \frac{\tau_c}{\tau} + \left( 1 + \frac{\tau_c}{\tau} \right) \cdot Sc^{-1} + 10^{\frac{3}{\tau_p^+}} \right] + w_{t,s} \right\} C(h)$$

According to Eq. (5.5) and taking account of the rebound effect, the surface resistance is found to be

$$r_s = \left\{ R \cdot w_{dm} \left[ \frac{E}{C_d} \cdot \frac{\tau_c}{\tau} + \left( 1 + \frac{\tau_c}{\tau} \right) \cdot Sc^{-1} + 10^{\frac{3}{\tau_p^+}} \right] + w_{t,s} \right\}^{-1} \quad (5.32)$$

where  $R$  is the correction factor of rebound (S82), and

$$w_{dm} = \frac{\tau}{\rho_a \cdot u_a(h)}$$

is the conductance for momentum. For smooth surfaces,  $w_{dm}$  is given by

$$w_{dm} = B_2 \cdot u_*$$

where  $B_2$  is an empirical constant of 3 (Zhang et al., 2001).

To sum up, the parameters used in the new scheme are organized and shown in Table 5-1. Some terms, such as  $D_{p,w}$ ,  $\tau_c/\tau$ ,  $R$  and  $E$ , are evaluated by using existing works and are not shown in the Table.



Table 5-1: Summary of the improved dust deposition scheme. Input parameters are shown in the third row.

Parameterization								
Wind field			Surface				Particle	
$u_*$	$z_0$	$z_d$	$h_c$	$d_c$	$\lambda$	$A_m$	$b$	$D_p$ $\rho_p$
Rough surface			$w_{dm} = \frac{u_*^2}{u_a(h_c)}$	$\frac{\tau_c}{\tau} = f(n, \lambda, \eta)$	$E = E^B + E^{im} + E^{in}$	$D_{p,w}$	$R$	$r_g = \frac{18\mu}{C_c \rho_p D_p^2 g}$
$r_a(z) = \frac{1}{Sc_T \cdot k \cdot u_*} \ln\left(\frac{z - z_d}{h_c - z_d}\right)$								
Smooth surface			$w_{dm} = B_2 \cdot u_*$	Drag partition	Element collection	Particle growth	Rebound	Settling resistance
$r_a(z) = \frac{B_1}{Sc_T \cdot k \cdot u_*} \cdot \ln\left(\frac{z}{z_0}\right)$ $B_1 = 0.45$								
			$r_s = \left\{ R \cdot w_{dm} \left[ \frac{E}{C_d} \cdot \frac{\tau_c}{\tau} + \left(1 + \frac{\tau_c}{\tau}\right) \cdot Sc^{-1} + 10 \frac{3}{\tau_p} \right] + w_{t,\delta} \right\}^{-1}$					
			$w_d(z) = \left( r_g + \frac{r_s - r_g}{\exp(r_a / r_g)} \right)^{-1}$					

## 5.2 Scheme validation

Dust deposition is determined both by dust transport in the transfer layer and dust collection in the collection layer. In the absence of roughness elements, dust collection is achieved through turbulent impaction, Brownian motion and gravitational settling. Particle rebound does not occur for the sticky surface. Because gravitational settling in this study is calculated from particle size and the PDPA can only identify particles bigger than 0.5  $\mu\text{m}$ , which are too large for Brownian motion, the experimental data for the wood surface can only be used to evaluate the parameterization of turbulent diffusion and impaction. Figure 5-5 shows that the predictions of the new scheme for the wood surface agree with the experimental data well and better than the SS80 scheme.

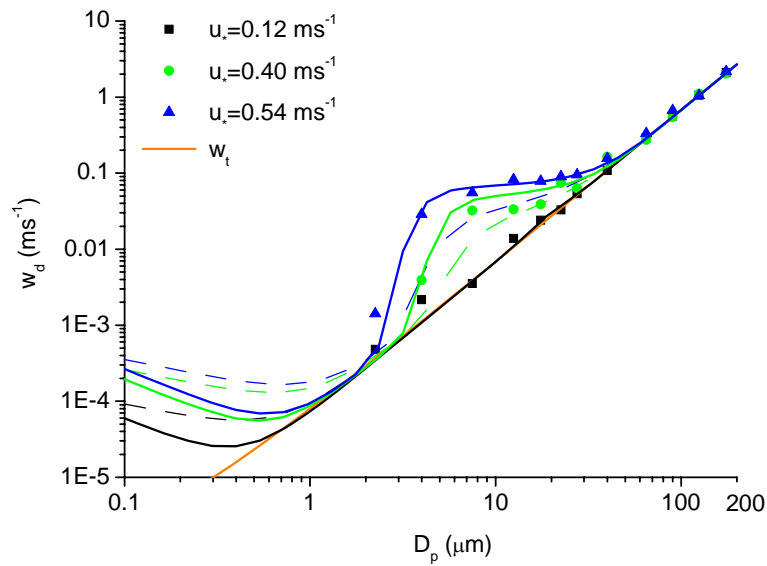


Figure 5-5: Comparison of deposition velocity,  $w_d$ , as function of particle diameter,  $D_p$ , predicted by the new scheme (solid lines) and the SS80 scheme (dashed lines) with the wind-tunnel measurements (symbols) for the sticky and smooth wood surface for three different wind conditions.

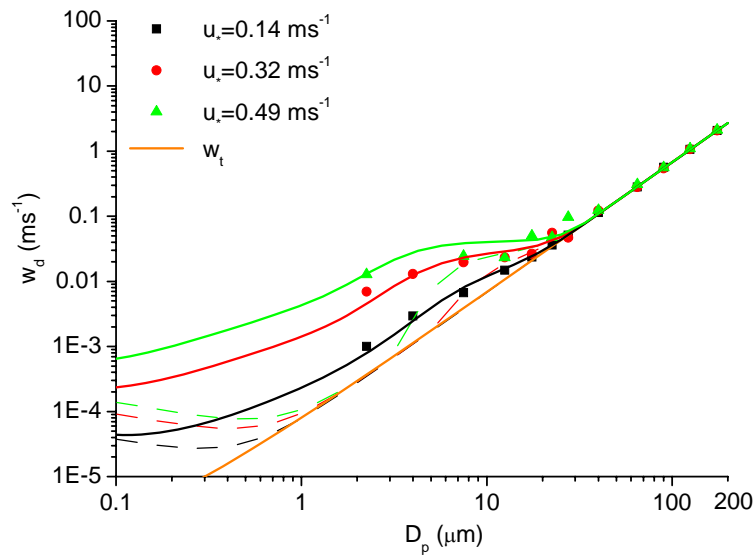


Figure 5-6: As Figure 5-5, but is for the sand surface. The parameters used in the new scheme include  $d_c = D_{sand}$  (average diameter of sand particles),  $h_c = d_c/2$ ,  $\lambda = 0.125$ ,  $b = 1$  and  $A_m = 1$ . The wind field parameters are selected according to Figure 4-12a.

The difference between the rough and smooth surfaces is that the elements

exposed on the rough surface not only enhance turbulence in the transfer layer but also improve the surface collection efficiency. Sand surface is a rough surface although the sizes of the roughness elements are small. The sand surface is used here as the second case to test the new scheme (Figure 5-6). The size of the elements is taken as the average diameter of the sand particles and element height half that diameter. The sand particles are assumed to be distributed uniformly on the surface and the distance between them is assumed to be twice the diameter. The other surface parameters, such as the frontal area and basal area indices can be calculated according to these assumptions. The rebound effect is taken into account and the  $b$  parameter is set to 1. As sand grains are smooth (no hair),  $A_{in}$  in Eq. (5.23) is set to 1.

Again, the predictions of the new scheme agree well with the experimental data. Compared with the SS80 scheme, the new scheme is obviously an improvement, especially for the particle size range from 2 to 10  $\mu\text{m}$ . The enhancement of deposition velocity can be attributed to better treatment of interception in the new scheme, which is neglected in the SS80 scheme. The results show that even small roughness elements on a surface can play an important role in the process of dust deposition.

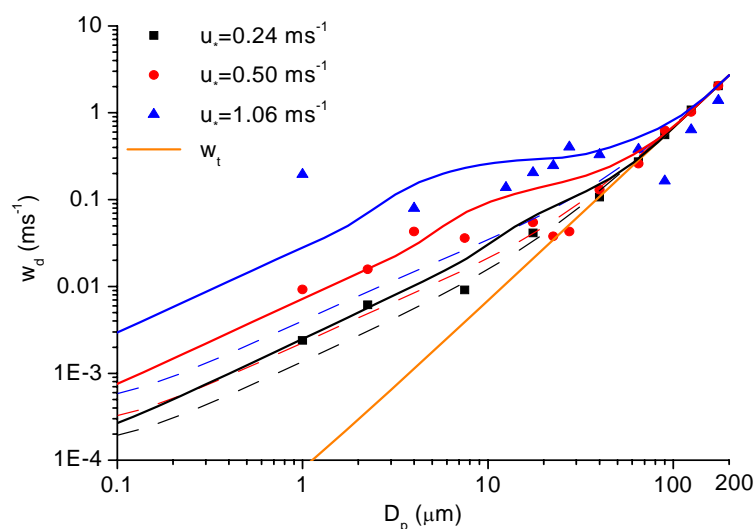


Figure 5-7: As Figure 5-5, but is for the tree surface. The solid lines are predictions of the new model and the dashed lines correspond to S82. The parameters used for the new scheme are  $d_c = 5$  mm,  $h_c = 230$  mm,  $\lambda = 0.4$ ,  $b = 0.01$  and  $A_{in} = 150$ . The parameters for the wind field are selected according to Figure 4-17.

The third case tested is the tree surface with rather complex structures. The roughness element (tree) size is  $d_c = 5$  mm and the height  $h_c = 230$  mm. Taking account of the effect of leaves, we set  $A_m = 150$  and  $\lambda = 0.4$ . The results of the new scheme shown in Figure 5-7 agree well with the experimental data and are better than the results of the S82 scheme.

We also tested the new scheme for the water surface. As shown in Figure 5-8, taking account of particle growth due to high humidity, the predicted deposition velocity with both the new and the SS80 scheme agrees with the experimental data. But the good agreement may be for the wrong reason: the Silicon Dioxide particles used in the experiments are not hygroscopic, to which the particle growth theory (Fitzgerald, 1975) does not apply. On the other hand, waves are visible on the water surface (Figure 4-4b). It is thus unreasonable to consider the water surface as a smooth surface.

The new scheme allows however to better describe the deposition of hydrophobic dust on the water surface. The water surface is treated as a rough surface, because under wind conditions, waves develop and bubbles or spray droplets are emitted from the surface. These waves, bubbles and droplets act as roughness elements. The input parameters used in the new scheme are taken as  $h_c = 30z_0$ ,  $d_c = 0.1$  mm and the distance between the adjacent elements is supposed to be equal to  $h_c$ . The other surface parameters, including element density and frontal area index, can be computed from these parameters. Taking account of bubbles or spray droplets, which behave like hair on the water surface, we set  $A_m = 100$ . Using the wind field parameters derived from the wind-tunnel experiments, the deposition velocities for different particle sizes are calculated. The results shown in Figure 5-9 confirm the good agreement between the scheme predictions with the experimental data. We have shown that the enhanced deposition over the water surface is indeed not due to particle growth, but to the enhanced collection capacities of the water surface caused by waves, bubbles and spray droplets.

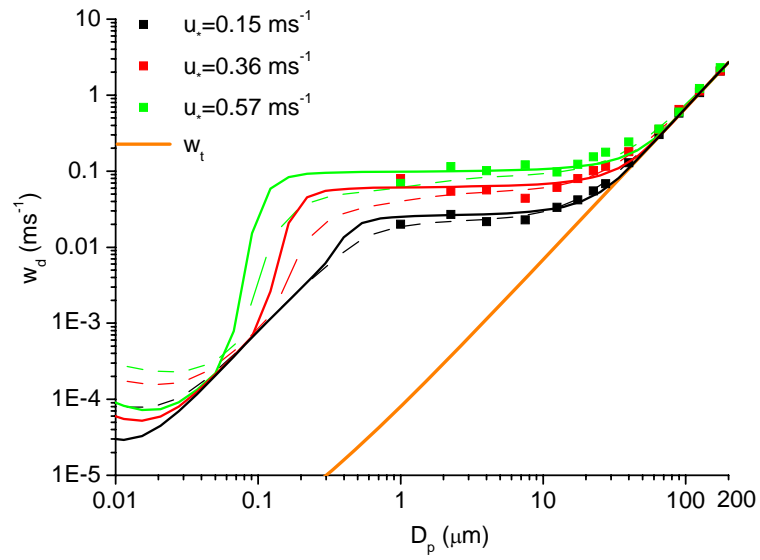


Figure 5-8: As Figure 5-5, but is for the water surface.

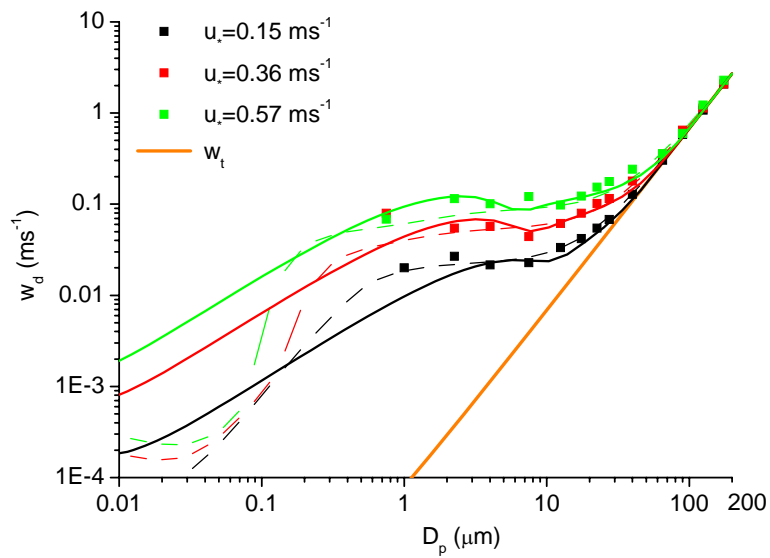


Figure 5-9: As Figure 5-5, but is for water surface. The surface is considered to be rough and the surface parameters are  $h_c = 30z_0$ ,  $d_c = 0.1$  mm,  $b = 0$ ,  $A_{in} = 100$  and the distance between the adjacent elements (waves) is equal to  $h_c$ . The wind field parameters are selected according to Figure 4-5.

The parameters used for the various surfaces discussed above are list in Table 5-2.

Table 5-2 Parameters used for the discussion of various surfaces

	$z_r$ (mm)	$u^*$ (m/s)	$z_0$ (mm)	$z_d$ (mm)	$h_c$ (mm)	$d_c$ (mm)	$\lambda$	$A_{in}$	$b$	$\rho_p$ ( $\text{kg}\cdot\text{m}^{-3}$ )
Sticky wood		0.12	0.075	0	0	0	0	1	0	2200
	15	0.40	0.033	0	0	0	0	1	0	2200
		0.54	0.032	0	0	0	0	1	0	2200
Sand		0.14	0.153	0	0.2	0.1	0.125	1	1	2200
	15	0.32	0.143	0	0.2	0.1	0.125	1	1	2200
		0.49	0.135	0	0.2	0.1	0.125	1	1	2200
Tree		0.24	5.927	200	230	5	0.4	150	0.01	2200
	250	0.50	2.877	200	230	5	0.4	150	0.01	2200
		1.06	2.106	200	230	5	0.4	150	0.01	2200
Water		0.15	0.300	0	$30z_0$	0.1	0.538	100	0	2200
	25	0.36	0.306	0	$30z_0$	0.1	0.538	100	0	2200
		0.57	0.309	0	$30z_0$	0.1	0.538	100	0	2200

### 5.3 Sensitivity analysis

The results shown in the previous section highlighted the good performance of the new scheme when compared with the experimental data. As the scheme performance depends on the certainty of the input parameters listed in Table 5-1, it is important to examine the scheme sensitivity to these parameters and to identify the most influential ones.

Table 5-1 shows that dust deposition depends on particle properties (size and density), aerodynamic conditions (friction velocity, roughness length and zero-plane displacement) and surface characteristics (roughness element size, density, frontal area index and rebound ability). In general, these parameters do not necessarily change independently. For example, while roughness length and zero-plane

displacement are used to describe wind profiles, they also reflect the characteristics of the surface. The variations in surface parameters, such as roughness element density and frontal area index, also cause changes in wind profiles.

First, we consider the sensitivity of dust deposition to particle properties. The typical behavior of deposition velocity as a function of particle size has been shown many times (e.g. Figure 5-5): it is large for small particles ( $< 0.01 \mu\text{m}$ ) because of Brownian diffusion and it is also large for big particles ( $> 50 \mu\text{m}$ ) because of gravitational settling. Dust deposition is suppressed for particles in the range from 0.01 to 50  $\mu\text{m}$ , because they are too big for Brownian diffusion and too small for gravitational settling. Normally, the minimum deposition velocity occurs in the range from 0.1 to 1  $\mu\text{m}$  (Figure 5-5 and 5-6), but the enhancement of interception shifts this range to smaller particles (Figure 5-7 and 5-9).

Particle density influences gravitational settling and the processes related to particle inertia, such as impaction. As shown in Figure 5-10, the variability of particle density mainly affects the deposition of coarse particles larger than 5  $\mu\text{m}$ , through the modification of gravitational settling.

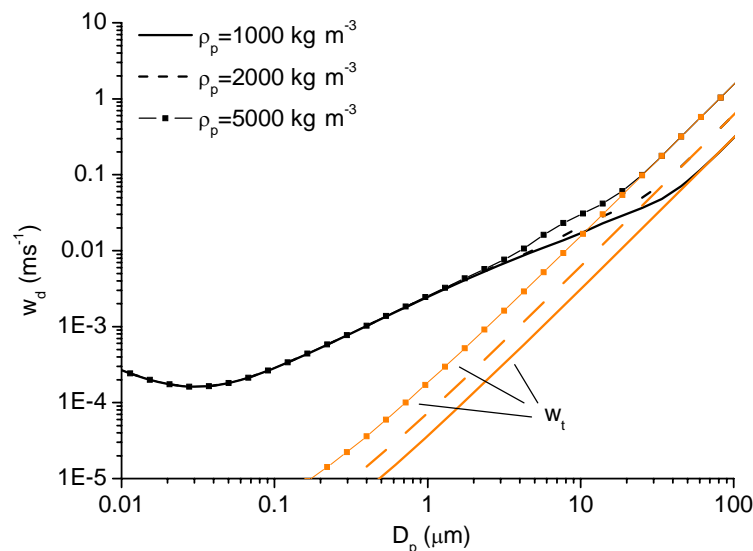


Figure 5-10: Sensitivity of deposition velocity to particle density. The deposition velocity is calculated for the reference height  $z_r = 100 z_0 + d$ . The aerodynamic and surface parameters are  $u_* = 0.3 \text{ m}\cdot\text{s}^{-1}$ ,  $z_0 = 10 \text{ mm}$ ,  $d = 100 \text{ mm}$ ,  $h_c = 150 \text{ mm}$ ,  $d_c = 5 \text{ mm}$ ,  $A_{in} = 100$  and  $b = 1$ .

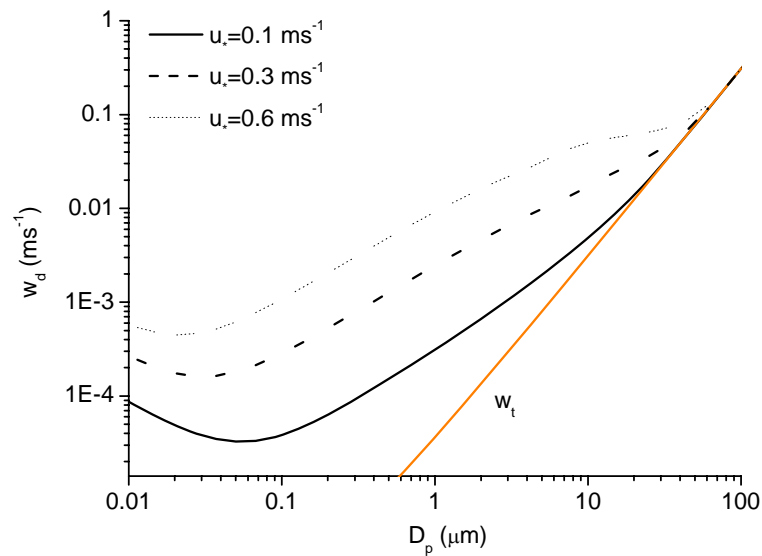


Figure 5-11: Sensitivity of deposition velocity to friction velocity. Dust density is  $\rho_p = 1000 \text{ kg}\cdot\text{m}^{-3}$ . The other parameters are the same as for Figure 5-10.

Secondly, we consider the aerodynamic parameters. Friction velocity is an aerodynamic parameter which influences the entire deposition process from turbulent diffusion to surface collection. As shown in Figure 5-11, the influence of friction velocity is predominantly for particles smaller than  $10 \mu\text{m}$ , for which the deposition is largely determined by turbulent transfer. An increased friction velocity improves surface collection due to impaction and interception and hence a noticeable enhancement of deposition for particles between  $0.1$  and  $10 \mu\text{m}$ .

Thirdly, we consider the sensitivity of deposition to surface characteristics. Roughness element size affects the element collection efficiency and two parameters are used to describe the element size in the new scheme. One is element diameter,  $d_c$ , and the other the micro-roughness parameter,  $A_{in}$ . Micro-roughness features, such as hair on the element, enhance the element collection efficiency due to interception (Chamberlain, 1976; S82). For smooth elements ( $A_{in} = 1$ ), the influence of  $d_c$  can be readily analyzed. To highlight the effect of impaction and interception, a large friction velocity ( $0.6 \text{ m}\cdot\text{s}^{-1}$ ) is selected here. As Figure 5-12 shows, element size mainly affects the deposition of particles in the size range of  $0.1$  to  $10 \mu\text{m}$ , because it determines the collection efficiency due to impaction and interception. For particles in the range of



0.1 to 5  $\mu\text{m}$ , deposition velocity is increased for small element size because of the improved interception. For particles from 5 to 50  $\mu\text{m}$ , impaction increases with element size and so does deposition velocity.

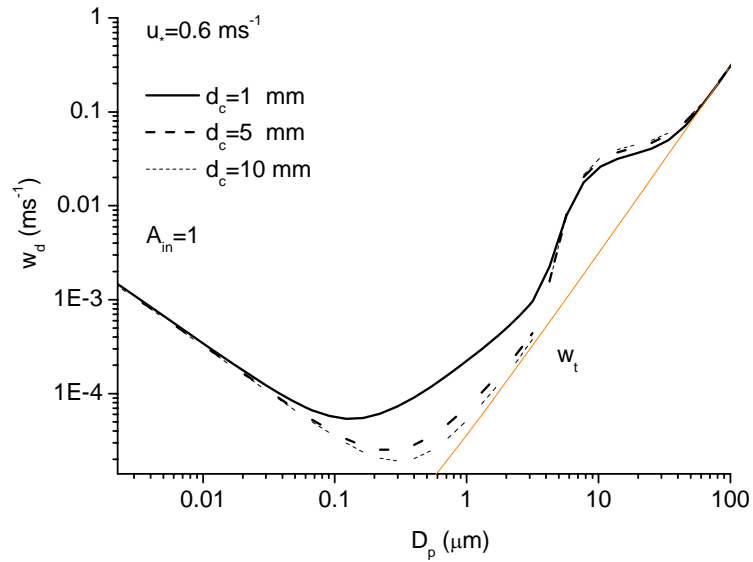


Figure 5-12: Sensitivity of deposition velocity to roughness element size. The friction velocity is  $u_* = 0.6 \text{ m}\cdot\text{s}^{-1}$ .  $A_{in} = 1$  and the other parameters are the same as for Figure 5-10.

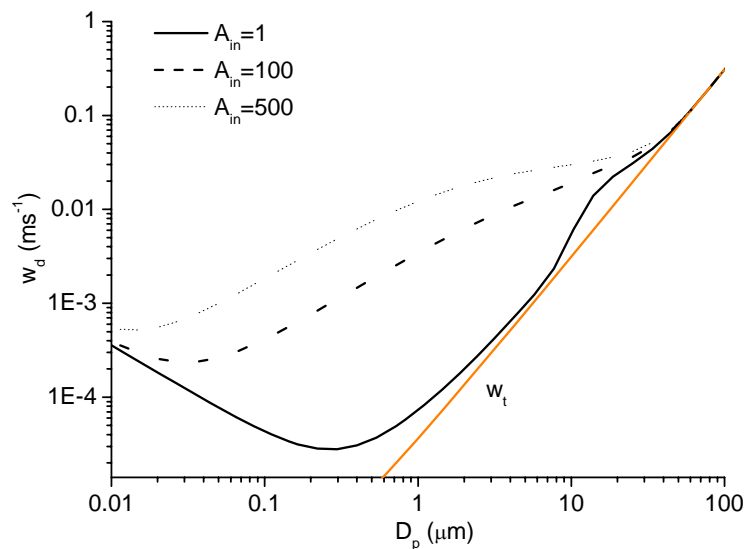


Figure 5-13: Sensitivity of deposition velocity to surface micro-roughness. The other parameters are the same as for Figure 5-10.

While  $d_c$  is usually too large to affect interception, the influence of  $A_{in}$  is significant and most profound on the deposition of particles in the size range of 0.1 to 10  $\mu\text{m}$  (Figure 5-13).

The parameter  $R$  describes the rebound probability when a particle collides with the surface. The influence of  $R$  on the deposition is visible for coarse particles larger than 5  $\mu\text{m}$  (Figure 5-14).

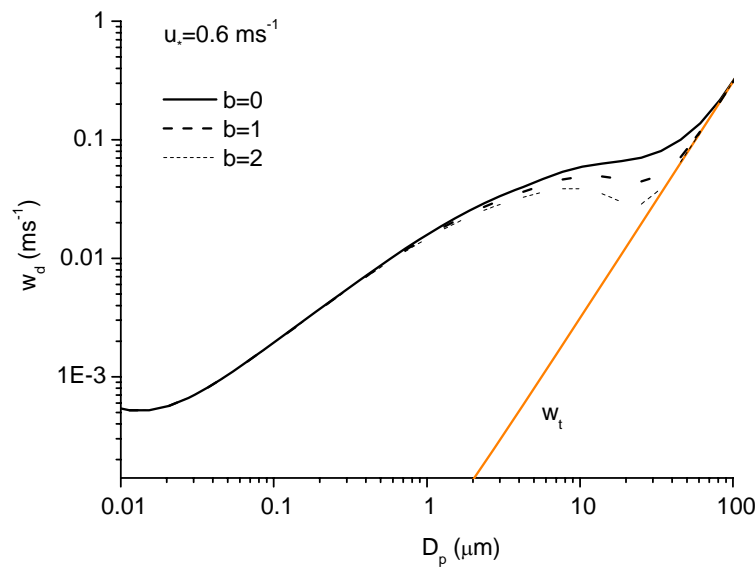


Figure 5-14. Sensitivity of deposition velocity to rebound probability. The friction velocity is set to  $u_* = 0.6 \text{ m}\cdot\text{s}^{-1}$ . The other parameters are the same as for Figure 5-10.

Roughness element frontal area index is a parameter used to describe the element distribution on the surface, used in the drag partition theory. We now test its influence on dust deposition in the absence of micro-roughness. As shown in Figure 5-15, deposition velocity first increases, then decreases with frontal area index. The influence affects all particle sizes, especially for particles in the range of 0.1 to 1  $\mu\text{m}$ . Figure 5-15 suggests that in case of small frontal area index, the elements make the surface rougher and enhance the surface collection, but as the number of elements further increases, the surface becomes again smoother and the surface collection efficiency is decreased. The influences of element frontal area index on surface resistance and deposition velocity for particles with diameter 1  $\mu\text{m}$  are shown in

Figure 5-16.

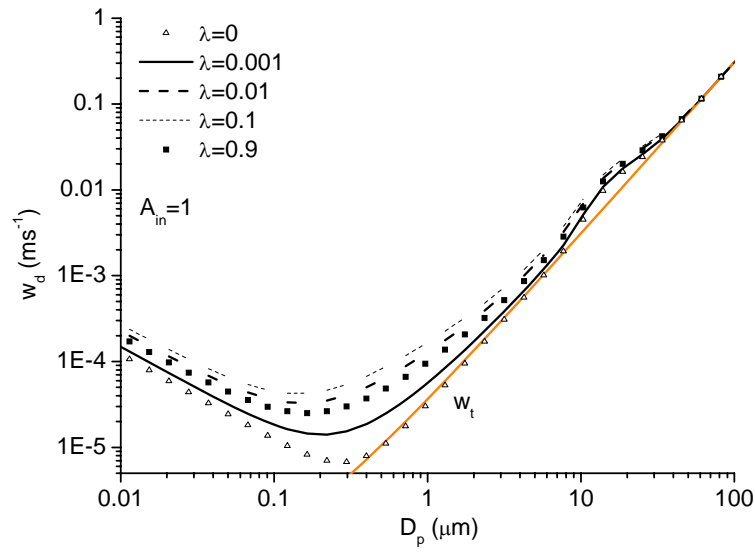


Figure 5-15: Sensitivity of deposition velocity to element frontal area index. We have set  $\rho_p = 2200 \text{ kg}\cdot\text{m}^{-3}$ ,  $A_{in} = 1$  and the other parameters as for Figure 5-10.

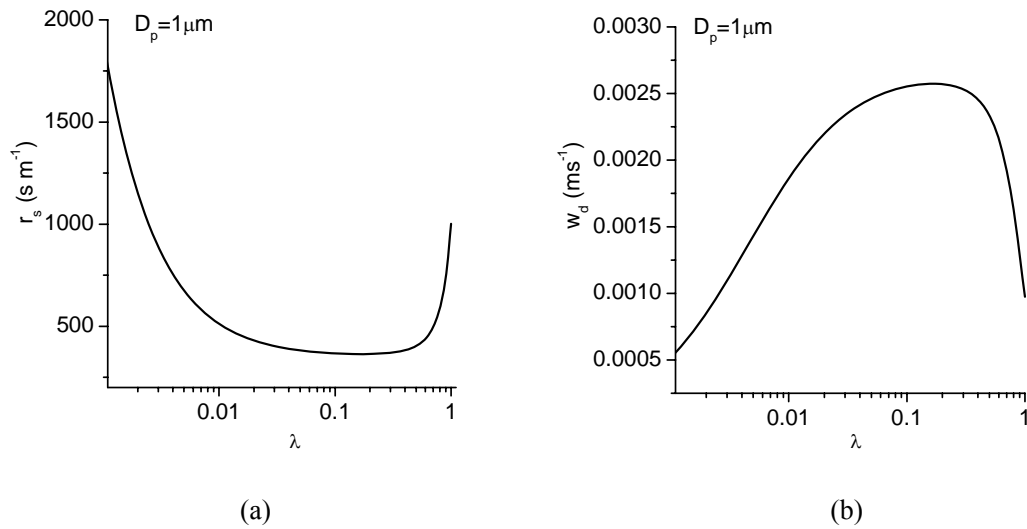


Figure 5-16: The influence of element frontal area index on (a) surface resistance and (b) deposition velocity for particles with diameter of  $1 \mu\text{m}$ . The other parameters are the same as for Figure 5-10.

## 5.4 Summary

A new dust deposition scheme is proposed by taking account of the impact of roughness elements on turbulent diffusion and surface collection. The relationship between the aerodynamics and surface collection process is established, and the effect of the interactions between the elements is introduced into the scheme in analogy to the drag partition theory. Besides, a modified expression for interception is proposed to account for the micro-roughness effect of the elements.

The new scheme is tested against the experimental data and good agreement between the scheme predictions and the observations is achieved. A new and more physical explanation based on the new scheme is proposed for the deposition of hydrophobic dust on water surface.

The sensitivity of the new scheme to some of the important input parameters has been tested. It is found that dust density and particle rebound probability mostly influence the deposition of coarse particles larger than 5  $\mu\text{m}$ ; the size and micro-roughness characteristics of the roughness elements influence interception noticeably and hence the deposition of particles in the size range of 0.1 to 10  $\mu\text{m}$ ; friction velocity affects the entire deposition process and influences the deposition of particles of all sizes; element frontal area index has a predominant effect on surface collection efficiency and influences the deposition of particles of all sizes.

## Chapter 6

# Summary and Outlook

In this dissertation, we have described a study on dust deposition, including wind-tunnel experiments and an improved parameterization of dust deposition. The conclusions of this research are summarized in this chapter and recommendations for future research are made.

## 6.1 Summary and conclusions

In Chapter 1, the topic of this study, namely dust deposition, is introduced together with a brief description of the background of the study. The aims of this study are as follows:

- to conduct wind-tunnel experiments to obtain a comprehensive and cohesive dataset for dust deposition;
- to validate existing dust deposition schemes using the experimental data; and
- to improve the dust deposition parameterization.

In Chapter 2, the basic theory of dust deposition is presented. The relevant concepts are introduced and the current knowledge of dust deposition mechanisms is summarized. The traditional experimental methods are described. The shortcomings of the measurement techniques and existing experimental data are summarized. It is found that there is a lack of information on previous experimental details and the measuring techniques have poor comparability. Also, the prevalent dust deposition schemes are shown in Chapter 2. The shortcomings of the existing schemes, such as the inadequate treatment of gravitational settling in the resistance scheme and the lack of suitable parameterization for surface collection processes are presented.

In Chapter 3, the facilities and equipments for the wind-tunnel experiments are described. The components, principles and specifications of the instruments as well as the design, purposes, configurations and procedures of execution are presented. The wind-tunnel experimental conditions are tested to measure the stability and profile of wind and dust concentration. It is shown that the wind-tunnel experimental conditions conform to those of a neutral atmosphere boundary layer and satisfy the requirements of our experiments.

In Chapter 4, the methodology of data processing is described. The deposition velocities for different particles are extracted from the experimental data and used to test the SS80 (for smooth surface) and S82 (for canopy) schemes. The following results are found:

- The measurements indicate that deposition velocity for the particle bigger than  $1\ \mu\text{m}$  increases with particle size and friction velocity. The elements on the surface can significantly enhance dust deposition, especially for dust smaller than  $4\ \mu\text{m}$ .
- Over water surface, the deposition velocities for the particles in the size range of 1 to  $12.5\ \mu\text{m}$  do not significantly differ from each other and their values increase almost linearly with friction velocity.
- Dust deposition on water surface can be well predicted by the SS80 (1980) scheme in which particle growth caused by humidity is considered. But the good scheme performance may be due to a wrong reason, because the particles ( $\text{SiO}_2$ ) used in our experiment is hydrophobic.
- Dust deposition on dry surface is underestimated by the SS80 and S82 schemes. On smooth surface, particles with diameter larger than  $4\ \mu\text{m}$  are effectively deposited by impaction which has been considered in the schemes but underestimated; on rough surface, the serious underestimation of the deposition velocity for particles in the size range of 1 to  $4\ \mu\text{m}$  may be caused by the underestimation of interception.
- The S82 scheme can predict the deposition velocity well by selecting a suitable value of small-collector size. But the characteristic dimension of the small collectors is difficult to estimate.

In Chapter 5, a new scheme with improved parameterization for the surface collection process is proposed. The relationship between the aerodynamics and surface collection process is established, and the effect of interaction between the elements is introduced to the parameterization scheme in analogy to the drag partition theory. A sensitivity analysis is carried out. The results are

- Dust density and particle rebound probability mostly influence the deposition of coarse particles larger than 5  $\mu\text{m}$ ;
- The size and micro-roughness characteristics of the roughness elements influence interception noticeably and hence the deposition of particles in the size range of 0.1 to 10  $\mu\text{m}$ ;
- Friction velocity effects the entire deposition process and influences the deposition of particles of all sizes;
- Element frontal area index has a predominant effect on surface collection efficiency and influences the deposition of particles of all sizes.

In conclusion, a series of wind-tunnel experiments have been successfully carried using the most sophisticated instrument available to date to produce a reliable and comprehensive dataset. We have used the experimental data to test the most representative existing dust deposition schemes. By analyzing the differences between the predictions and experimental data, the shortcomings of the existing schemes have been identified. This has allowed us to propose a new dust deposition scheme by incorporating the drag partition theory. Comparison with the data has demonstrated the new scheme performs better than the existing schemes.

## 6.2 Outlook

Through the theoretical work and the wind-tunnel experiments presented in this study, our understanding on dust deposition is improved, and with the development of the new scheme, our capacity for dust deposition parameterization improved. However, some questions remain unanswered and we recommend that future research should focus on the following issues:

### **The effect of wind intermittency**

In our study, we assumed the wind is steady and the effect of wind intermittency is

neglected. But wind intermittency probably seriously affect the dust deposition, including dust transport in the upper layer and dust collection in the lower layer (Figure 5-1). While some studies on the topic already exist, e.g., the treatment of the effect of wind intermittency on aerodynamic resistance by Zhang et al. (2001) and Seinfeld and Pandis (2012), the influence of wind intermittency on the dust collection process deserves further research.

### **Deposition on complex surfaces**

Only surfaces with relatively simple and uniform elements are tested in our study, but natural surfaces are much more complex. For example, how to predict dust deposition to surfaces with multi-size elements is important for regional and global dust models.

### **Effect of element-interaction on element collection efficiency**

In analogy to the drag partition theory, an expression for describing the distribution of total deposited dust on different parts of the surface (elements or up-facing surface) is proposed in our study. But the element collection efficiency is evaluated based on the study of isolated elements. The effect on element collection efficiency due to the interactions between the roughness elements remains rather unclear.

### **Mutual promotion between deposition scheme and drag partition theory**

In our work, a relationship between dust deposition and drag partition is proposed. An opportunity of mutual promotion exists between the studies on dust deposition and drag partition. The drag partition theory could improve the quality of deposition scheme. The deposited dust can be treated as a 'tracer element'. By measuring the quantity of dust deposited on different part of the surface could improve our understanding of drag partition.



## List of Symbols

$A_{in}$	Empirical parameter for surface micro-roughness characteristics	/
$A_{gf}$	Ratio of ability of the element to collect dust and to absorb momentum	/
$a$	Numerical constant in surface collection efficiency due to Brownian motion	/
$B_1, B_2$	Empirical constant	/
$b$	Numerical constant in rebound expression	/
$C$	Dust concentration	$\text{kg}\cdot\text{m}^{-3}$
$C_c$	Cunningham correction factor	/
$C_d$	Drag coefficient for obstacle	/
$c$	Fraction of the total collected momentum collected by small collectors (e.g. vegetative hairs)	/
$c_d$	$c_d$ is average drag coefficient for vegetation	/
$c_v$	The portion of $c_d$ arising from viscous drag (as opposed to form drag),	/
$D_a$	The effective diameter of air molecule	m
$D_p, D_{aw}$	Dry/wet particle diameter	m
$d_c, d_c^l, d_c^s$	Dimension of the roughness elements, large collector (i.e. roughness elements) and small collector	m
$E, E^B, E^{in}, E^{im}$	Element collection efficiency for different mechanisms	/
$F_d, F_d^{mean}, F_d^{diff}, F_d^g, F_d^B, F_d^T$	Dust deposition flux caused by different mechanisms	$\text{Kg}\cdot\text{m}^{-2}\cdot\text{s}^{-1}$

$F_s, F_s^g, F_s^B, F_s^{im}, F_s^{in}$	Flux of dust collected by surface due to different mechanisms	$\text{Kg}\cdot\text{m}^{-2}\cdot\text{s}^{-1}$
$f_r$	Aerodynamic drag	N
$G$	Gravity	N
$G_{im}, G_B$	Impaction and Brownian diffusion conductance	$\text{m}\cdot\text{s}^{-1}$
$G_{aM}$	Aerodynamic conductance for momentum	$\text{m}\cdot\text{s}^{-1}$
$g$	Gravitational acceleration	$\text{m}\cdot\text{s}^{-2}$
$h$	Thickness of surface layer	m
$h_c$	Height of roughness element	m
$K_B$	Boltzmann constant	$\text{J}\cdot\text{K}^{-1}$
$K_p$	Particle eddy diffusivity	$\text{m}^2\cdot\text{s}^{-1}$
$K_T$	Turbulent (or eddy) viscosity	$\text{m}^2\cdot\text{s}^{-1}$
$k_p$	Brownian diffusion coefficient	$\text{m}^2\cdot\text{s}^{-1}$
$k$	von Karman constant	/
$n$	Element density	$\text{m}^{-2}$
$R$	Reduction in collection caused by rebound	/
$Re$	Reynolds number	/
$r_a, r_b, r_c$	Aerodynamic, laminar (or quasi-laminar) layer, and surface resistance	$\text{s}\cdot\text{m}^{-1}$
$r_s$	Surface collection resistance including the effect of both $r_b$ and $r_c$	$\text{s}\cdot\text{m}^{-1}$
$r_g$	Resistance of gravity (inverse of terminal velocity)	$\text{s}\cdot\text{m}^{-1}$
$Sc$	Schmidt number	/
$Sc_T$	Turbulent Schmidt number	/
$St$	Stokes number	/

$u_a$	Horizontal velocity of air	$\text{m}\cdot\text{s}^{-1}$
$u_*$	Friction velocity	$\text{m}\cdot\text{s}^{-1}$
$V$	Volume of the sampling area	$\text{m}^3$
$V_p$	Resultant velocity of particle	$\text{m}\cdot\text{s}^{-1}$
$w_a, w_p, w_r$	Vertical velocity for air, particle and particle-to-air	$\text{m}\cdot\text{s}^{-1}$
$w_d$	Deposition velocity	$\text{m}\cdot\text{s}^{-1}$
$w_t$	Terminal velocity	$\text{m}\cdot\text{s}^{-1}$
$z, z_r$	Height and reference height	$\text{m}$
$z_0, z_d$	Roughness length and zero-plane displacement	$\text{m}$
 <b><i>Greek symbols</i></b>		
$\gamma$	A parameter characterizing the wind profile in canopy	/
$\delta, \delta'$	Thickness of laminar layer or quasi-laminar layer	$\text{m}$
$\delta_f$	Distance between the brightness and darkness fringes	$\text{m}$
$\eta$	Basal area index	/
$\theta$	The angle between the incident beams of PDPA	degree
$\lambda$	Frontal area index	/
$\lambda_m$	Mean free path of molecular motion ( $\sim 3.5 \times 10^{-10}\text{m}$ )	$\text{m}$
$\lambda_l$	Wavelength of laser	$\text{m}$
$\mu$	Dynamic viscosity of air	$\text{kg}\cdot\text{m}^{-1}\cdot\text{s}^{-1}$
$\nu$	Kinematic viscosity of air	$\text{m}^2\cdot\text{s}^{-1}$
$\xi, \xi^B, \xi^{im}, \xi^{in}$	Surface collection efficiency for different mechanisms	/
$\rho_p, \rho_a$	Particle/air density	$\text{kg}\cdot\text{m}^{-3}$
$\tau, \tau_c, \tau_s, \tau_r$	Drag exerted on different parts of the surface	$\text{N}\cdot\text{m}^{-2}$
$\tau_p$	Relaxation time of particle	$\text{s}$

---

$\tau_p^+$	Dimensionless particle relaxation time	/
$\phi$	Phase difference for Doppler signals	/
$\varphi$	Geometrical factor of PDPA	/

# Bibliography

- Arya, S. P. S. (1975). A drag partition theory for determining the large-scale roughness parameter and wind stress on the Arctic pack ice. *Journal of Geophysical Research*, 80(24), 3447-3454.
- Bache, D. H. (1979a). Particle transport within plant canopies—I. A framework for analysis. *Atmospheric Environment*, 13(9), 1257-1262.
- Bache, D. H. (1979b). Particulate transport within plant canopies—II. Prediction of deposition velocities. *Atmospheric Environment*, 13(12), 1681-1687.
- Beswick, K. M., Hargreaves, K. J., Gallagher, M. W., Choularton, T. W., & Fowler, D. (1991). Size-resolved measurements of cloud droplet deposition velocity to a forest canopy using an eddy correlation technique. *Quarterly Journal of the Royal Meteorological Society*, 117(499), 623-645.
- Bleyl, M. (2001). Experimentelle Bestimmung der Depositionsgeschwindigkeit Luftgetragener Partikel mit Hilfe der Eddy-Kovarianzmethode über einem Fichtenaltbestand im Solling. *Ph.D. Thesis*, Georg-August-Universität, Göttingen.
- Businger, J. A. (1986). Evaluation of the accuracy with which dry deposition can be measured with current micrometeorological techniques. *Journal of Climate and Applied Meteorology*, 25, 1100-1124.
- Buzorius, G., Rannik, Ü., Mäkelä, J. M., Vesala, T., & Kulmala, M. (1998). Vertical aerosol particle fluxes measured by eddy covariance technique using condensational particle counter. *Journal of Aerosol Science*, 29(1), 157-171.
- Campbell Scientific, Inc. (2007). CSAT3 Three Dimensional Sonic Anemometer. Revision 2/07.
- Cellier, P., & Brunet, Y. (1992). Flux-gradient relationships above tall plant canopies. *Agricultural and Forest Meteorology*, 58(1), 93-117.
- Chamberlain, A. C. (1966). Transport of gases to and from grass and grass-like surfaces. Proceedings of the Royal Society of London. Series A. *Mathematical and Physical Sciences*, 290(1421), 236-265.
- Chamberlain, A. C. (1967). Transport of Lycopodium spores and other small particles to rough surfaces. Proceedings of the Royal Society of London. Series A. *Mathematical and Physical Sciences*, 296(1444), 45-70.
- Clough, W. S. (1973). Transport of particles to surfaces. *Journal of Aerosol Science*, 4(3), 227-234.
- Clough, W. S. (1975). The deposition of particles on moss and grass surfaces. *Atmospheric Environment*, 9(12), 1113-1119.
- Csanady, G. T. (1963). Turbulent diffusion of heavy particles in the atmosphere. *Journal of Atmospheric Sciences*, 20, 201-208.
- Dantec Dynamics A/S (2006). BSA Flow Software Installation & User's Guide, Version 4.10.
- Davidson, C. I., & Wu, Y. L. (1990). Dry deposition of particles and vapors. *Acidic precipitation* (pp. 103-216). Springer New York.
- Droppo, J. G. (2006). Improved Formulations for Air-Surface Exchanges Related to National Security Needs: Dry Deposition Models. Pacific Northwest National Laboratory.

- Durst, F. & Zaré, M. (1976). Laser Doppler measurements in two-phase flows. *In The accuracy of flow measurements by laser Doppler methods*, Vol. 1, pp. 403-429.
- Fick A., (1855), Über Diffusion. *Poggendorff's Annalen der Physik und Chemie*, 94, 59-86.
- Fitzgerald, J. W. (1975). Approximation Formulas for the Equilibrium Size of an Aerosol Particle as a Function of Its Dry Size and Composition and the Ambient Relative Humidity. *Journal of Applied Meteorology*, 14, 1044-1049.
- Fuchs, N. A. (1964). *Mechanics of Aerosols*. Pergamon, New York.
- Gallagher, M. W., Choularton, T. W., Morse, A. P. & Fowler, D. (1988). Measurements of the size dependence of cloud droplet deposition at a hill site. *Quarterly Journal of the Royal Meteorological Society*, 114(483), 1291-1303.
- Gallagher, M. W., Beswick, K. M., Duyzer, J., Westrate, H., Choularton, T. W., & Hummelshøj, P. (1997). Measurements of aerosol fluxes to speulder forest using a micrometeorological technique. *Atmospheric Environment*, 31(3), 359-373.
- Garland, J. A. (2001). On the size dependence of particle deposition. *Water, Air and Soil Pollution: Focus*, 1(5-6), 323-332.
- Gerber, H. E. (1985). Relative-humidity parameterization of the Navy Aerosol Model (NAM) (No. NRL-8956). Naval Research Lab, Washington DC.
- Gieré, R. & Querol, X. (2010). Solid particulate matter in the atmosphere. *Elements*, 6(4), 215-222.
- Ginoux, P., Prospero, J. M., Torres, O., & Chin, M. (2004). Long-term simulation of global dust distribution with the GOCART model: correlation with North Atlantic Oscillation. *Environmental Modelling & Software*, 19(2), 113-128.
- Giorgi, F. (1988). Dry deposition velocities of atmospheric aerosols as inferred by applying a particle dry deposition parameterization to a general circulation model. *Tellus B*, 40(1), 23-41.
- Goossens, D. & Offer, Z. Y. (1994). An evaluation of the efficiency of some eolian dust collectors. *Soil technology*, 7(1), 25-35.
- Goossens, D. & Rajot, J. L. (2008). Techniques to measure the dry aeolian deposition of dust in arid and semi-arid landscapes: a comparative study in West Niger. *Earth Surface Processes and Landforms*, 33(2), 178-195.
- Gregory, P. H. & Stedman, O. J. (1953). Deposition of airborne Lycopodium spores on plane surfaces. *Annals of Applied Biology*, 40, 651-674.
- Grimm Aerosol Technik GmbH & Co. KG. (2010). Portable Laser Aerosol spectrometer and Dust Monitor Model 1.108/1.109.
- Grönholm, T., Aalto P. P., Hiltunen V., et al. (2007). Measurements of aerosol particle dry deposition velocity using the relaxed eddy accumulation technique. *Tellus B*, 59(3), 381-386.
- Hinds, W. C. (2012). *Aerosol technology: properties, behavior, and measurement of airborne particles*. Wiley-interscience.
- Hicks, B. B., Wesely, M. L., Durham, J. L., & Brown, M. A. (1982). Some direct measurements of atmospheric sulfur fluxes over a pine plantation. *Atmospheric Environment* (1967), 16(12), 2899-2903.
- Hicks, B. B., Baldocchi, D. D., Meyers, T. P., Hosker Jr, R. P., & Matt, D. R. (1987). A preliminary multiple resistance routine for deriving dry deposition velocities from measured quantities. *Water, Air, and Soil Pollution*, 36(3-4), 311-330.
- Hicks, B. B., Matt, D. R., et al. (1989). A field investigation of sulfate fluxes to a deciduous forest. *Journal of Geophysical Research: Atmospheres* (1984–2012), 94(D10), 13003-13011.
- IPCC. *Climate Change 2007: IPCC Fourth Assessment Report (AR4)*. Cambridge University Press: 2007.

- Lamaud, E., Chapuis, A., Fontan, J., & Serie, E. (1994). Measurements and parameterization of aerosol dry deposition in a semi-arid area. *Atmospheric Environment*, 28(15), 2461-2471.
- Little, P. (1977). Deposition of 2.75, 5.0 and 8.5  $\mu\text{m}$  particles to plant and soil surfaces. *Environmental Pollution* (1970), 12(4), 293-305.
- Liu, B. Y. & Agarwal, J. K. (1974). Experimental observation of aerosol deposition in turbulent flow. *Journal of Aerosol Science*, 5(2), 145-155.
- Malm, W. C., Day, D. E., Kreidenweis, S. M., Collett, J. L., & Lee, T. (2003). Humidity-dependent optical properties of fine particles during the Big Bend Regional Aerosol and Visibility Observational Study. *Journal of Geophysical Research*, 108(D9), 4279.
- McMahon, T. A., & Denison, P. J. (1979). Empirical atmospheric deposition parameters—a survey. *Atmospheric Environment*, 13(5), 571-585.
- Mili, H. R., & Lempfert, R. G. K. (1904). The great dust-fall of February 1903, and its origin. *Quarterly Journal of the Royal Meteorological Society*, 30(129), 57-91.
- Nemitz, E., Gallagher, M. W., Duyzer, J. H., & Fowler, D. (2002). Micrometeorological measurements of particle deposition velocities to moorland vegetation. *Quarterly Journal of the Royal Meteorological Society*, 128(585), 2281-2300.
- Nicholson, K. W. (1988). The dry deposition of small particles: a review of experimental measurements. *Atmospheric Environment*, 22(12), 2653-2666.
- Nicholson, K. W. (1993). Wind tunnel experiments on the resuspension of particulate material. *Atmospheric Environment. Part A. General Topics*, 27(2), 181-188.
- Ould-Dada, Z. (2002). Dry deposition profile of small particles within a model spruce canopy. *Science of the total environment*, 286(1), 83-96.
- Owen, P. R., & Thomson, W. R. (1963). Heat transfer across rough surfaces. *Journal of Fluid Mechanics*, 15(03), 321-334.
- Pérez, C., Nickovic, S., Pejanovic, G., Baldasano, J. M., & Özsoy, E. (2006). Interactive dust - radiation modeling: A step to improve weather forecasts. *Journal of Geophysical Research: Atmospheres*, 111(D16).
- Petroff, A., Mailliat, A., Amielh, M., & Anselmet, F. (2008a). Aerosol dry deposition on vegetative canopies. Part I: Review of present knowledge. *Atmospheric Environment*, 42(16), 3625-3653.
- Petroff, A., Mailliat, A., Amielh, M., & Anselmet, F. (2008b). Aerosol dry deposition on vegetative canopies. Part II: A new modelling approach and applications. *Atmospheric Environment*, 42(16), 3654-3683.
- Pope III, C. A., & Dockery, D. W. (1999). Epidemiology of particle effects. *Air Pollution and Health*, 31, 673-705.
- Pryor, S. C. (2006). Size-resolved particle deposition velocities of sub-100nm diameter particles over a forest. *Atmospheric Environment*, 40(32), 6192-6200.
- Pryor, S. C., Larsen, S. E., et al. (2007). Particle fluxes over forests: Analyses of flux methods and functional dependencies. *Journal of Geophysical Research: Atmospheres* (1984–2012), 112(D7).
- Pryor, S. C., Larsen, S. E., Sørensen, L. L., & Barthelmie, R. J. (2008). Particle fluxes above forests: observations, methodological considerations and method comparisons. *Environmental Pollution*, 152(3), 667-678.
- Rajot J L, Formenti P, Alfaro S, et al. (2008). AMMA dust experiment: An overview of measurements performed during the dry season special observation period (SOP0) at the Banizoumbou (Niger) supersite. *Journal of Geophysical Research: Atmospheres* (1984–2012), 113(D23).

- Raupach, M. (1992). Drag and drag partition on rough surfaces. *Boundary-Layer Meteorology*, 60(4), 375-395.
- Raupach, M. R., Briggs, P. R., Ford, P. W., Ahmad N., & Edge, V. E. (2001). Endosulfan transport: II. Modeling airborne dispersal and deposition by spray and vapor. *Journal of Environmental Quality*, 30(3), 729-40.
- Reheis M. C., Goodmacher J. C., Harden J. W., et al. (1995). Quaternary soils and dust deposition in southern Nevada and California. *Geological Society of America Bulletin*, 107(9), 1003-1022.
- Ruijrok, W., Davidson, C. I., & W Nicholson, K. E. N. (1995). Dry deposition of particles. *Tellus B*, 47(5), 587-601.
- Sehmel, G. A. (1971). Particle diffusivities and deposition velocities over a horizontal smooth surface. *Journal of Colloid and Interface Science*, 37(4), 891-906.
- Sehmel, G. A. (1973). Particle eddy diffusivities and deposition velocities for isothermal flow and smooth surfaces. *Journal of Aerosol Science*, 4(2), 125-138.
- Sehmel, G. A. & Sutter, S. L. (1974). Particle deposition rates on a water surface as a function of particle diameter and air velocity. *Journal de Recherches Atmospheriques*, 8, 911-920
- Sehmel, G. A. (1980). Particle and gas dry deposition: A review. *Atmospheric Environment*, 14(9), 983-1011.
- Seinfeld, J. H., & Pandis, S. N. (2012). Atmospheric chemistry and physics: from air pollution to climate change. Wiley-Interscience.
- Shao, Y., et al. (2003). Northeast Asian dust storms: Real-time numerical prediction and validation. *Journal of Geophysical Research*, 108(D22), 4691
- Shao, Y., & Yang, Y. (2005). A scheme for drag partition over rough surfaces. *Atmospheric Environment*, 39(38), 7351-7361.
- Shao, Y. (2008). Physics and modelling of wind erosion. Atmospheric and Oceanographic Sciences Library, 37, Springer.
- Sievering, H. (1981). Profile measurements of particle mass transfer at the air-water interface. *Atmospheric Environment (1967)*, 15(2), 123-129.
- Slinn, S. A., & Slinn, W. G. N. (1980). Predictions for particle deposition on natural waters. *Atmospheric Environment*, 14(9), 1013-1016.
- Slinn, W. G. N. (1982). Predictions for particle deposition to vegetative canopies. *Atmospheric Environment*, 16(7), 1785-1794.
- Sokolik, I. N., Winker, D. M., et al. (2001). Introduction to special section: Outstanding problems in quantifying the radiative impacts of mineral dust. *Journal of Geophysical Research: Atmospheres*, 106(D16), 18015-18027.
- Stull, R. B. (2009). An introduction to boundary layer meteorology. Atmospheric and Oceanographic Sciences Library, 13, Springer.
- Tanaka, T. Y., & Chiba, M. (2006). A numerical study of the contributions of dust source regions to the global dust budget. *Global and Planetary Change*, 52(1), 88-104.
- Venkatram, A., & Pleim, J. (1999). The electrical analogy does not apply to modeling dry deposition of particles. *Atmospheric Environment*, 33(18), 3075-3076.
- Wells, S. G., McFadden, L. D., & Dohrenwend, J. C. (1987). Influence of late Quaternary climatic changes on geomorphic and pedogenic processes on a desert piedmont, Eastern Mojave Desert, California. *Quaternary Research*, 27(2), 130-146.
- Wedding, J. B., & Montgomery, M. E. (1980). Deposition velocities for full-scale corn and soybean canopies: a wind tunnel simulation. *Environment International*, 3(1), 91-96.



- Wesely, M. L., Hicks, B. B., Dannevik, W. P., Frisella, S., & Husar, R. B. (1977). An eddy-correlation measurement of particulate deposition from the atmosphere. *Atmospheric Environment*, 11(6), 561-563.
- Wesely, M. L., Cook, D. R., Hart, R. L., & Speer, R. E. (1985). Measurements and parameterization of particulate sulfur dry deposition over grass. *Journal of Geophysical Research: Atmospheres*, 90(D1), 2131-2143.
- Wesely, M. L., & Hicks, B. B. (2000). A review of the current status of knowledge on dry deposition. *Atmospheric Environment*, 34(12), 2261-2282.
- Winchell, A. N., & Miller, E. R. (1918). The dust fall of March 9, 1918. *American Journal of Science*, (274), 599-609.
- Zhang, L., Gong, S., Padro, J., & Barrie, L. (2001). A size-segregated particle dry deposition scheme for an atmospheric aerosol module. *Atmospheric Environment*, 35(3), 549-560.



# Acknowledgement

I would like to express my heartfelt gratitude to my supervisor, Prof. Yaping Shao, for all the support, encouragement and inspiration throughout this study. His professional and technical guidance enabled me to understand the subject and is invaluable to me. I wish to acknowledge the support of Prof. Xiaojing Zheng and Prof. Ning Huang in Lanzhou University for the wind-tunnel experiments. I am deeply indebted to the three of them. Without their support the work would not have been possible.

I owe my deepest gratitude to the members of my thesis committee, Prof. Ulrich Lang, Prof. Susanne Crewell and Dr. Sabine Lennartz-Sassinek, for their encouragement, insightful comments, and challenging questions. I would like to express the deepest appreciation to my secondary supervisor Prof. Susanne Crewell for the professional and elaborate suggestion on the thesis improvement.

I would like to thank the rest of the research group of Prof. Shao, Dr. Shaofeng Liu, Martina Klose, Lars Kirchhübel, Chiyan Tsui (Paul), Zhuoqun Li, Michael Hintz, Max Haardt and Bozhana Dimitrova, for the fruitful discussions and suggestions that always give me new ideas to improve my research work. Especially, I thank Zhuoqun Li for the assistance of experiments and Chiyan Tsui (Paul) for the proofreading of the thesis.

I wish to thank my colleagues in Lanzhou University for the assistance of wind-tunnel experiments, especially Senior engineer Jinglan Che, Dr. Ning Cheng, PhD student Lei Guo, Wenhai Sun, Kejie Zhan, Xu Zhou, Guang Li and so on. The experiments would not be accomplished successfully without their disinterested assistance.

Thanks to the supporting staff in the Institut für Geophysik und Meteorologie, especially to Frau Dagmar Janzen who provides a lot of support to my work in the institute.

I would like to thank all my friends, Pingli Wang, Honghe Wang, XinXin Xie, Ye

Yuan and Tong Li who have contributed, in their own ways, to my work and life in Germany.

Finally, I would like to thank my beloved family, for their support, encouragement and understanding throughout these years.

# Erklärung

Ich versichere, dass ich die von mir vorgelegte Dissertation selbstständig angefertigt, die benutzten Quellen und Hilfsmittel vollständig angegeben und die Stellen in der Arbeit - einschließlich Tabellen, Karten und Abbildungen -, die anderen Werken im Wortlaut oder dem Sinn nach entnommen sind, in jedem Einzelfall als Entlehnung kenntlich gemacht habe; dass diese Dissertation noch keiner anderen Fakultät oder Universität zur Prüfung vorgelegen hat; dass sie - abgesehen von den unten angegebenen Teilpublikationen - noch nicht veröffentlicht worden ist, sowie dass ich eine solche Veröffentlichung vor Abschluss des Promotionsverfahrens nicht vornehmen werde. Die Bestimmungen dieser Promotionsordnung sind mir bekannt. Die von mir vorgelegte Dissertation ist von Prof. Dr. Yaping Shao betreut worden.

Köln, den 20. Aug, 2013

(Jie Zhang)



# Curriculum Vitae

## Personal Data:

**First name:** Jie  
**Family name:** Zhang  
**Date of birth:** 10.04.1983  
**Place of birth:** Suzhou, Anhui, P.R. China  
**Sex:** Male

## Education:

**1998-2001** The No.2 senior high school, Suzhou, Anhui, China  
**2001-2005** Bachelor, Department of Theoretical and Applied Mechanics, Lanzhou University, Lanzhou, Gansu, China  
**2005-2008** Master, school of Civil Engineering and Mechanics, Lanzhou University, Lanzhou, Gansu, China  
**2010-2013** PhD student, Institute for Geophysics and Meteorology, Cologne University, Cologne, Germany

## Working Experience:

**2009-2010** Engineer, Lanzhou University  
Responsible for the experimental teaching work for undergraduate students, and take charge of the experiment of the 'Multifunction Environmental' wind tunnel and its management work  
**2010-2013** PhD student, Cologne University  
Work for the DFG (Deutsche Forschungsgemeinschaft) project: 'A Wind-tunnel Study on Dust-deposition Mechanics and Validation of Dust-deposition Schemes'